Simulation of the ATLAS ITk Strip Endcap Modules for Testbeam Reconstruction and Analysis

by

Ryan Justin Atkin

A thesis submitted in fulfillment for the
degree of Master of Science

in the
UCT-ATLAS Group
Department of Physics
Faculty of Science

June 2019

Declaration of Authorship

I, Ryan Justin Atkin, declare that this thesis titled, *Simulation of the ATLAS ITk Strip Endcap Modules for Testbeam Reconstruction and Analysis* and the work presented in it are my own. I confirm that:

- This work was done wholly or mainly while in candidature for a research degree at this University.
- Where any part of this thesis has previously been submitted for a degree or any other qualification at this University or any other institution, this has been clearly stated.
- Where I have consulted the published work of others, this is always clearly attributed.
- Where I have quoted from the work of others, the source is always given. With the exception of such quotations, this thesis is entirely my own work.
- I have acknowledged all main sources of help.
- Where the thesis is based on work done by myself jointly with others, I have made clear exactly what was done by others and what I have contributed myself.

Signed: Signed by candidate

Date: 18 June 2019

UNIVERSITY OF CAPE TOWN

Abstract

Department of Physics
Faculty of Science

Master of Science

by Ryan Justin Atkin

The Large Hadron Collider (LHC) is planned to be upgraded to the High Luminosity LHC (HL-LHC), increasing the rate of collisions and producing more particles passing through the detectors. This increased production rate will require upgrades to the detectors in order to cope with the large increase in data collection and radiation as well as improving the tracking and particle reconstruction in the higher occupancy environment. A major upgrade to ATLAS, one of the LHC detectors, will be replacing the current Inner Detector (ID) with a fully silicon semi-conductor based Inner Tracker (ITk). The research and development phase of the ITk requires a simulation of the sensors for performance simulations and testing the sensors in test-beams. The ITk strip end-cap sensors will use radial geometries, however the current testbeam telescope simulation software (AllPix) and reconstruction software (EUTelescope) are designed with cartesian geometries. Presented is the work behind implementing a radial geometry for one of the ITk strip endcap sensors, the R0 module, in the simulation software of Allpix and the reconstruction software of EUTelescope. Included in this work is the simulation of the propagation of the charge deposited in the sensor by the beam. The simulated data, as well as data from the actual EUDET testbeam telescope at DESY, Hamburg are both reconstructed with the same reconstruction software and analysed using the same post-reconstruction software. A comparison of the simulation to experiment is then performed, in particular to study the residuals, efficiency and charge sharing of the R0 module.

Acknowledgements

Firstly I would like to thank the National Research Foundation (NRF) for their financial support towards my Masters, as well as my family for their financial as well as emotional support and encouragement. This project has received funding from the European Unions Horizon 2020 Research and Innovation programme under Grant Agreement no. 654168.

I would like to thank my co-supervisors Stephen W. Peterson for his assistance when it came to the Geant4 implementation, Kenneth G. Wraight for his important input and guidance on my thesis, especially concerning EUTelescope, and Andrew Blue for his overall guidance of my project. I would also like to thank Kenneth and Andrew for their assistance in organising funding for me to visit DESY and work with them in Glasgow, and their assistance in helping me fit in during my trips in Europe.

Lastly, but certainly not least, I would like to thank my supervisor Sahal Yacoob for his very important input, guidance and supervision. His assistance when I had any financial or other problems was also greatly appreciated. It was also due to Sahal that I studied at UCT and did my masters on this specific project and it was him who introduced me to the ATLAS collaboration.

Contents

List of Figures

List of Tables

Abbreviations

2HDM	2 Higgs Doublet Model
ABCStar	ATLAS Binary Chip for final production
ALICE	A Large Ion Collider Experiment
API	Application Programming Interface
ASIC	Application-Specific Integrated Circuit
ATLAS	A Toroidal LHC ApparatuS
BNL	Brookhaven National Laboratory
BSM	Beyond the Standard Model
CERN	Conseil Européen pour la Recherche Nucléaire (European Organisation for Nuclear Research)
CMS	Compact Muon Spectrometer
DAQ	Data AcQuisition system
DESY	Deutsches Elektronen-Synchrotron (German Electron Synchrotron)
DUT	Device Under Test
ECal	Electromagnetic Calorimeter
EUDAQ	DAQ for the EUDET telescopes
EUDET	Detector R&D towards the international linear collider
FCal	Forward Calorimeter
FE	Front End
FPGA	Field-Programmable Gate Array
GBL	General Broken Lines
GEANT4	GEometry ANd Tracking 4
GEAR	GEometry API for Reconstruction
HCal	Hadron Calorimeter

HCCStar	Hybrid Controller Chip for final production
HEP	High Energy Physics
HL-LHC	High Luminosity LHC
HLT	High Level Trigger
IBL	Insertable B-Layer
ID	Inner Detector
ILC	International Linear Collider
IP	Interaction Point
ITk	Inner Tracker
LAr	Liquid Argon
LCIO	Linear Collider I/O
LDO	Low-DropOut
LEP	Large Electron Positron
LHC	Large Hadron Collider
LHCb	LHC-beauty
LINAC	LINear ACcelerator
LoI	Letter of Intent
LS	Long Shutdown
MC	Monte Carlo
MIMOSA	Minimum Ionising MOS Active pixel sensor
MS	Muon Spectrometer
MSSM	Minimal Supersymmetric Standard Model
MWPC	Multi Wire Proportional Chamber
NIEL	Non-Ionising Energy Loss
PCB	Printed Circuit Board
PMT	Photo Multiplier Tube
PS	Proton Synchrotron
PSB	Proton Synchrotron Booster
QCD	Quantum ChromoDynamics
R&D	Research and Development
RF	Radio Frequency
SCT	SemiConductor Tracker
SLAC	Stanford Linear ACcelerator

SM	Standard Model
SPS	Super Proton Synchrotron
SS	Short Strip
SUSY	SUper SYmmetry
TDAQ	Trigger and Data AcQuisition
TLU	Trigger Logic Unit
TRT	Transition Radiation Tracker
UA1	Underground Area 1
UA2	Underground Area 2
vdM	van der Meer

Chapter 1

Introduction

It is believed that the first written account of the thought that matter is composed of small indivisible pieces, atoms, was by the Greek philosophers Democritus and Leucippus circa 450 B.C. [1]. However, the study and formulation of the atomic and sub-atomic realm only truly began in the very late 19th century with the discovery of X-rays in 1895 by Wilhelm Röntgen, radioactivity in 1896 by Henri Becqueral and the discovery of the first fundamental particle, the electron. The electron was originally known as a cathode ray, observed in the mid-19th century, and was finally isolated by J.J. Thomson in 1897 [2] when he also measured the electron's charge to mass ratio. These discoveries set about the search in understanding the atomic structure of matter, leading to the sub-atomic realm of particle physics. First came the discovery of the nucleus in 1911 by Ernest Rutherford [3], after which he discovered the proton in 1919. In 1932 came the discoveries of the neutron by James Chadwick [4] and the first anti-particle, the positron, by Carl D. Anderson [5].

Major discoveries after these were the discovery of the muon, the first non-generation one fundamental particle, in 1936 by S.H. Neddermeyer and C.D. Anderson using cosmic rays [6] and the electron anti-neutrino in 1956 by C. Cowan et al. at the Savannah River Site nuclear plant [7]. The constituents of the proton and neutron, the up and down quarks, as well as the strange quark were discovered in 1968 at the Stanford Linear Accelerator (SLAC) [8] [9]. Charm quarks were found through the discovery of the J/Ψ hadron in 1974 by both the SLAC [10] and the Brookhaven National Laboratory (BNL) [11] and the tau lepton in 1975 by the SLAC-LBL group [12]. In 1977 at Fermilab, the bottom quark was discovered [13] and the gluon was discovered in 1979 at the Deutches Elektronen SYnchrotron (DESY) [14]. The W and Z bosons were discovered in 1983 by Carlo Rubbia, Simon van der Meer and the CERN UA1 [15] [16] and UA2 [17] [18] collaborations. The heaviest of the fundamental particles, the top quark, was jointly discovered in 1995 by the CDF [19] and D0 [20] experiments at Fermilab. The most recent discovery was that of the Higgs boson in 2012 by the ATLAS [21] and CMS [22] collaborations at CERN.

The particle discoveries in the first half of the 20th century led to the development of the Standard Model (SM) of particle physics [23] [24] [25], currently the most comprehensive model of the fundamental particles and their interactions through the electro-weak and strong forces. Most of the particles discovered in the latter half of the 1900s were all predicted by the SM. Although the SM has been extremely successful to date with every test of it coming up with very little, if not non-existent evidence to dispute it, there are a few things it is incapable of explaining. Among that not predicted by the SM is dark matter, the elusive "stuff" that seems to cluster heavily in galaxies. Dark energy, the supposed "force" accelerating the expansion of the universe, the asymmetry of matter over anti-matter observed in the universe and the hierarchy problem of the large differences in masses between the 3 generations of particles are also among that list. This has led to several Beyond the Standard Model (BSM) theories, for example the two Higgs Doublet Model (2HDM) [26], String theory [27] [28], Supersymmetry (SUSY) [29] [30] and the Minimal Supersymmetric Standard Model (MSSM) [31].

Particles are difficult to detect, with the proton being on the order of 10^{-15} m in size [32]. This lead to the need for special detectors capable of observing these objects. The first device built for the purpose of observing particles was the spinthariscope [33], a device inspired by accident when William Crookes in 1903 dropped some radium and decided to search for it. It was a form of scintillator whereby a small screen was coated with zinc sulfide that would give off flashes of light when alpha particles collided with the zinc. The cloud chamber, an ionizing detector created by Charles T.R. Wilson in 1911 for which he won a Nobel prize, works through the use of charged particles travelling through a water saturated gas and leaving a trail of ions around which the water would condense. In 1928 came the first form of a drift tube, the Geiger-Müller tube, which used the ionizing ability of electrons to ionize a gas. The liberated electrons would then be attracted to the anode wire at the centre of the cathode tube, creating a measurable signal through the wire. The next development, still widely used today, was the Photo Multiplier Tube (PMT) in 1934 by Harley Iams and Bernard Salzberg. The PMT operated through the use of a plastic scintillator to create photons which were then used to create secondary electron emissions that formed an avalanche effect to boost the signal. An improvement to the cloud chamber came in 1952 with the Bubble chamber, invented by Donald Glaser, which used a superheated liquid instead of gas.

A major advancement, which earned Georges Charpak a Nobel prize for its creation, was the Multi Wire Proportional Chamber (MWPC) in 1968. The MWPC was effectively an advanced Geiger-Muller device with multiple wires and a smaller ion clearing time. The latest big invention came with the solid state semiconductor detectors first used in 1983. Semiconductors are used nowadays mainly for tracking purposes close to the interaction points due to their high granularity. The charged particles create around 80 electron-hole pairs per micron when passing through the depletion zone of the semiconductor [34], the volume around the area where the n-type and p-type semiconductor material meet and that is void of free charged particles. Today, detectors like the ATLAS detector at the LHC are larger than ever and use a combination of solid state, gaseous and scintillating detectors.

With all the predicted particles of the SM having been discovered, and considering that it is known that the SM is not a complete theory, what's left is for improved precision measurements of the SM and to search for new BSM physics. As there has been no evidence to support any BSM physics as of yet, the searches need to be improved. This will occur through the use of higher particle energies in the collisions as well as far higher luminosities to improve the statistics. These improvements will be the goal of the LHC by 2026, where particles will be colliding at a centre-of-mass energy of $\sqrt{s} = 14$ TeV and luminosities of around $\mathscr{L} = 7.5 \times 10^{34}$ fb^{-1} [35]. The detectors will need to be able to cope in the new environment with far higher radiation doses and have a track finding efficiency capable of dealing with the high pile-up.

One of the main sections of the ATLAS detector is the Inner Detector (ID). Being the closest sub-detector to the beam pipe, it is important for measuring the tracks of charged particles in order to calculate the charge and momentum of those particles, as well as determining the position of the vertices. The ID's location also means it receives the highest doses of radiation in the detector. Unfortunately, the current ID will not be able to cope in the high luminosity environment and will therefore require a complete overhaul. It will be replaced with an all silicon semiconductor Inner Tracker (ITk) during the Phase-II upgrade of the ATLAS detector starting in 2024 [35].

This thesis describes part of the R&D towards the ATLAS ITk, in particular the characterisation, simulation and testing of the innermost module in the Strip Detector endcap (forward) region, the R0 module. The current testbeam simulation (AllPix) and reconstruction (EUTelescope) software packages are defined with cartesian based geometries. Due to the radial layout of the strip sensors in the endcap regions, the R0 sensor is defined using radial geometries. This is the first time radial sensors have been studied with these testbeam packages and so they require the addition of radial descriptions. Once the testbeam telescope has been simulated, tracks are extracted from both the experimental and the simulated data during the reconstruction. An analysis is then performed with those reconstructed tracks to calculate the efficiencies, charge sharing and resolution of the R0 sensor.

Chapter 2

CERN, the LHC and the ATLAS Detector

2.1 CERN

CERN is a European research organisation located on the Franco-Swiss border in Geneva, Switzerland and founded in 1954 by 12 original member states [36]. An illustration of CERN is shown in Fig. 2.1. CERN is the largest particle physics research facility in the world, and has over 2500 official staff members and over 13000 fellows, associates, students, users and apprentices [37]. There are now 22 member states, 8 associate members and 6 observer states and organisations. CERN has many accelerators and detectors at its facilities, most of which are shown in Fig. 2.2, with the first accelerator being the Synchrocyclotron which was started up in 1957 and shut down as late as 1991. The name CERN originally came from Conseil Européen pour la Recherche Nucléaire, the name of the council setup in 1952 for the building of the laboratory. The name was changed to Organisation Européen pour la Recherche Nucléaire in 1954, although the acronym of CERN was kept.

Some of the notable achievements in physics at CERN include the discovery of the W and Z bosons in 1983, the first production of anti-atoms, anti-hydrogen [39], in 1995, and the discovery of the Higgs boson in 2012. Due to the large amounts of data that the experiments at CERN deal with, as well as the need for remote access to all of that data, CERN has also become a world leader in computer science. It was at CERN that the World Wide Web [40] was designed and where on 20 December 1990 the worlds first website and server went online.

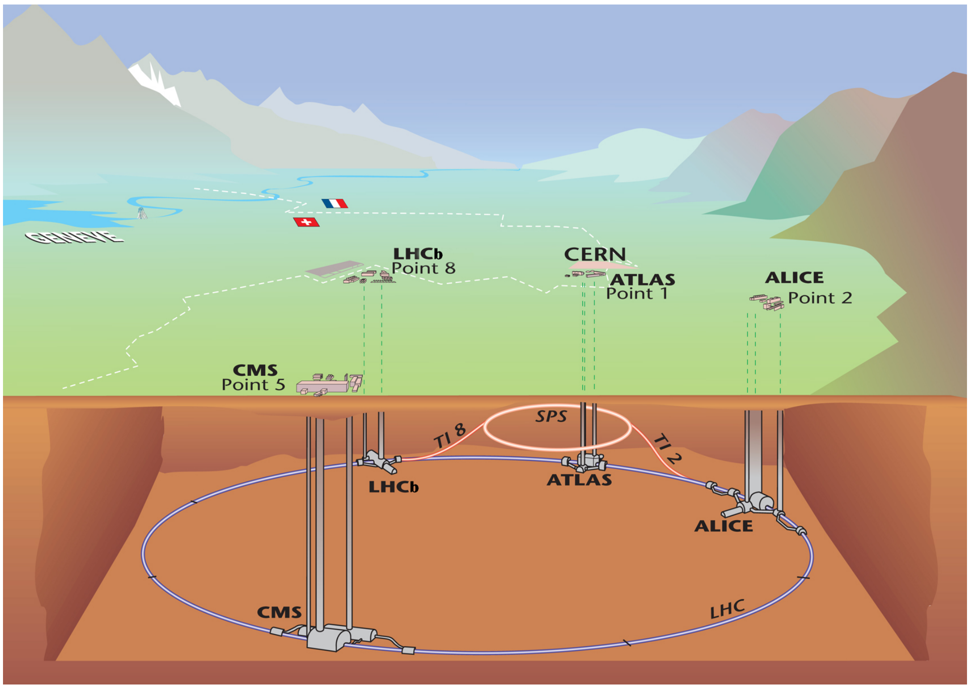

FIGURE 2.1: An illustration of the LHC and the underground caverns of the four main experiments [38].

2.2 LHC

The Large Hadron Collider (LHC) is the latest collider to join the CERN accelerator complex, approved in 1994 with building commencing in 1998 and completed in 2008 [41]. It is also the largest machine in the world as well as the highest energy particle collider in the world, built to reach energies of $\sqrt{s} = 14$ TeV. It is situated beneath the border between France and Switzerland with a circumference of 26.7 km. The tunnel the LHC is located in was built between 1984 and 1989 for the Large Electron Positron (LEP) machine, which was closed in 2000 for the construction of the LHC, and lies between 45 m and 170 m below the surface [41]. The reasons for the machine to be placed underground were due to the costs of buying land for the machine, the environment issues that come with building a large accelerator above ground as well as for protection from cosmic radiation. The tunnel consists of eight octants, each running from the centre of one arc to the centre of the next arc, with straight sections in between. An illustration of these octants is shown in Fig. 2.3. The arcs contain the superconducting magnets used to bend and focus the beams [42]. The eight straight sections about 528 m in length are used for the detectors, beam injection, beam dumping and beam cleaning [42]. The superconducting magnets are chilled to 1.9° K and generate a roughly 8.33 T magnetic field [41]. The LHC pipe is a composite pipe with two inner beam pipes, one carrying the particles in a clockwise direction and the other in an anti-clockwise direction. These two pipes cross over at the interaction points within the four detectors. The construction of a composite pipe using

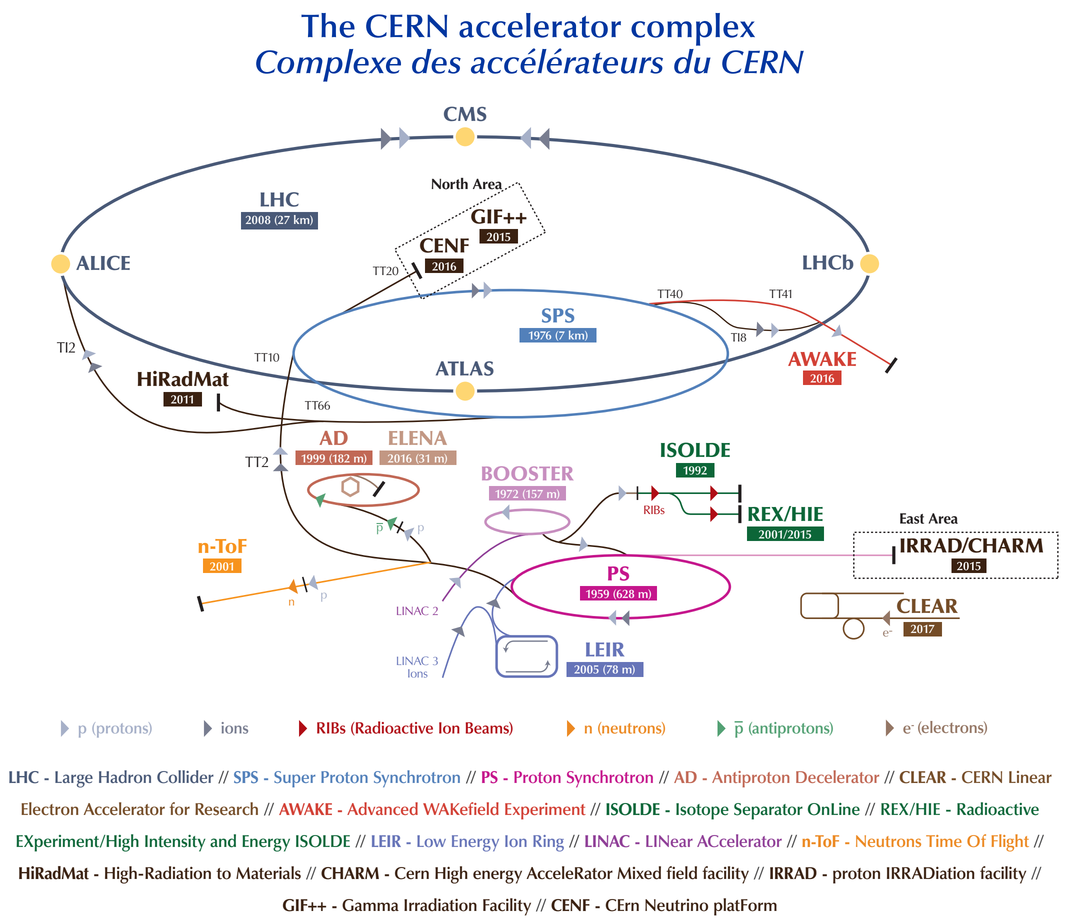

FIGURE 2.2: An illustration of the accelerator complex at CERN [43].

twin-bore magnets, instead of two separate beam pipes, was due in large part to the limiting size of the pre-existing tunnel and in small part due to it being a cost saving measure. The beam pipes are under ultrahigh vacuum, 10^{-13} atm, to allow for as few gas molecules as possible that the protons might collide with.

The various accelerators situated at CERN are shown in Fig. 2.2. The protons start off in the LINAC2, then travel through the Proton Synchrotron Booster (PSB), the Proton Synchrotron (PS), the Super Proton Synchrotron (SPS) and lastly get injected into the LHC. The LHC was designed to have 2808 bunches per beam with 1.2×10^{11} protons per bunch, and accelerate each proton up to 7 TeV (currently 6.5 TeV [42]). At this energy, the time between each bunch will be 25 ns (a bunch crossing rate of 40 MHz) and they will be travelling at a speed of 0.999999991 c [41]. The particles are collided in bunches as the probability of shooting two single protons at each other and having them scatter is highly unlikely. The reason for many small bunches as opposed to one large bunch is so that there will be a manageable amount of collisions per bunch crossing, and that it is easier to control and accelerate the smaller bunches. The lead ions follow a slightly different path into the LHC and are currently accelerated up to 2.56 TeV/u (energy

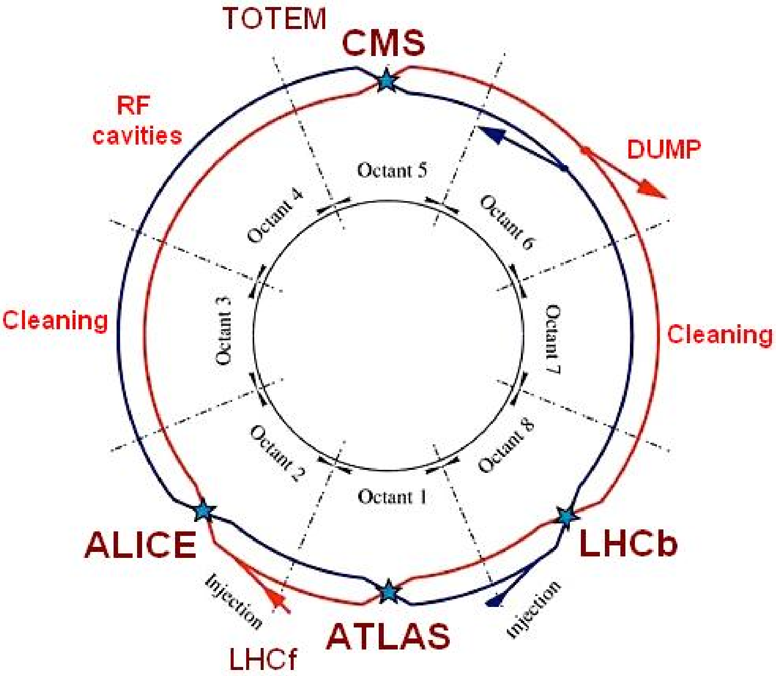

FIGURE 2.3: An illustration of the eight octants in the LHC [44].

per nucleon) [42]. The reason for the choice of a collider accelerator over that of a fixed target accelerator is that the energy available for particle production is the center-of-mass energy $\sqrt{s}$, where $s = (p_1 + p_2)^2$ and p is the four momentum of the particle. In the case of a fixed target accelerator, $\sqrt{s} \approx \sqrt{2mE}$, with E being the energy of the beam and m the mass of the particle. However, in the case of a collider, $\sqrt{s} = E_1 + E_2 = 2E$ assuming both beam energies are equal [45]. The choice of using hadrons in the LHC is that protons, being about 1836 heavier than the electron, will not suffer as much from the effects of synchrotron radiation, the radiation due to a particle travelling in a curved path. Protons are composite particles comprised of quarks and gluons. This results in far more complicated collisions than leptons, but it allows for the study of Quantum ChromoDynamics (QCD), which leptons do not. The purpose of the LHC is to test our current understanding of physics, as well as to study new physics models through the detection of new particles or observing discrepancies in well known constants. Areas of study will include the search for and precision measurements of the Higgs boson, detected the ATLAS and CMS experiments in 2012, the understanding of gravity at the quantum level, the search for possible dark matter candidates and investigating other BSM theories.

These studies will be performed primarily through the use of the four main experiments at the LHC. They are the ALICE (A Large Ion Collider Experiment) [46], ATLAS [47], CMS (Compact muon Spectrometer) [48] and LHCb (LHC beauty) [49] experiments. The locations of these experiments at the LHC can be seen in Fig. 2.3.

2.3 The ATLAS Detector

2.3.1 Overview

The ATLAS detector [47] is a multi-purpose detector located at point 1 of the LHC. Unless otherwise stated, all facts and figures in this chapter are from “The ATLAS Experiment at the CERN Large Hadron Collider” [47]. The name ATLAS originally stood for A Toroidal LHC ApparatuS, however it is no longer an acronym and is just plainly the name of the experiment. ATLAS is the largest experiment at CERN, being 44 m in length, 25 m in diameter and coming in at around 7000 tonnes. It is nominally forward-backward symmetric with respect to the centre of the detector and covers a full 2π angle around the beam and a nearly full 2π angle parallel to the beam. The main purpose of this almost full 4π coverage is to be able to more accurately calculate the missing energy in an event, which is used to determine whether there were any neutrinos, or new particles, produced in that event. The ATLAS detector consists of four main sections: the ID closest to the beam, the calorimeters, the Muon Spectrometer (MS) and the solenoid and toroid magnets. The design of ATLAS was based around a superconducting solenoid encompassing the ID and the large superconducting Toroidal magnets designed with an eight-fold azimuthal symmetry within the MS. A diagram of the ATLAS detector is shown in Fig. 2.4.

The Cartesian axes in ATLAS are defined so that the origin is at the point of interaction, with the positive $\hat{z}$ in the anti-clockwise direction of the LHC, $\hat{y}$ pointing up and $\hat{x}$ directed to the centre of the LHC ring. The positive $\hat{z}$ section of ATLAS is sometimes called the A side (anti-clockwise), while the negative $\hat{z}$ is the C side (clockwise). A cylindrical co-ordinate system is used, with $\hat{z}$ defined as already mentioned, the azimuthal angle $\hat{\phi}$ around the beam pipe ($x - y$ plane), and the angle θ defined as the angle between the beam pipe and the detection point ($z - y$ plane). A preferred co-ordinate used at ATLAS is the rapidity,

$$\mathcal{Y} = \frac{1}{2}\ln\left[\frac{E + p_z}{E - p_z}\right], \tag{2.1}$$

where E and p_z are the energy of the particle and the z-component of momentum respectively. For high-energy low-mass particles, i.e. essentially massless particles, rapidity becomes degenerate with pseudo-rapidity,

$$\eta = -\ln\left[\tan(\frac{\theta}{2})\right], \tag{2.2}$$

where θ is defined as before. Rapidity is used due to the momentum distribution of the hadron’s constituents being complex and possibly leading to boosts in collisions. Rapidity has a nice trait

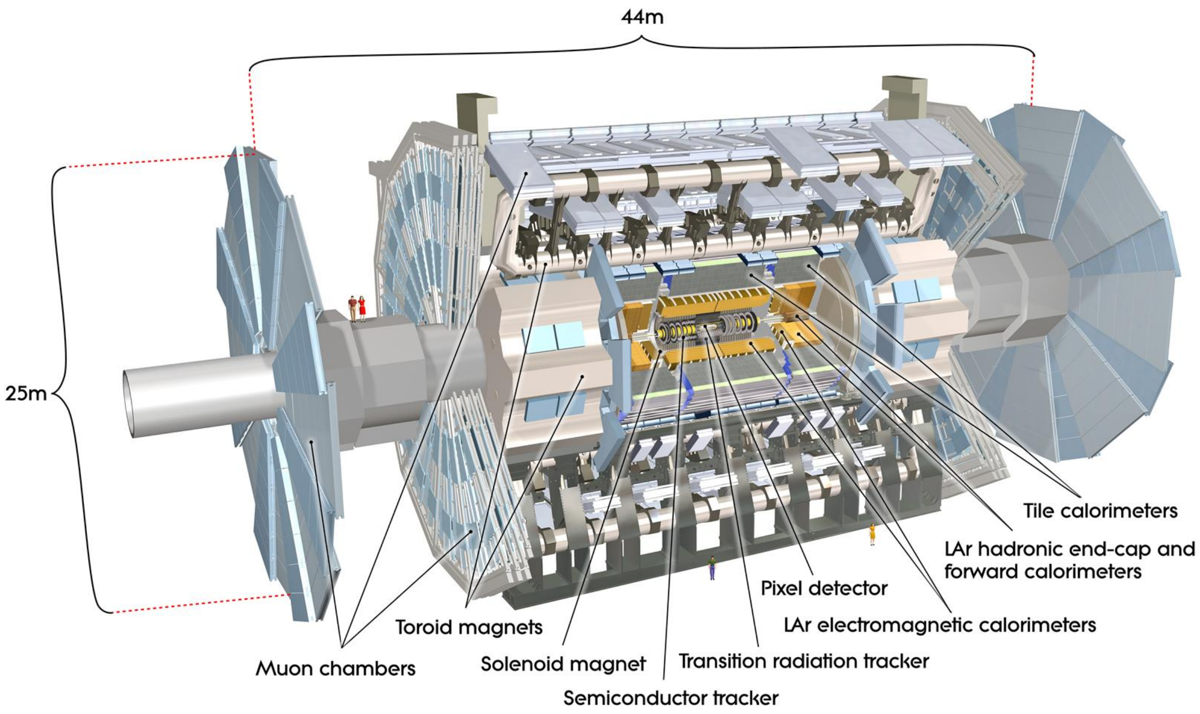

FIGURE 2.4: Cut away 3-dimensional view of the ATLAS Detector showing the several sub-detectors [47].

where the differences in rapidity are Lorentz invariant and are thus unaffected by these boosts, also resulting in roughly the same number of particles produced per unit rapidity. Another issue with the hadrons' complex momentum distribution is that longitudinal linear momentum conservation cannot be used, as the partons within the proton each carry a different fraction of the proton's momentum and these fractions are unknown at the time of the collision. However, due to there being negligible if not non-existent transverse momentum in the $x-y$ plane before a collision; transverse momentum p_T, transverse energy E_T, and missing transverse energy E_T^{miss}, are widely used variables. Transverse momentum is defined as $p_T = p\sin(\theta)$ and similarly for transverse energy. The distance between two points in pseudorapidity-azimuthal space is defined as $\Delta R = \sqrt{\eta^2 + \phi^2}$.

2.3.2 Magnets and Muon Spectrometer

The ATLAS detector's main feature is its unique hybrid superconducting magnet system consisting of a thin solenoid around the ID, and a barrel and two end-cap toroid magnets within the MS. The magnetic fields produced by these magnets are used to bend the charged particles so that their sign and momentum may be measured.

Muons are far heavier than electrons, thus they do not lose much energy through bremsstrahlung

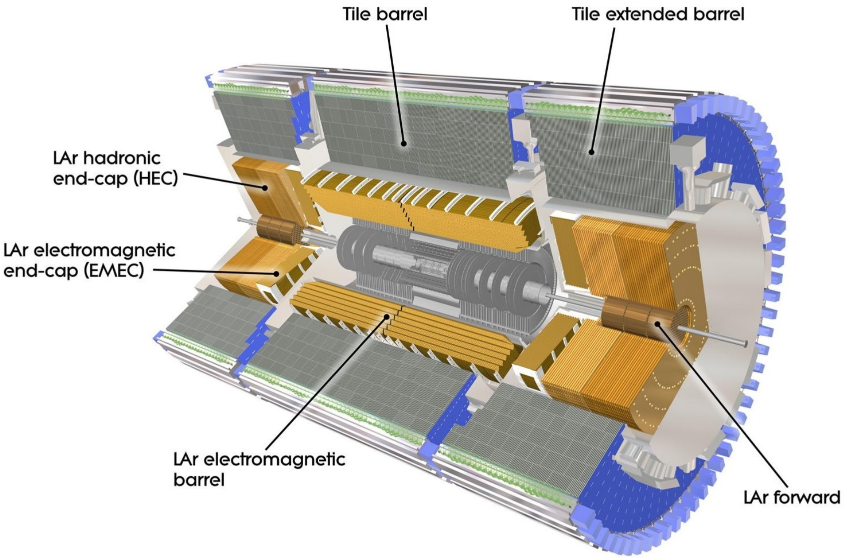

Figure 2.5: Cut away view of the ATLAS Calorimeter system showing the three subsections [47].

and as they are leptons, they do not interact via the strong force. This gives muons very high penetrating capabilities. It is for this reason that the MS is the final layer of the ATLAS detector where almost all the particles penetrating this far will be solely muons. The MS consists of separate triggers, $|\eta| < 2.4$, and high-precision tracking chambers, $|\eta| < 2.7$, within which sits the large toroid magnets.

2.3.3 Calorimeters

The calorimeters are the sub-detectors after the ID and before the MS and who's purpose is to measure the energy of the particles. The calorimeter system consists of three sections, namely the Electromagnetic Calorimeter (ECal), the Hadron Calorimeter (HCal) and the Forward Calorimeter (FCal), which are shown in Fig. 2.5. The calorimeters cover a pseudo-rapidity range of $|\eta| < 4.9$ and utilise varying techniques for different physics processes. The large eta range as well as the full 2π azimuthal coverage of the calorimeters is important in the measurement of the E_T^{miss} which is important for many physics signatures. The eta range of the ECal that matches that of the ID has high granularity for the precision measurements of photons and electrons. Outside that eta range is coarser granularity adequate enough for jet reconstruction and E_T^{miss} measurements.

Calorimeters measure the energies of particles via the particles giving off bremsstrahlung radiation creating a shower of particles and transferring their energy to the calorimeters. It is therefore important that the particles be contained within the calorimeters as much as possible. The containment of the particles will also prevent non-muon particles from entering the MS and creating fake muon signals. The calorimeters operate through the use of alternating layers of active sampling media and dense absorber materials which promote and sustain the showers. Liquid Argon (LAr) is the main active detector medium due to its linear behaviour and intrinsic radiation-hardness, but the HCal tile barrel uses scintillating tiles due to their higher density for strong interactions.

2.3.4 Inner Detector

The closest sub-detector to the beam pipe and immersed in a 2 T uniform magnetic field, the Inner Detector (ID) is important for particle identification, and momentum and vertex measurements of charged particles. It is 2.1 m in diameter and 6.2 m in length, also making it the smallest sub-detector. Measurements are possible for particles within the range $|\eta| \leq 2.5$ and usually above a threshold p_T of 0.5 GeV. The particle momenta and charge sign are measured using the bending of the tracks. The direction of the curve gives the charge sign while the greater the momentum of the particle, the less it bends in the magnetic field. The relative resolution in momentum increases as the momentum of the particle increases and is given by the following equation [50]:

$$\frac{\sigma_{p_T}}{p_T} = \frac{p_T \sigma_x}{0.3BL^2}\sqrt{\frac{720}{N+4}}. \tag{2.3}$$

Here, σ_{p_T} is the uncertainty in the transverse momentum measurement p_T and σ_x is the track measurement error, assumed to be constant for each point. The magnetic field B is measured in tesla, the chord length L of the arc from the first to the last point is in metres and the momentum is given in GeV/c. N is the number of equally distributed points over the arc. A requirement of the ID is to be able to accurately reconstruct vertices, showing which reconstructed objects are linked to the same process. B-hadrons have a longer lifetime than the lighter quarks and can travel $c\tau \sim$0.5 mm [51] before decaying, forming a secondary vertex displaced from the primary vertex. Reconstructing this secondary vertex is therefore important for finding b-jets.

There are three sections to the ID, going from the innermost outward and also descending in granularity, are the Pixel, Semi-Conductor Tracker (SCT) and the Transition Radiation Tracker (TRT). The decrease in granularity and efficiency is due in most part to costs, as well as the amount of readout cables, power cables and cooling pipes that would be required for a full pixel ID. The pixel and SCT operate in a temperature range of -5° C to -10° C to reduce leakage current and contain the annealing due to the radiation.

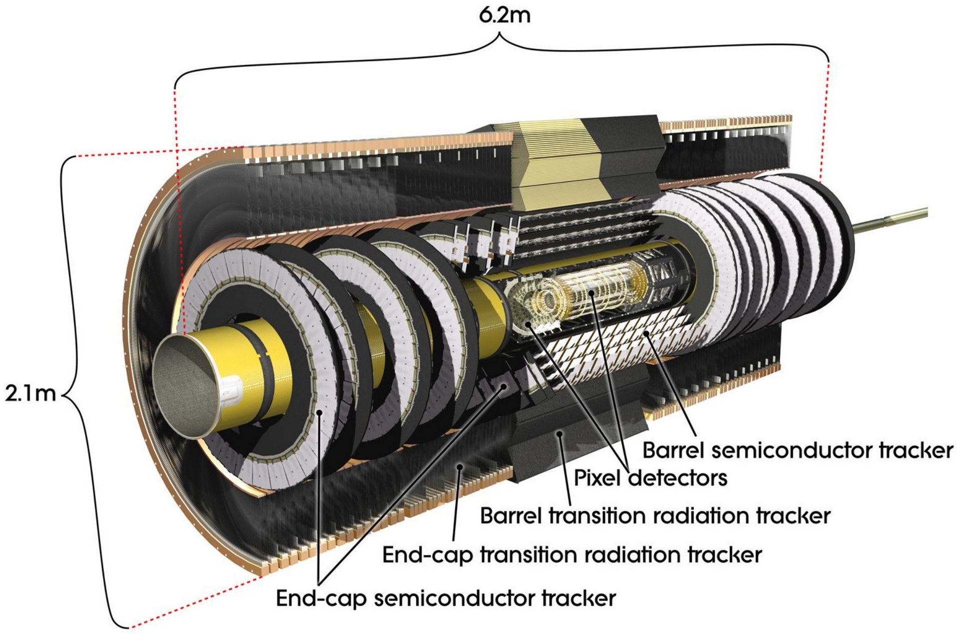

FIGURE 2.6: Cut away view of the ATLAS Inner Detector showing the three subsections [47].

2.3.4.1 Pixel Detector

The pixel detector is the closest section to the beam pipe (made evident in Fig. 2.7) and thus requires the highest granularity and resolution. The pixel sensors are 250μm thick and each pixel has an area of $50 \times 400 \mu m^2$. There are 47 232 pixels per sensor, and a total of 1744, 19×63 mm^2 sensors in the pixel detector, resulting in around 80.4 million readout channels. In the pixel barrel, the sensors are placed on staves arranged in three layers. In the endcap region, the sensors are placed on disks with three disks per side. The inner most layer (B-layer) was intended to be replaced every three years due to the high radiation dose it receives, while the other two layers were designed to withstand a 1 MeV neutron equivalent radiant energy per unit area (see Section 3.2.2.1) of up to $\sim 8 \times 10^{14}$ n$_{eq}$/cm^{-2}.
In 2014 during Long Shutdown 1 (LS1), the beam pipe's diameter within the ATLAS detector was reduced to allow for the insertion of the Insertable B-Layer (IBL) [52]. The inclusion of the IBL was in preparation for the increase in luminosity the LHC would be running at in Run-2. It was inserted 1 mm from the beam pipe, adding a fourth layer for improved tracking efficiencies and allowed the B-layer to remain in the ID instead of being replaced. IBL pixel sizes are smaller than the other pixels at 50×250 μm^2 with a sensor thickness of 200 μm [52]. A new cooling system based on CO$_2$ evaporative cooling was implemented for the IBL as well, instead of the C$_3$F$_8$ used in other parts of the ID.

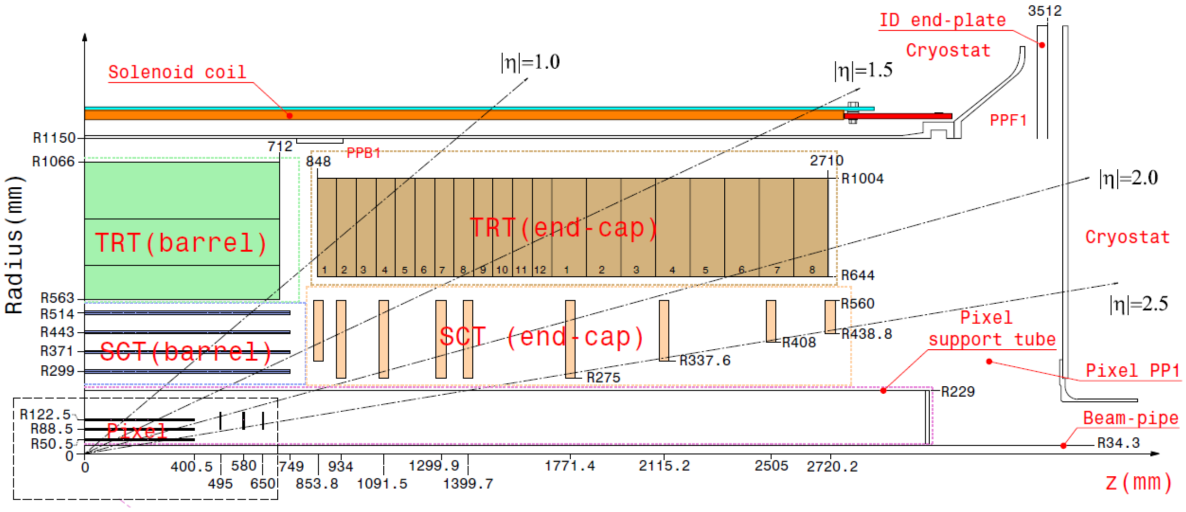

FIGURE 2.7: A quadrant of the ATLAS ID without the IBL [47].

2.3.4.2 SemiConductor Tracker

The SCT surrounds the pixel detector and uses p-in-n semiconductors, with 15 912 sensors that are $285 \pm 15\mu$m thick. Each sensor has 12 cm long active strips with a pitch of 80 μm, giving the SCT 6.3 million readout channels. The strips in the barrel are parallel to the beam while those in the end-cap are orthogonal to and focus on the beam pipe. The end-cap strips thus have an angular pitch ranging from 207 μrad to 161.5 μrad going radially out, giving an average of 80 μm. As the SCT is further from the interaction than the pixel detector, it was designed to withstand a 1 MeV neutron equivalent radiant energy per unit area of up to $\sim 2 \times 10^{14}$ $\mathrm{n_{eq}/cm^{-2}}$.

The strip sensors are arranged on staves in four layers in the barrel section, and on disks in the end-cap region with 9 disks either side. Since the strips are elongated, they are only capable of 1D position measurements. Therefore the staves and disks are double sided as to allow for the measurement of the space points through the use of stereo angles, the angle between the strips on adjacent sides of a stave. The second dimension of the position is measured using the points where the strips on either side of the stave overlap. In the barrel region, one side of the stave has the strips running parallel to the beam while the strips on the opposite side are rotated off this direction by a stereo angle of 40 mrad. The end-caps have a similar situation, though the direction is orthogonal to the beam.

2.3.4.3 Transition Radiation Tracker

The TRT is the final section of the ID, surrounding the SCT and consists of gas filled drift (straw) tubes instead of semiconductors. The tubes act as the cathodes while 31 μm thick tungsten wires coated in gold and split in half at about $z = 0$ in the barrel region act as the anodes. The

TRT provides track finding in the range $|\eta| = 2.0$ and only provides information in the $R - \phi$ planes. The barrel tubes are 1440 mm long and the end-cap tubes are 370 mm in length, with both being 4 mm in diameter. The barrel tubes are aligned parallel to the beam while the tubes in the end-cap are aligned radially, focusing on the beam pipe. There are 73 straw planes in the barrel and 160 straw planes in the end-cap providing a total of 351 000 readout channels in the TRT. The TRT provides a large number of hits per track (~ 36) which contribute significantly to the momentum measurements of the particles. The Xenon based gas mixture of the TRT provides improved electron identification through the detection of transition-radiation photons absorbed by the gas, which provide larger signals than the minimum ionising charged particles.

2.3.5 Trigger and Data Acquisition

The Trigger and Data AcQuisition (TDAQ) systems are comprised of smaller sub-systems, usually based on the sub-detectors. The Front-End (FE) systems of the detectors are used to convert the charge depositions in the sensors to an analogue or digital signal which is used to reconstruct the objects. The triggers are used to determine whether an event has any interesting objects that are worth studying. Due to the large amount of data collected by the ATLAS detector (on the order of 10 TB a second during Run 1), storing and studying all of it would be near impossible. The trigger system is split into two main parts to help reduce the amount of data. The hardware based L1 trigger searches for high p_T events and the software based High Level Trigger (HLT) partially reconstructs events that passed L1 to determine if it is worth further study. Events that pass the HLT are transferred to the CERN computer centre for permanent storage.

2.3.6 Luminosity and Pile-up

In accelerator physics, two of the most important values to be concerned about are the luminosity and the cross section. Luminosity can be seen as the number of particles passing through an area per second, while the cross section is the probability of interaction between two particles. These two values can be used to calculate the number of expected events of a specific process and the average number of pp interactions per bunch crossing. These relations are as follows [53]:

$$\mathscr{L} = \frac{n_b f_r n_1 n_2}{2\pi \Sigma_x \Sigma_y}, \tag{2.4}$$

$$N_{process} = \mathscr{L} \sigma_{process}, \tag{2.5}$$

$$\mu = \frac{\mathscr{L} \sigma_{pp}}{n_b f_r}. \tag{2.6}$$

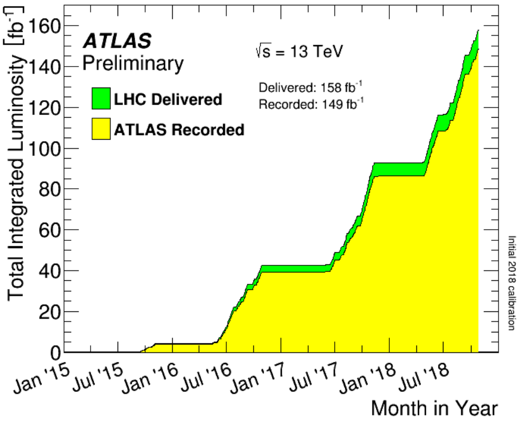

FIGURE 2.8: The cumulative luminosity delivered by the LHC (green) and recorded by ATLAS (yellow) during stable beams for pp collisions during the full Run 2 operation. The delivered luminosity is the total luminosity from when stable beams is declared to when ATLAS goes into safe standby mode for beam dump. The recorded luminosity is less due to the DAQ inefficiencies and due to the ATLAS warm-up before data can be taken. [55]

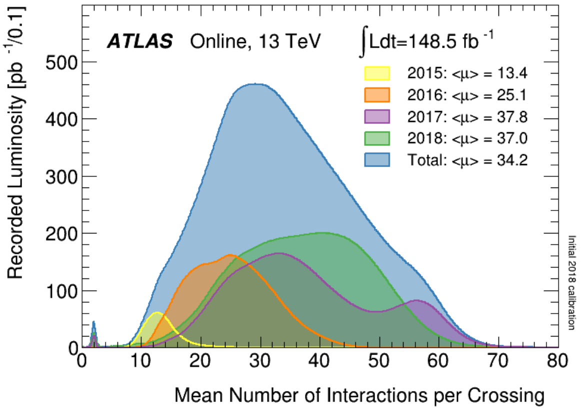

FIGURE 2.9: Shown is the luminosity-weighted distribution for the average number of pp interactions per bunch crossing for the full Run 2 pp collision data at $\sqrt{s} = 13$ TeV. The smaller peak at higher number of interactions in 2017 is due to luminosity levelling used at the end of 2017. [55]

where $\mathscr{L}$ is the instantaneous luminosity, N_{event} is how many events of a particular process are produced and μ is the average number collisions in a bunch crossing [53]. Here, n_b is the number of bunch crossings per revolution, f_r is the LHC revolution frequency, n_1 and n_2 are the number of protons per bunch and Σ_x and Σ_y characterise the horizontal and vertical convolved beam widths respectively. $\sigma_{process}$ is the cross section of the process under study and σ_{pp} is the inelastic pp cross section, assumed to be 80 mb for the $\sqrt{s} = 13$ TeV data. It is important to have accurate luminosity measurements in order to calculate the cross sections of the different processes. The measurement of the beam parameters in Eq. 2.4 are performed using van der Meer (vdM) scans [54]. In particle physics, luminosity is measured in Barns (b) and is defined as 1 b= 10^{-28} m^2 or in terms of inverse femtobarns, 1 fb^{-1} = 10^{39} cm^{-2}. The luminosity delivered to and measured by ATLAS in 2015 - 2018 is shown in Fig. 2.8. The total integrated luminosity is simply the time integral of Eq. 2.4. The other pp collisions (Pile-up) not involved in the high p_T event of interest, add large amounts of extra radiation in the detector. Pile-up can occur within the same bunch crossing (in-time pile-up), or be due to remnants left in the detectors from previous bunch crossings (out-of-time pile-up). The number of pp collisions per bunch crossing is determined by a Poisson distribution with a mean value given by Eq. 2.6. The number of interactions averaged over a time interval is defined as $\langle\mu\rangle$. Figure 2.9 shows the time averaged number of pp interactions for the 2015 - 2018 Run-2 data.

Chapter 3

LHC and ATLAS Upgrades

3.1 LHC

Since the start of the LHC, the Higgs boson has been discovered by the ATLAS [21] and CMS [22] experiments and many new limits have been applied to theories beyond the standard model. In light of this success and that the Higgs mechanism now needs to be studied in detail, there is a plan to upgrade the LHC to the High Luminosity LHC (HL-LHC). The upgrade will greatly increase the available statistics and allow for increased precision measurements of Standard Model processes as well as the possibility for improved BSM searches. The improvement will be possible through the increase in the instantaneous luminosity to a nominal (ultimate) value of $\mathscr{L}_{ins} = 5 \times 10^{34}\text{cm}^{-2}.\text{s}^{-1}$ ($\mathscr{L}_{ins} = 7.5 \times 10^{34}\text{cm}^{-2}.\text{s}^{-1}$) [35], five to seven and a half times the current nominal value. This will result in a nominal (ultimate) collision rate per bunch crossing of $\mu = 140$ ($\mu = 200$) [35] and over the 10 years of operation foreseen for the HL-LHC, a total integrated luminosity of over $\mathscr{L} = 3000$ fb^{-1} (3×10^{42} cm^{-2}). This luminosity increase will vastly improve statistics beyond that collected at any hadron collider before. Before the LHC, only 10 fb^{-1} of data had been collected by all the hadron colliders in the world. This was surpassed three-fold by the LHC after it collected around 30 fb^{-1} by the end of Run 1. At the end of Run 3, the LHC will have delivered approximately 300 fb^{-1} of data. During HL-LHC, it is expected that around 250 - 300 fb^{-1} of data will be delivered every year.

The current roadmap to the HL-LHC can be seen in Fig. 3.1. LS1 was used to reach the design values of the LHC for luminosity and increase the energy to $\sqrt{s} = 13$ TeV. LS2 will be used mostly for the upgrade of the injectors, with the replacement of Linac2 with the higher energy Linac4 [56]. The main upgrades, occurring during LS3, will focus on the accelerator magnets. Stronger magnets will be used to squeeze the beam at the interaction, as well as RF crab cavities that will reduce the crossing angle of the bunches so that they overlap better at the collision point.

Figure 3.1: The current plan for the upgrades to the LHC for the HL-LHC [57].

3.2 ATLAS

The LHC upgrades will result in the delivered luminosity and pileup occurring at levels beyond the current capabilities of the ATLAS detector. As such, the detector will require many upgrades in order to have sufficient radiation hardness, particle resolution detection and rapid enough readout channels to cope with the HL-LHC environment. These upgrades will occur over several stages, with a few having been completed already. The future upgrades will be split into the Phase-I upgrades during Long Shutdown 2, which will focus on upgrades to the trigger systems, and the Phase-II upgrades during Long Shutdown 3. This will allow the detector to be ready for HL-LHC during Run-4 of the LHC.

3.2.1 Phase-I Upgrade

The Phase-I upgrade will focus on upgrades to the trigger system. An important trigger for future physics will be triggering for low p_T isolated leptons (e and μ) and large acceptance in the forward region [58]. These will allow precision measurements of the Higgs properties in events where the Higgs is produced along with a W boson. WW boson scattering as well as SUSY searches will also require the low p_T lepton trigger. The trigger will also need to be able to quickly and efficiently select τ and b events for precision Higgs measurements.

3.2.2 Phase-II Upgrade

The Phase-II upgrades, scheduled to begin at the beginning of 2024, will be the largest upgrades to the ATLAS detector. The main focus will be the complete replacement of the current ID with a new, all silicon ITk. The other upgrades will mostly be improving the TDAQ systems throughout the ATLAS detector.

3.2.2.1 ITk

The source for the information in this section is "Technical Design Report for the ATLAS Inner Tracker Strip Detector" [35], unless otherwise stated. The large increase in particles passing through ATLAS during HL-LHC will increase the radiation damage as well as the occupancy level (amount of electronic signals) of the tracking components. Particles incident on a solid-state detector transfer energy to that material primaraily through two mechanisms; ionisation (losing energy to the valence electrons in the atoms) and non-ionising energy loss (NIEL) (transferring energy to the nuclei of the atoms) [59]. NIEL effects the crystalline structure of the silicon detectors by creating atomic displacements, forming interstitial atoms and vacancies in the lattice. This damages the detectors and can cause the bulk-type to change, as well as increasing the number of traps in the silicon, reducing the signal charge and increasing the leakage current [59]. This radiation damage is often given in terms of 1 MeV equivalent neutron fluence.

The ID's specifications were to operate at a peak luminosity of 10^{34} cm^{-2}s^{-1} for 10 years, with an average collision rate of $\mu = 23$ [60]. The current pixel system is able to withstand a total fluence (radiant energy per unit area) of 10^{15} n$_{\mathrm{eq}}$/cm^2 and the SCT a total of 2×10^{14} n$_{\mathrm{eq}}$/cm^2, where n$_{\mathrm{eq}}$ is 1 MeV neutron equivalent radiation [60]. However, the fluence is expected to exceed 2×10^{16} n$_{\mathrm{eq}}$/cm^2 in the innermost pixel region and 1.2×10^{15} n$_{\mathrm{eq}}$/cm^2 in the ITk strip section. The front-end electronics of the pixel and SCT detectors are capable of dealing with occupancy levels from $\mu = 50$ collisions per bunch crossing, and so will be unable to cope with the expected $\mu = 140$ to $\mu = 200$ collisions. The large amount of particles produced in these collisions will saturate the TRT, making it incapable of differentiating particles from each other. Hence, the ITk will consist solely of silicon detectors. The strip detectors will occupy the current space of the TRT and most of the SCT, and the pixel detectors will cover the current pixel region as well as part of the current SCT [61]. In the ID, the TRT acted as the polymoderator for the SCT barrel to reduce neutrons back scattered from the calorimeters, while the endcaps had their own dedicated polymoderator. Since the ITk will not have a TRT, it requires a dedicated neutron polymoderator for the strips barrel and a new polymoderator for the endcaps, both of which will be placed between the ITk envelope and the calorimeters.

Since the Phase-II Letter of Intent (LoI) [60], the ITk design has gone through a few modifications. The changes increased the tracking capabilities of the ITk up to $|\eta| \sim 4$ [62] and improved the resolution close to the interaction point while ensuring the correct redundancy required to deal with detector defects. A new CO$_2$ evaporation cooling method will be used in the ITk, after it was used for cooling in the IBL, cooling the sensors to a temperature of -25°C. The strip section will be split into the strip barrel and strip end-cap. The pixel section will be split

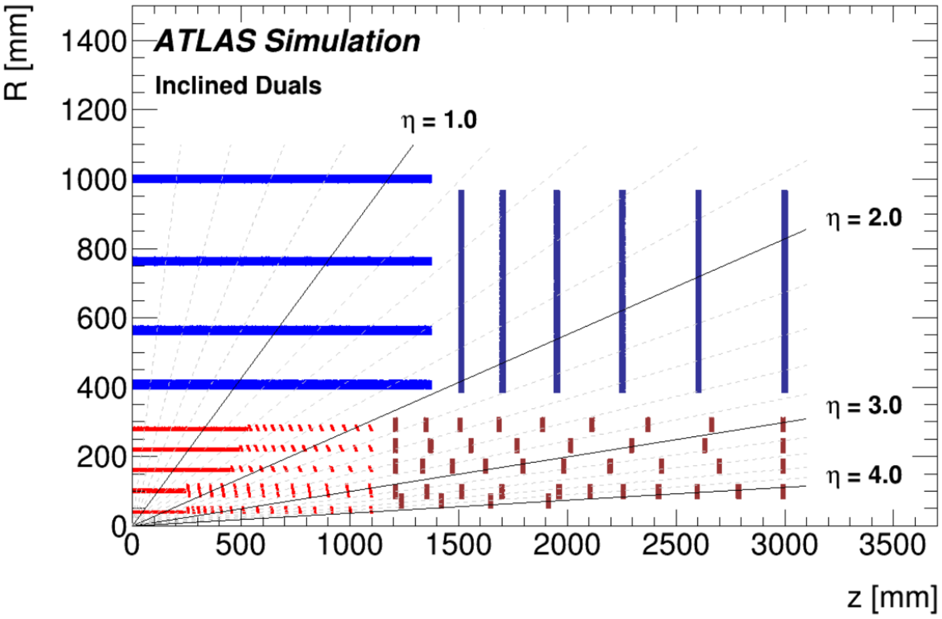

Figure 3.2: A quadrant of the inclined duals layout of the ATLAS Inner Tracker [61]. The blue lines represent the strip detector while the red lines represent the pixel detector. Comparing to Fig. 2.7, it can be seen how much larger the ITk pixel detector will be.

into the inner system (covering the first two layers), the outer barrel and the outer end-cap. A simple illustration of the ITk inclined duals layout can be seen in Fig. 3.2, which can be compared to that of the current ID in Fig. 2.7. The inclined duals layout is that which is presented in the ITk pixel Technical Design Report [61], and is so named as most of the inclined pixel modules are dual modules (modules that have two readout chips). This layout is not the final design, however it is the latest publicly available design and so will be used in this thesis. The pixel inner barrel and the central outer barrel modules will be horizontal to the beam. The forward outer barrel pixel modules will be inclined towards the Interaction Point (IP). All the end-cap modules will be vertical. The angle of inclination for the inclined pixel modules will be 75° in the first two layers and 56° in the outer 3 layers [61]. The inner two pixel barrel layers as well as the two inner most ring layers in the pixel end-cap will have their own inner support tube, which will allow for replacement in the future.

The local support structure for the strip detector will be the stave for the barrel, and the petal for the end-cap. Each stave will have 14 modules per side, giving 28 modules per stave. A module consists of a silicon sensor, 1 or 2 hybrids glued to the sensor and a power board. The hybrid is a kapton board with printed circuits on which sits the readout chips (ATLAS Binary Chips or ABCStar) and Hybrid Controller Chip (HCCStar). The chips are intended to be built with a thickness of 300 nm. An illustration showing an exploded view of a short strip barrel module can be seen in Fig. 3.3. The two inner strip barrel layers will have short strip modules, which have sensors with four rows of 24.1 mm long strips and two hybrids. The outer two layers will have long strip modules, which have sensors with two rows of 48.2 mm long strips and

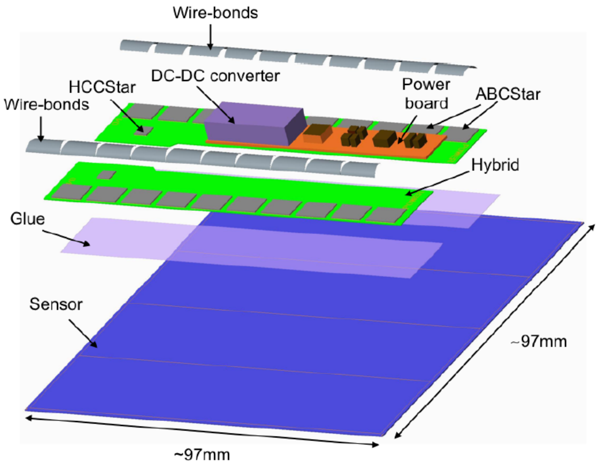

Figure 3.3: An exploded view of an ITk short strip barrel module [35]. The long strip barrel and end-cap modules follow the same basic design.

one hybrid. Both the short and long strip sensors will have a strip pitch, distance between the centres of the strips, of 75.5 μm.

The petals will have 9 modules per side, giving 18 modules per petal, utilising 6 different sensor designs organised in 6 rings. An illustration of a petal is shown in Fig. 3.4, with a cross section of a stave in Fig. 3.5. There will be 32 petals per disk placed in two layers of 16 with each petal slightly overlapping two petals in the other layer, ensuring no gaps between petals in a disk. The strips in the end-caps have varying lengths ranging from 19 mm closest to the beam to 60.1 mm furthest from the beam. This was chosen to keep the occupancy of the end-cap strips below 1%. The average strip pitch also ranges from 69.9 to 80.7 μm to allow a strip pitch of $\sim$75.5 μm at the bond pad regions where the readout strips are connected to the chips. Due to this, the modules in rings 0, 1 and 3 will have two hybrids reading out four rows of strips, while rings 2, 4 and 5 will have 1 hybrid reading out 2 rows of strips.

As the strips are elongated, they are only capable of 1 dimensional space point measurements. To measure the second co-ordinate, two modules are placed either side of a stave/petal with a stereo angle. The two layers of sensors are used to calculate one 2D space point per stave/petal layer. In the barrel, the sensors on both layers of the staves are placed at an angle of 26 mrad from the z-axis, giving a total stereo angle of 52 mrad. The end-cap has the stereo angle built into the sensor, with the strips placed at an angle of 20 mrad off the radial line. This gives a total stereo angle of 40 mrad between two corresponding sensors. The angle was built into the end-cap sensor to make placement of the sensors easier due to their wedge shape. The difference in the stereo angle between the barrel and end-cap is due to technical constraints.

One of the goals of a good tracking detector is to reduce the amount of material traversed by the particles so that they do not lose too much energy before they reach the calorimeters. A comparison of the nuclear interaction lengths traveled by a particle that has met the number of hits required for reconstruction between the ITk and the current ID is shown in Fig 3.6.

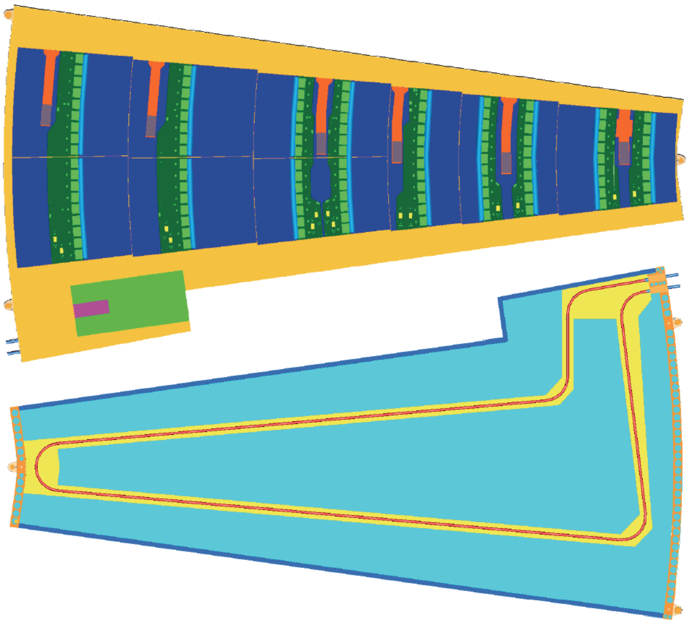

Figure 3.4: Illustration of the ITk end-cap local support structures, also known as petals [35]. The top image is the external view of one side of the petal, showing the modules and the End of Structure card (EoS) (green box). The bottom image is an internal view of the petal, showing the cooling pipes (red lines) and carbon foam (light blue).

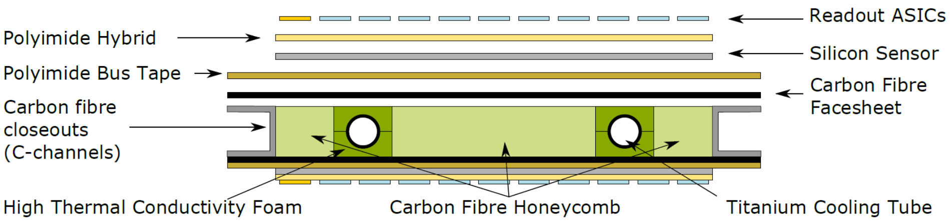

Figure 3.5: Illustration of the internal transverse view of a stave with the attached modules [35]. The end-cap petals will have a very similar design which can be seen if this figure is compared with 3.4. This diagram is not drawn to scale.

A nuclear interaction length is the mean distance a hadron (particle consisting of quarks) can travel until undergoing an inelastic nuclear reaction. The amount of material in the ITk is significantly reduced, improving the tracking efficiency as well. Two important aspects of a tracking detector are the tracking efficiency and the rate of reconstructing fake tracks, or the fake rate. The efficiency is defined as the ratio of the number of reconstructed tracks matched with a simulated particle, to the total number of simulated particles [61]. A comparison of the ITk tracking efficiency to that of the ID is shown in Fig. 3.7. The fake rate, in this case defined as the rate of tracks with no matching simulated particle [61], is shown in Fig. 3.8 for both the ITk and the current ID. Although the data from the ITk uses pileup of 200 events, it still out performs the ID which used only 20 pileup events. The ID data is shown with two different selection criteria, loose and tight. The loose selection requires less hits in the ID and reduced

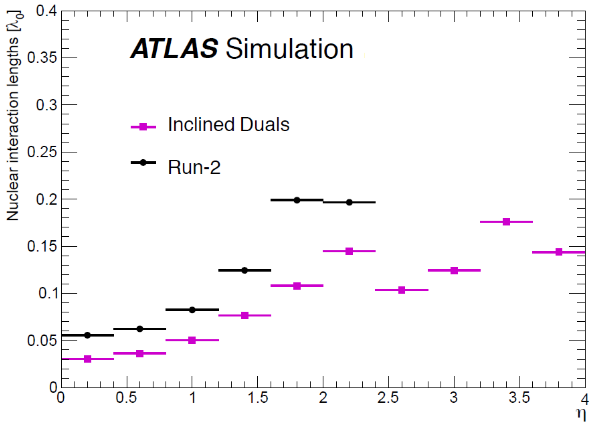

FIGURE 3.6: Number of nuclear interaction lengths traveled by a particle versus pseudorapidity, that has met the number of hits required for reconstruction [61]. Inclined duals is the name of the ITk layout as specified in the ATLAS ITk pixel TDR and Run-2 represents the ID setup during LHC Run-2.

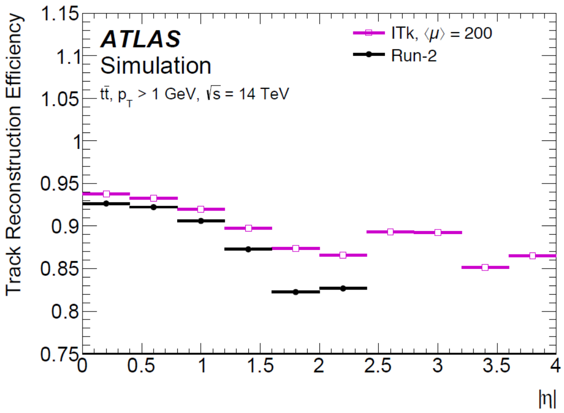

FIGURE 3.7: The efficiency for track reconstruction of a top, anti-top sample with an average pileup of 200 events. [61]

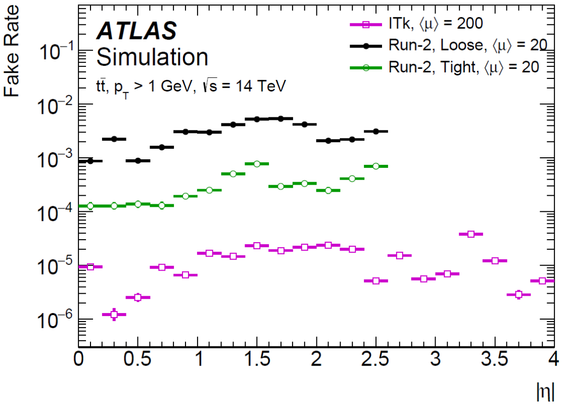

FIGURE 3.8: The fake rate for the reconstruction of tracks in top, anti-top events with an average pileup of 200 collisions [61]. The ITk results are compared to two different track selections in the ID, loose and tight.

information while the tight selection requires more hits in the ID, additional information and more cuts are applied.

Chapter 4

R0 Module and Software

This chapter will introduce the module that was simulated and the software in which it was simulated.

4.1 R0 Module

The R0 module is part of the ITk strip endcap system. It will be the innermost module and thus will receive the highest radiation dose in the strip endcap, around 1.5×10^{15} $\mathrm{n_{eq}/cm^2}$ expected during HL-LHC [63]. A picture of a R0 module prototype without the power board is shown in Fig. 4.1. The DC-DC power board in a full module is used to power the chips and monitoring sensors on the hyrids and to supply the bias voltage to the sensor. The current SCT sensors have p-type semiconductor strips in a n-type semiconductor bulk silicon wafer (p-in-n). The n-type bulk will invert to an apparent p-type bulk under fluences greater than 10^{13} $\mathrm{n_{eq}/cm^2}$ and will have to be operated at full depletion throughout its life [63]. Although using n^+-in-n could help against this, the expense of two sided processing required for n^+-in-n sensors is too great. So n^+-in-p silicon sensors will be used for the ITk strips detector, as the p-bulk will provide more signal than n-type after irradiation, making it more radiation resilient [35].

The strips of the R0 sensor will have a radial distribution not exactly azimuthally placed with respect to the beam due to the stereo angle of 20 mrad, as shown in Fig. 4.2. The start and end points of the strips will follow rings concentric with the beam pipe, while focusing on a point offset from the beam so as to create the stereo angle. The resultant shape of the sensor is known as a stereo annulus.

The strips will be placed in four rows, with the length of the strips increasing as one goes further out in the rows. The R0 module will have two hybrids (described in 3.2.2.1) reading out the strips, one hybrid for the inner two rows (rows 1 and 2) and one for the outer two rows (rows 3 and 4). The inner two rows have a different number of strips and angular strip pitch

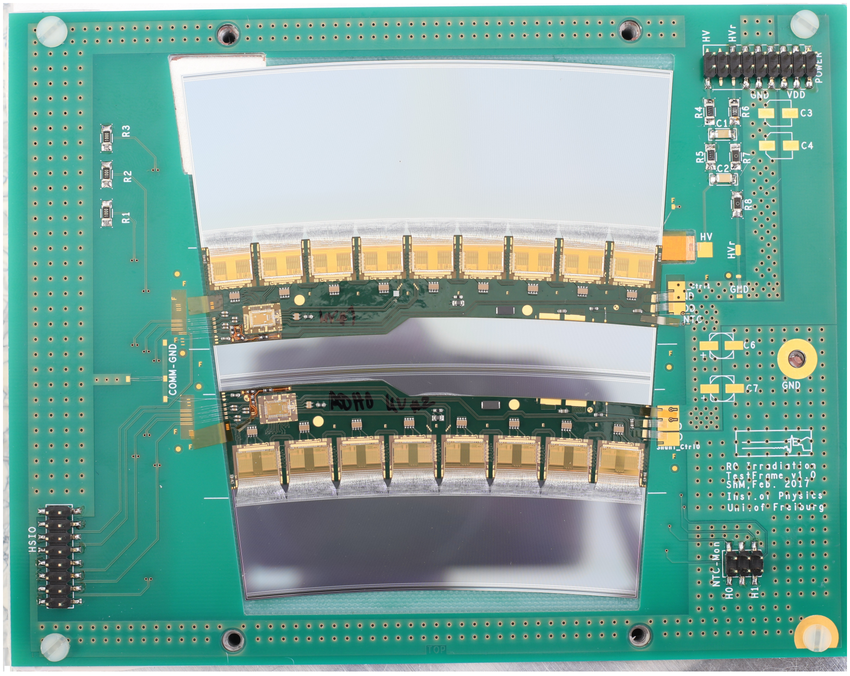

FIGURE 4.1: Picture of the R0 module tested at the testbeam at DESY in May 2017. Note that the power board has not been integrated into the module yet.

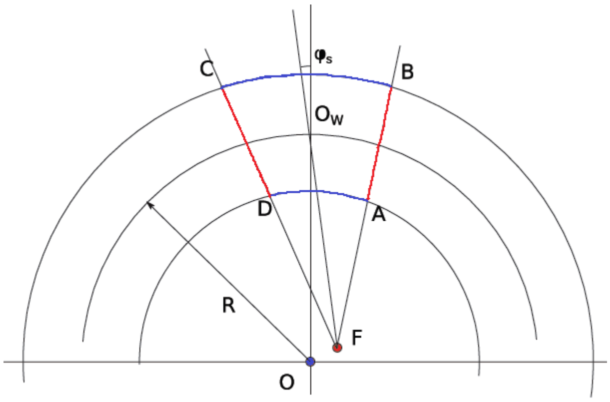

The sensor is drawn connecting ABCD.
The arcs CB and DA are centered at O
Strips have F as focus.
Sensor center O_W at radius R

FIGURE 4.2: Illustration of how the R0 module is defined [63]. The curved blue lines are concentric with the beam, while the straight red lines point to the offset point F instead of the beam. This offset results in the built-in stereo angle of 20 mrad. When placed in the detector, the sensor centre O_W will be 438.614 mm from the beam (O in the figure).

TABLE 4.1: The specifications of the R0 module [63]. Rows 0 and 1 were read out by one hybrid, while rows 2 and 3 were read out by another hybrid. The pitch is the distance from the centre of a strip to the centre of the next strip.

Row number	**nChips**	**nStrips**	**Inner Radius [mm]**	**Length [mm]**	**Angular Pitch [μrad]**	**Min/Max pitch [μm]**
0	8	1026	384.5	18.981	193.3	74.3/78
1	8	1026	403.481	23.981	193.3	78/82.6
2	9	1154	427.462	28.980	171.8	73.5/78.4
3	9	1154	456.442	31.981	171.8	78.4/83.9

compared to the outer two rows, where the angular pitch is the angular distance between two strips. The inner hybrid contains 8 readout chips and the outer hybrid has 9 readout chips. Each chip reads out 128 strips from each row, resulting in 256 strips per chip and 4352 readout channels for the R0 module. The chips are connected to the aluminium readout strips placed on the n-type semiconductor strips via wire bonds at the boundary regions of the strips. The boundary region between rows 2 and 3 will have no bond pads as these two rows are connected to separate hybrids. The first and last strips in each row are not used for readout, but instead are used for shaping the electric field for the outer readout strips. The sensor has a thickness of 310 ± 25 μm and a guard ring structure around the sensitive sensor 450 μm wide in the radial direction and 500 μm wide in the angular direction. The guard being thicker in the angular direction is due to the bond pads. More specifics of the R0 sensor are given in Table 4.1.
As the strips are not placed using a simple radial format, an algorithm to find the angle and position of each strip is used. These formulae are as follows [63]:

$$\phi'_i = (i - N_{strips}/2 + 0.5)\phi_p \tag{4.1}$$

$$b = -2\sin(\phi_s/2 + \phi'_i)2R\sin(\phi_s/2) \tag{4.2}$$

$$c = [2R\sin(\phi_s/2)]^2 - r^2 \tag{4.3}$$

$$r' = (-b + \sqrt{b^2 - 4c})/2 \tag{4.4}$$

$$x_i = r'\cos(\phi'_i + \phi_s) - R\cos(\phi_s) \tag{4.5}$$

$$y_i = r'\sin(\phi'_i + \phi_s) - R\cos(\phi_s) \tag{4.6}$$

Here, N_{strips} is the number of strips in a row, r is the position from the beam, ϕ_p is the angular strip pitch for that row, ϕ_s is the stereo angle, R is the distance of the centre of the sensor from the beam. The strips are labelled by i ranging from 0 to $(N-1)$. These formulae provide the position in (x, y) of strip i at a radius of r. These calculated positions are based on the sensor centre O_W sitting on the positive x-axis. The positions were rotated 90° anti-clockwise, ie. $(x, y) \longrightarrow (-y, x)$, to simulate the sensor with the centre on the positive y-axis. Derived from these formulae and after rotation, the focus point (F_x, F_y) and angle of the strips ϕ_i are calculated using:

$$(F_x, F_y) = (R\sin(\phi_s), R(1 - \cos(\phi_s))) \tag{4.7}$$

$$\phi_i = \phi_i' + \phi_s + \pi/2 \tag{4.8}$$

The readout chips use a 1-bit Analog-to-Digital Converter (ADC) and only stores information of whether there was a hit or not, no information relating to the shape of the analog signal is stored [64]. The collected charge from the sensor is integrated through a pre-amplifier and the following pulse shaper adjusts the timing and shape of the input pulse to meet the input requirements of the ADC. The threshold value is provided as a differential voltage from an internal programmable 8-bit Digital-to-Analog Converter (DAC) to the comparator [64]. The comparator compares the input pulse to threshold voltage and if the input pulse is larger the threshold, the strip is registered as a hit.

4.2 Software

4.2.1 Simulation Software

AllPix [65] is a Geant4 [66] based simulator dedicated to the study of solid state detectors. Geant4 is a C++ based program used to simulate particles interacting with matter and is used in the simulation of the ATLAS detector in order to compare simulated Monte Carlo pp collisions to experiment. AllPix was developed as a generic simulator for pixel detectors, although it has an important application in the simulation of EUDET-type testbeam telescopes (refer to Section 5.1) due to the pre-defined detectors and telescope setups. The simulation is run from a description file, providing a simple way for the user to interact with the larger AllPix framework. The detectors used, their positions and rotations, the particles used and the physics processes defining the particles' interactions are specified in this file. The description file calls a detector database file in which the specifics of the different detectors are defined. The commands in the description file are mostly Geant4 commands, with some AllPix specific commands. Since Geant4 does not come with a dedicated digitiser (which converts the deposited charge into a digital signal), AllPix performs its own digitisation using the deposited energy and co-ordinates of the particles from Geant4. AllPix has digitisers defined in the package which are specifically designed for the detectors used in the testbeam telescopes. When a particle passes through a strip or pixel and deposits energy, its position is calculated with respect to the centre of that strip or pixel. From this, digitisation is performed and the channel numbers that had deposited charge greater than the threshold, and their corresponding detector, are output to text files. The text files are then converted to Linear Collider I/O (LCIO [67]) data format, using a Python based converter that comes with the AllPix package. The tracks of the particles are then reconstructed using EUTelescope in the same manner that data from the actual telescope is reconstructed. More on this in Section 4.2.2.

4.2.2 Reconstruction Software

EUTelescope [68] is a generic pixel telescope data analysis framework. It was designed as part of the EUDET [69] project to analyse data from the EUDET pixel telescopes as part of the R&D towards the International Linear Collider (ILC). EUTelescope is used to analyse data from both the EUDET testbeam telescope and AllPix simulations. The EUTelescope package has a step before the analysis that is used to convert the raw experimental data into LCIO format, but not the simulated data.

The main files the user interacts with are the configuration file, steering files and the GEAR files. The configuration file contains the paths to the input files and the output files, as well as the variables used by the source code. The steering files define the processors and specific input files for each step in the EUTelescope framework, with the essential steps being illustrated in Fig. 4.3. The Geometry API for Reconstruction (GEAR) [70] files define how many planes were used in the telescope/simulation, the positions and rotations of those planes, as well as any other information regarding the setup eg. magnetic field. The detectors can also have the number of pixels, the pixel pitch and size of the sensor defined in the GEAR file and passed to the specific geometry description in EUTelescope. Here the detector geometries are "constructed" using ROOT's [71] geometry class TGeo, where they are used to map the channel numbers to the local and global positions of the corresponding pixel or strip.

After the completion of each step, the output from those steps are placed in two separate files. The one file is used as input to the next step while the other file can be studied for quick analysis. For the ATLAS ITk strips R&D group, "EUTelescope Guide for ATLAS ITk Strip: Reconstruction and Analysis" [72] was used as the guide to using EUTelescope, and will be used as reference for the following explanation of EUTelescope. The first step towards analysis after conversion is the clustering stage. In this stage, the channels that registered a signal in each detector plane are grouped together to form clusters based on a distance parameter. In the following step, the hitMaker step, the clusters are used to form hits in the detectors' (local) reference frames and the telescope (global) reference frame. With these hits, a pre-alignment is performed and a new GEAR file is created with positions from the pre-alignment.

The next step, using the new GEAR file, is the patternRecognition step. The upstream MIMOSA arm has the 3 MIMOSA planes before the DUT and the downstream MIMOSA arm has the other 3 MIMOSA planes after the DUT. Clusters on the first and last planes in each arm are compared to each other to find a match within a distance parameter, creating a doublet. If a match is found, a prediction is made on the middle plane and if a cluster is found within

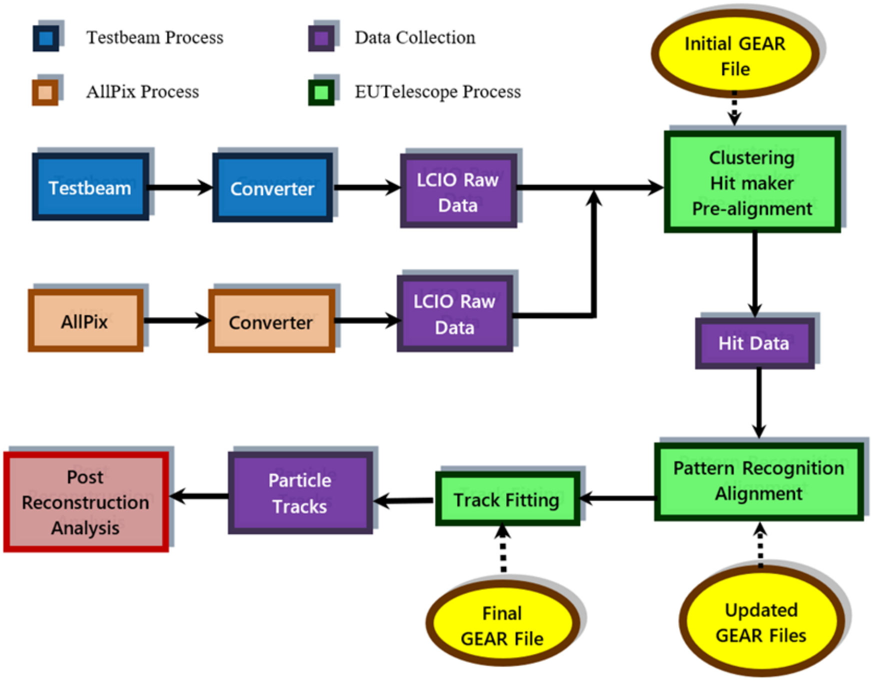

FIGURE 4.3: An overview of the EUTelescope framework. As can be seen, EUTelescope can take as input data from the EUDET testbeam telescope or the AllPix simulation software. The post reconstruction analysis is performed separately to the EUTelescope framework.

this prediction then a triplet is formed. If triplets are found on both arms, and their predictions of the track position at the centre of the telescope matches within a distance parameter, as well as their slopes matching within a different parameter, the triplets are combined into a “proto-track”. These proto-tracks are used by the following step, the GBLAlign step, to perform alignment of the planes. If a cluster on the DUT and FE-I4 fall within a certain distance from the proto-track, then those clusters are used to align the DUT and FE-I4 respectively. The alignment is done by performing a χ^2 minimization on the residuals of the clusters and proto-tracks. A new GEAR file is created with updated positions and rotations of the planes, to improve the transformation from local to global reference frames.

The patternRecognition and GBLAlign steps are usually repeated several times, with the patternRecognition distance parameters made smaller in the later iterations and the GEAR file being updated each time, to improve the alignment of the planes. Once enough iterations to get a good alignment of all eight sensors have been completed, typically around 4 or 5, a final patternRecognition is done with the latest updated GEAR file, after which the GBLTrackFit step is performed. The GBLTrackFit step performs the actual fitting of the tracks and outputs the information into a file which is then used in a separate analysis code to perform the final analysis. This post-reconstruction analysis takes the positions of the hits and the reconstructed tracks in the local reference frame of each detector to calculate the residuals, charge sharing and efficiencies.

4.2.2.1 Multiple Scattering

The GBL in GBLAlign and GBLTrackFit stands for General Broken Lines [73]. GBL is an advanced method for track fitting in High Energy Physics (HEP) and is a general case of the Broken Lines method [74]. When a charged particle passes through a medium, it can undergo multiple scattering (MS) due to the coulomb interactions with the atoms in that medium. Although there can be a lot of these scatters, each scatter results in a small angle deflection from the original path. The resultant deflection of the particle through a medium or plane i due to MS has an expected value of zero, with a variance given by [51]

$$\Delta\theta_i^2 = \left(\frac{z(13.6\text{ MeV})}{\beta c p}\right)^2 \epsilon_i(1 + 0.038\ln(\epsilon))^2, \tag{4.9}$$

where β, p and z are the velocity, momentum and charge of the incident particle respectively. The material budget $\epsilon_i = \frac{\Delta x_i}{X_{0,i}}$ is the thickness of material or plane i in terms of its radiation length, with the full telescope providing $\epsilon = \sum \epsilon_i$ [75]. The variance of MS is used in the χ^2 equation that is minimised when fitting the tracks [74], performed by the Millepede-II algorithm [76], in an extra term that accounts for the expected angular distribution due to MS in plane i. The material budget for the sensor planes includes the silicon with a radiation length of $X_0 = 93.65$ mm and a 25 μm thick protecting Kapton foil on each side of the sensor with $X_0 = 285.6$ mm [75]. The air between the planes is simulated as extra scatterers when calculating the full material budget and has $X_0 = 3.042 \times 10^5$ mm. There is approximately 150 mm of air between successive Mimosa planes, and about 100 mm of air before and after the R0. With the 6 Mimosa sensors each having a thickness of 50μm and the 2 DUTs with a thickness of 300μm each, the expected total material budget is 0.014. With an incident 4.4 GeV electron, the expected uncertainty on the deflection of a particle from its track due to MS from the entire telescope is 0.0003 rad (0.017 deg).

Chapter 5

Experimental Setup and Simulation

5.1 Experimental Setup

The EUDET testbeam pixel-telescope [69] [77] used during the testing of the R0 module is located at DESY in Hamburg, Germany. A closeup of the telescope can be seen in Fig. 5.1. The telescope is used to provide precision tracking for testbeam experiments wherein prototype sensors are tested. It comprises of six planes of high granularity Mimosa26 [78] pixel detectors used for track fitting, providing precisions of up to 2 μm [69]. Carbon fiber targets in the DESY II accelerator produce bremsstrahlung beams which are converted to electron/positron pairs using a metal plate. The electrons are used as the probes in the telescope with an energy range from 1 GeV to 6 GeV [69] and are selected through the use of a magnetic field, with a stronger field used to select the higher energy electrons. The Device Under Test (DUT) is usually placed between the third and fourth Mimosa planes, in the centre of the telescope.

The May 2017 testbeam performed tests for the first time on an ITk sensor with radial strips, the R0 module prototype, as well as tests on a full Short Strip (SS) module. This testbeam also used for the first time the updated generic data acquisition software EUDAQ2.0 [80]. Two types of measurements were performed; sensor performance studies, and radiation length (X_0) studies. In pre-lab tests, electrical characterisations were done for the R0 in order to study its performance in terms of noise, gain and response. For the purpose of this thesis however, these tests were not carried out on the simulated data and so will not be elaborated on. The main performance studies carried out are with the use of the beam. Track reconstruction is performed using the Mimosa26 planes with additional timing resolution of the Mimosa and DUT readouts provided by the FE-I4 [79] detector. Tracks are reconstructed by connecting the hits (a cluster of pixels/strips that collected charge above a threshold) across all 6 Mimosa planes within a certain (x, y) distance parameter. The (x, y) position of those tracks at the z location of the DUT is compared to the (x, y) position of the hits measured in the DUT. From this, information on

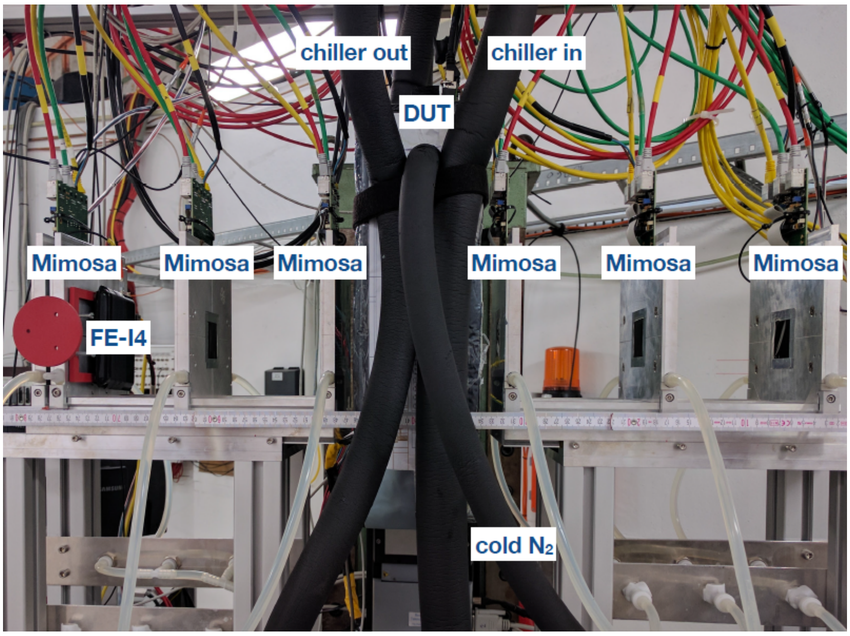

FIGURE 5.1: The R0 sensor placed as a Device under test (DUT) within the EUDET testbeam telescope [69] [77]. The DUT is placed within an insulated box in between the mimosa detectors [78] used to reconstruct the electron tracks. Also shown is the FEI4 detector [79] used for timing and the various cooling pipes. The electron beam comes in from the right and perpendicular to the planes.

the cluster sizes, charge sharing, efficiency and residuals of the DUT can be calculated. These tests were performed on both the R0 module prototype and the full SS module. An image of the SS module in its testing box is shown in Fig. 5.2, and the R0 is shown in Fig. 5.3. What made the SS module a so called “full” module, is that it contained a DC-DC power board attached to the sensor between the two hybrids, which is clearly absent on the R0 module. The red tubes in the boxes were meant for the vacuum to hold the module against the jig better, however due to a leak the vacuum was removing the nitrogen gas and so it was decided to not use the vacuum. A large amount of the wires in the box were used for the thermometers.

Several different beam positions on the DUT were planned to be tested that allowed for a variety of different situations. Not all of these positions were used however. In the R0 case, some chips had problems with the Low-Dropout (LDO) powering (hereby referred to as the disabled chips) in the pre-testbeam tests, reducing the numbers of testable chips. For the SS module, there was a problem with one of the hybrids, resulting in only one hybrid being used to readout. Despite this, enough data was collected for analysis, with about 92 million events for the R0 and 52 million for the SS module being recorded. A simple diagram showing the positions tested for the R0 is shown in Fig. 5.4. The disabled chips are visible, as well as the positions used in this thesis, given by the blue dots. The lack of positions in rows 2 and 3 is because that is the area that was covered by the cooling jig.

After the performance tests were complete, radiation length testing of the DUTs was performed. No power was supplied to and no data was taken from the DUT, as X_0 measurements examine

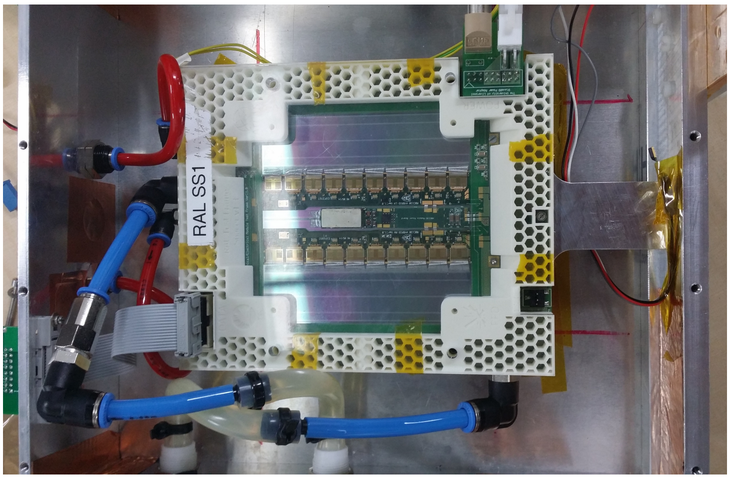

Figure 5.2: Image of the short strip module tested at DESY inside the insulating box. The blue pipes supplied the coolant to the jig to cool the module, the broad grey cable at the bottom left of the module is the readout cable and the two cables at the top right of the module, brown and white connectors, supplied the high and low voltage power. The remaining wires in the box were connected to thermometers.

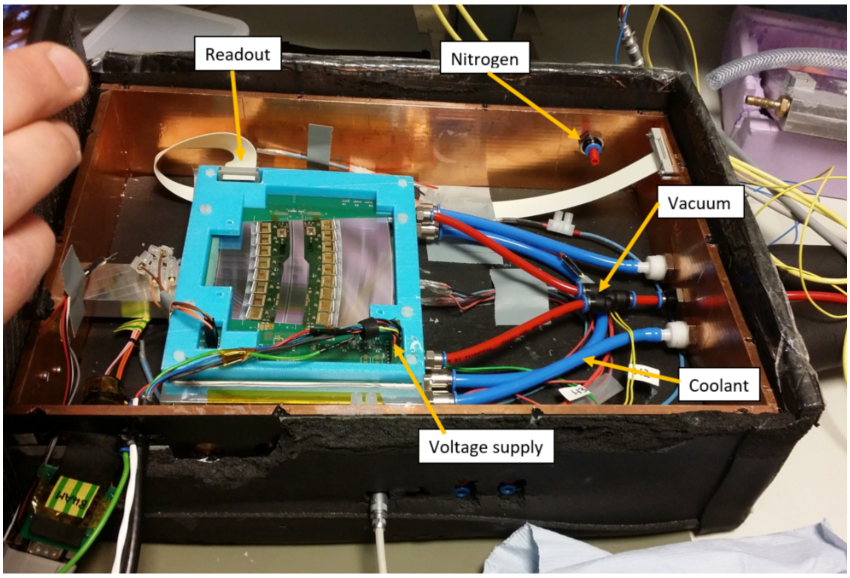

Figure 5.3: Image of the R0 module prototype tested at DESY inside the insulating box while being tested before being placed in the telescope.

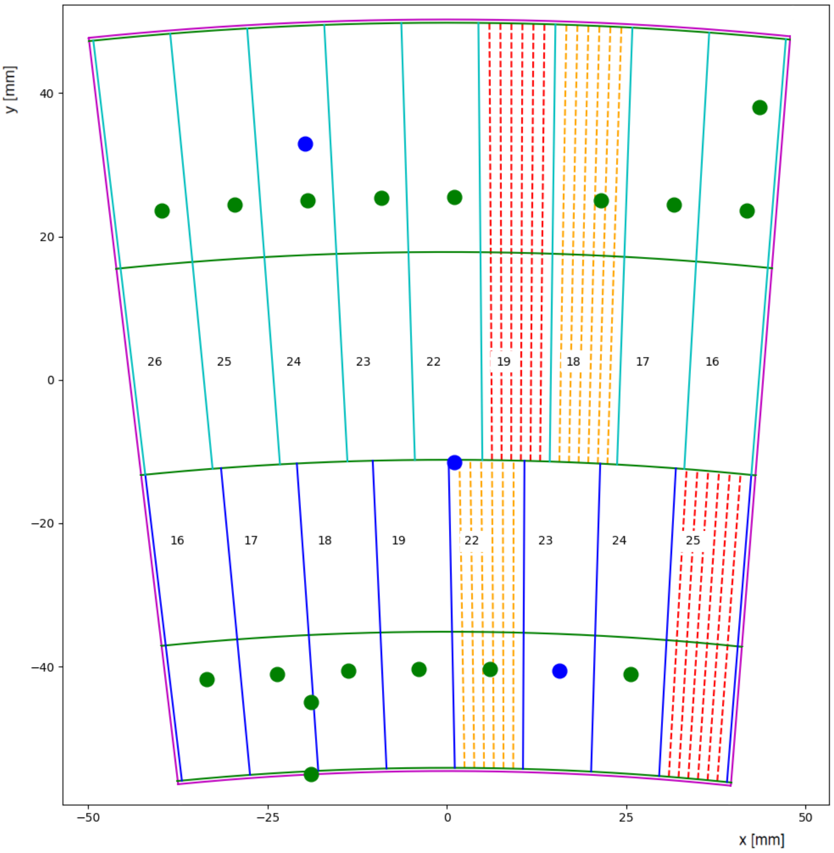

Figure 5.4: Simple diagram illustrating the different positions of the beam, represented by the dots, for the testing of the R0. The blue dots are the positions used in this thesis. The arced green lines are the boundaries between the rows of strips and the magenta lines are the edge of the sensor. The radially distributed cyan and blue lines represent the boundaries of the 128-strip wide area that is readout by one chip. The strip numbering increases in the direction of increasing chip ID as shown, where the lowest strip/channel number per chip is given by $Strip\_num = (Chip\_ID - 16) * 128$. The cyan lines represent the R0H1 hybrid with its chip labels in row 3, while the blue lines represent the R0H0 hybrid with its chip labels in row 2. The chips with orange dotted lines were the noisy chips and the red dotted lines are for the chips that had the LDO powering issues.

the material itself, not the electronics. As there was no data coming from the DUT, the FE-I4 was not required for timing and so was removed to reduce the amount of material in the telescope. The Mimosa26 planes were moved closer to the DUT box to improve the measurements of the small angle scattering. Over one million events were measured to provide high statistics for the X_0 measurements. A plot of the scattering angle based on position for the SS module is shown in Fig. 5.5(a), with the glue pattern specifications in Fig. 5.5(b). An ASIC (Application Specific Integrated Circuit), along with its five glue spots can be seen at $-4 < x < 4$ and $-4 < y < 4$.

For the performance tests, a beam energy of 4.4 GeV was used, while an energy of 3 GeV was used for the radiation length tests. The lower energy provided higher statistics as more electrons passed through the magnetic selector, while the higher energy reduced the amount of scattering

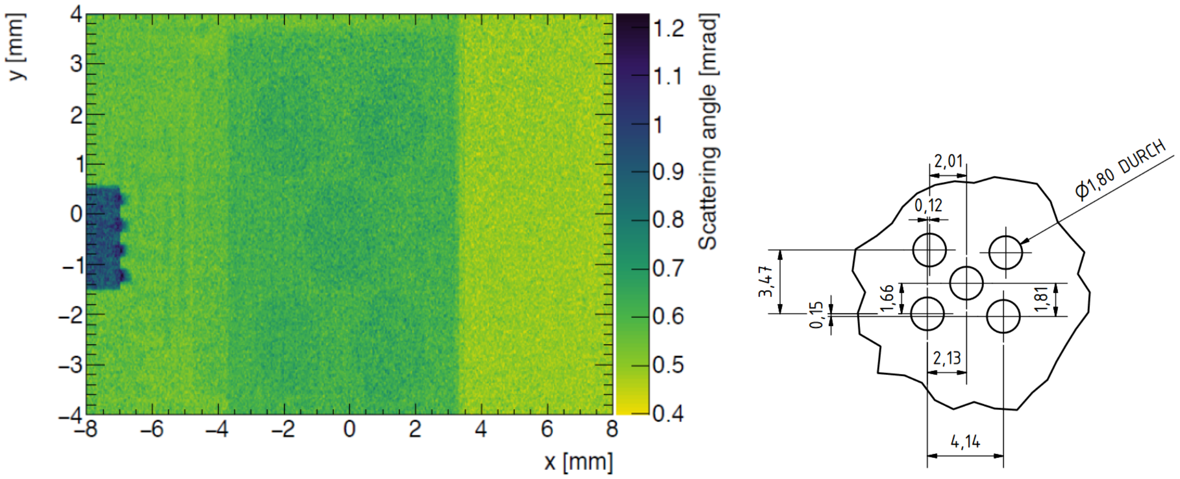

(a)

(b)

Figure 5.5: (a) Plot showing the scattering angle of the incoming electrons at different locations on the sensor [81]. The large blue-green rectangle between -4 and 4 in x and y is an ASIC, with the five circles in that rectangle being the glue holding the ASIC to the kapton of the hybrid. The dark blue rectangle on the left supplies the power to the chip. The yellow-green area at $x > 4$ is the sensor and the light green area at $x < -4$ is the hybrid. (b) The specs of the glue pattern used for the chips [82].

and improved tracking. A beam profile of 1.0×1.5 cm^2 was used in both radiation length and non-radiation length tests. For the performance tests, a voltage of 400 V was applied to both the R0 and SS modules for the majority of the testing. An operating voltage of 400 V is to ensure that the sensor operates at a level well above the depletion voltage of ∼300 V, making the sensor fully biased. Some tests were done at voltages of 100 V, 200 V and 300 V before and after the sensors were operated at 400 V to test for any effects of long term biasing. In order to cool the sensor during operation, a chiller pumped cooled glycol through the jig that held the module. The nitrogen gas used to reduce the humidity in the box was also chilled before entering the box for improved cooling. Operating temperatures for the R0 sensor were around -10°C and 10°C to 15°C for the SS module.

The triggers from the Mimosa planes, the FEI4 timing detector and the DUT were processed through the Trigger Logic Unit (TLU), with the DUT read-out first going through the ATLYS Field-Programmable Gate Array (FPGA) board. An interlock was used to cut the power to the DUT, excluding the HV, if the humidity or temperature in the DUT box was over a threshold. The full experimental setup is shown in Fig. 5.6.

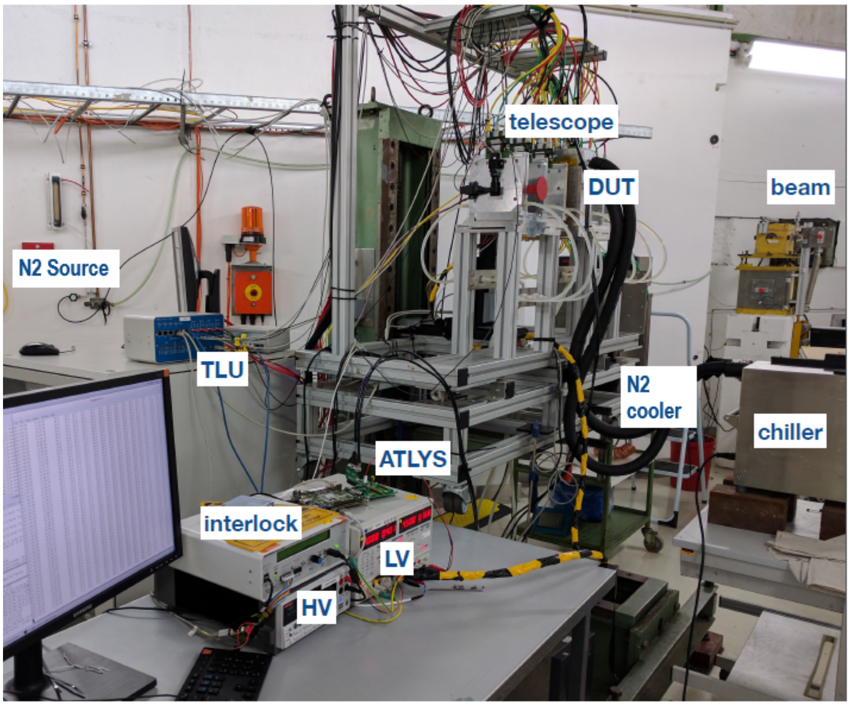

FIGURE 5.6: Image of the testbeam setup at DESY [81].

5.2 Simulation Software

The first step towards the simulation of the radial geometry of the R0 sensor was to add radial geometry specifics to the detector database and place the R0 sensor in the macro file. The R0 sensor was given an unique ID in the detector database file and is called by the macro using that ID. The main commands used in the macro are shown in Appendix A.1. Once the radial definitions were in the database, changes to the detector construction file were possible. A flag was added to the detector database file for the radial sensor to let the construction file know whether a radial geometry would be required instead of the usual rectangular geometries. The first simulations were simple radial geometries, with arbitrary dimensions and the focus point of the strips on the origin. The sensor shape was a simple tubular section with tubular shaped strips. The strips in a row were positioned by starting at one side of the sensor and simply increasing the phi co-ordinate while keeping the radial distance constant.

The true specifics and shape of the sensor only started to be implemented once access to the R0 technical specifications document [63] was provided. The specifics in particular are those referred to in Section 4.1. At the end of 2017, a strips group did precise measurements of the specifications of the R0 module tested at DESY in May 2017. They discovered that the lengths of the strips did not match those specified by the Technical Specifications in [63]. Instead, the strip lengths, as well as the beginning and ending points of those strips were as described in Table 5.1. The difficult part of simulating the R0 module was finding a way to create the "stereo annulus" shape. The technical specifications document for the R0 sensor provided an algorithm

TABLE 5.1: The revised R0 sensor specifications [83]. The lengths of the strips were found to be different to the specified values in the technical specifications document [63].

Row number	**Inner Radius [mm]**	**Outer Radius [mm]**	**Length [mm]**
0	384.5	403.518	19.017
1	403.518	427.515	23.999
2	427.516	456.451	28.994
3	456.451	488.422	31.912

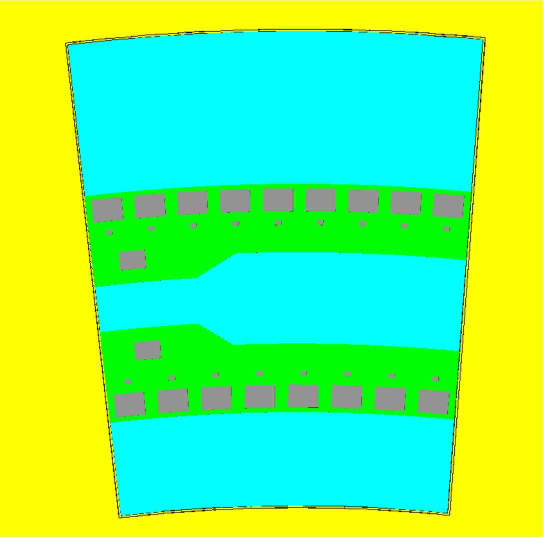

FIGURE 5.7: Image of the simulated R0 module. The yellow background is the PCB, the black outline is the inactive silicon guard ring, the sensor is defined by light blue, the hybrid is green and the chips and power supplies are the grey boxes.

for the placement of the strips, which provided insight into the design of the "stereo annulus". In the end, a simple intersection of a ring centred at the origin and a wedge centred at the offset point with sides at the same angles of the sensor edges, were used to create the final R0 sensor shape. The formulae were then used to place the strips, tubular shaped, at their correct positions and angles. These formulae are given in Section 4.1 and the important changes made to the construction file to accommodate for the R0 sensor are given in Appendix A.2. The final addition to the description of the R0 module was the two hybrids that sit on the surface of the sensor. The kapton base was modeled as a PCB while the chips and chip power sources were modeled as aluminium. With the full geometric description of the R0 complete, work began on the digitiser for the R0. An image of the simulated R0 is given in Fig. 5.7, while an image of the simulated telescope with the R0 can be seen in Fig. 5.8.

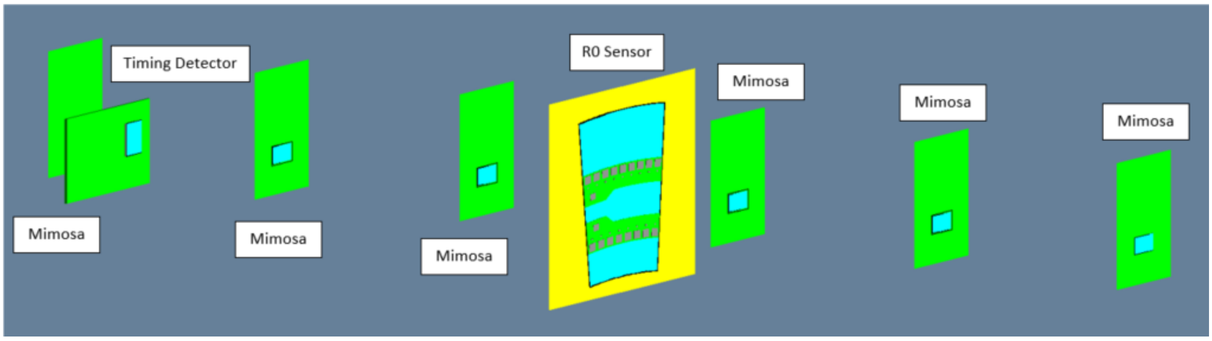

FIGURE 5.8: Image of the simulated EUDET telescope with the R0 module as the Device Under Test and a detector for timing (FEI4). The green rectangles are the PCBs (yellow in the case of the R0), the light blue areas are the sensitive areas of the detectors and the black lines around these sensitive areas are the inactive silicon guard rings. The R0 also has the hybrids in green with the grey rectangles as the chips.

5.2.1 Digitiser

A digitiser is used to simulate the behaviour of the front-end electronics on the detectors by converting the amount of deposited charge (analogue signal) to a digitial signal. Dino Tahirovic wrote a digitiser [84] for the barrel strip modules based on the Timepix [85] digitiser already in the AllPix framework. This digitiser was used as the basis for the R0 digitiser. Simulated information from Geant4, eg. position and energy of the charged particles, is used as input to the digitiser. The global position of the incident particle as it enters the sensitive volume of the sensor is first converted to a position in the reference frame of that sensor. From this it is possible to calculate the index of the strip the particle traversed, which is shown in the first part of Appendix A.3.

The role of a digitiser in simulation can be split into two parts; modeling the charge carrier transport in the detector and modeling the response of the chip that digitises the charge collection. For the carrier transport, the electron mobility (ease of carrier drift due to electric field) and the electric field in the sensor due to the bias voltage (external voltage applied to a p-n junction) are used to calculate the drift velocity of the carriers. From this, the drift time (time taken for the carrier to drift to the read-out edge) can be calculated, which is used to get the variance of a gaussian diffusion. These calculations are as follows [86]:

$$\mu_e = \frac{v_{sat}}{E_{crit}(1+(\frac{E_{field}}{E_{crit}})^{\beta})^{1/\beta}} \tag{5.1}$$

$$E_{field} = \frac{V_b - V_d}{w} + (1 - \frac{z}{w})\frac{2V_d}{w} \tag{5.2}$$

$$T_{drift} = \frac{w-z}{v_{drift}} = \frac{w-z}{-\mu_e E_{field}} \tag{5.3}$$

$$\sigma_{dw} = \sqrt{2\,T_{drift} D_n}. \tag{5.4}$$

Here, μ_e is the electron mobility, v_{sat} is the saturation velocity (maximum velocity of carriers at high electric fields) of the electrons in the semiconductor and defined as $v_{sat} = 1.53 \times 10^9 T^{-0.87}$ [86]. E_{crit} is the critical electric field (strength of electric field at which velocity saturation occurs) for electrons given by $E_{crit} = 1.01 T^{1.55}$, and $\beta = 2.57 \times 10^{-2} T^{0.66}$ is a phenomenological parameter [86]. The electric field in a semiconductor sensor can be approximated using a one dimensional electric field as in Eq. 5.2, where $V_b = 400$ V is the bias voltage, $V_d = 300$ V is the depletion voltage (magnitude of reverse bias voltage that fully depletes the semiconductor), w is the width of the sensor and z is the depth of the deposited charge. For fast simulations, Eq. 5.3 is used to calculate T_{drift}, but for a more accurate calculation, a Runge-Kutta-Fehlberg45 [87] integration over time from z to w is used. σ_{dw} is the variance associated with gaussian diffusion, with the electron diffusion coefficient (ease of carrier diffusion due to carrier density gradient) $D_n = 36.62$ cm^{2}s^{-1}, and is the variable used to calculate the amount of energy shared to neighbouring strips.

Calculating the shared energy is only done if the particle passed through the strip at a distance at least $3\sigma_{dw}$ from the edge of the strip. If the distance to the edge is greater than $3\sigma_{dw}$, then all the deposited energy goes into that strip. Sharing is then calculated through the use of error functions, and in order to conserve charge, the calculation is done for all the immediate neighbouring strips. The following is the formula used to calculate the shared energy:

$$E_s = \frac{E_{dep}}{4} \left(\mathrm{erf}\left(\frac{x_2 - x_h}{\sqrt{2}\sigma_{dw}} \right) - \mathrm{erf}\left(\frac{x_1 - x_h}{\sqrt{2}\sigma_{dw}} \right) \right) \left(\mathrm{erf}\left(\frac{y_2 - y_h}{\sqrt{2}\sigma_{dw}} \right) - \mathrm{erf}\left(\frac{y_1 - y_h}{\sqrt{2}\sigma_{dw}} \right) \right). \tag{5.5}$$

Here, E_s is the energy in a strip, E_{dep} is the total deposited energy, x_h and y_h are the co-ordinates of the particle. The boundaries of the strip are given by x_i and y_i. The radial geometry of the strips in the R0 sensor provided a challenge with the boundaries as the usual digitisers work with pixels/strips with constant x and y pitch and all the pixels/strips oriented at the same angle. The biggest challenge was at the boundary between the second and third row of strips where the angular pitch changes. Both the size and the number of strips change at this boundary, resulting in the strip boundaries not matching up. The R0 also has the channel numbering change direction at this boundary, so keeping the same x channel number when changing rows was not possible. To visualise what is meant by this, compare the two simple illustrations of the strip boundaries at the first and second row boundaries in Fig. 5.9. Some of the code for this digitiser is given in Appendix A.3. The energy in the strips is then converted to the amount of charge or signal per strip, C_{dep}. The ionisation energy of silicon is 3.6 eV, so an electron-hole pair in silicon is created for every 3.6 eV of energy deposited. The deposited charge is then put through a chip response function to replicate how a chip would process the signal. A CR-RC3 signal shaper response function was used and is given by:

Figure 5.9: Simple illustrations of the strip boundaries at the boundary between rows one and two (left) and the boundary between rows two and three (right). The boundaries on the right don't match up properly due to the change in strip number and width at this boundary.

$$Y = \frac{C_{dep}}{27} e^{3-t/\tau} \left(\frac{t}{\tau}\right)^3 . \tag{5.6}$$

The time constant τ is related to the peaking time of the pulse $T_p = 21$ ns via $\tau = T_p/3$ [88]. The time t is incremented from 0 to 25 ns until Y is greater than the threshold. If Y is greater than the threshold, then it would be considered as a hit and the channel number for that strip is output. Since the readout chips for the sensors are binary, i.e. there is either a hit or there isn't, the output data does not have information on the deposited energy or charge in the strip.

Chapter 6

Reconstruction and Analysis

6.1 Comparison of Reconstruction in Experiment and Simulation

The ROOT TGeo classes and methods used by the reconstruction software (EUTelescope) are very similar to the Geant4 classes and methods. So once the AllPix geometry was completed, only slight adjustments to the names of the classes and methods were neccesary. Originally the R0 sensor was defined in a file that was called by the GEAR file. The description evolved along side the AllPix description and so started out as a simple radial geometry with the focus on the origin. Once the accurate description was available, simple changes were made to some of the EUTelescope code in order to determine if the radial TGeo definition worked. Changes were made to the clustering step, the first step in the EUTelescope chain, to check if the channels coming from the simulation output were mapped to their corresponding position correctly through the use of a hitmap. An example of this hitmap is given in Fig. 6.1. Once these checks passed, the description file along with the clustering source file were sent to the ATLAS ITk strips group. The entire EUTelescope chain was altered by Xiaocong Ai [89] in order for it to be able to reconstruct data from the R0 sensor. The R0 description used in this new radial EUTelescope can be seen in Appendix B.1. The new radial EUTelescope was designed to reconstruct data from the testbeam, and not the simulation. Before any reconstruction of the simulation output was possible, a few changes to the reconstruction code were required. The software used to read out the data from the testbeam, EUDAQ2.0, was designed for the strip barrel modules, which have more readout chips than the R0 sensor. This resulted in two "ghost" chips in the data (the missing chips 20 and 21 in Fig. 5.4). This caused the channel numbers to run from 0-511 and then 767-1407, instead of 0-1151 in the outer two rows, and from 0-511 and 767-1279 instead of 0-1023 in the inner two rows (Fig. 5.4). This did not affect the data however, and ended up just creating a shift in the output by 256 channels, as each chip

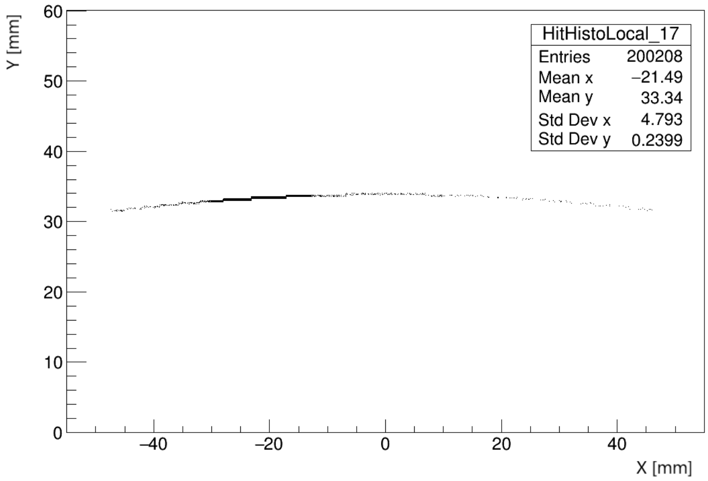

Figure 6.1: Histogram showing the two dimensional hitmap of the simulated R0 sensor in the sensor's local reference frame. Only the centre of the strip that registered a hit is shown, hence the thin band in the y direction. The denser area is where the beam was hitting, centred at (-21.5, 33.3) mm. The hits outside of the beam area are due to scattering.

reads out 128 channels per row. The EUDAQ software also reads out the information from each row in the R0 sensor as a separate sensor, along with a separate sensor for each timing window. Therefore the output had 12 "sensors" for the R0, 3 timing windows for before, during, and after the trigger and 4 rows per timing window. The output from the simulation did not have this shift in the channel numbering, so the numbering run normally from 0-N_{strips}, nor did it have the extra "sensors" due to the different timing windows. To test the simulation output, the simulated sensor was given an ID that matched the ID of the on-trigger timing window for the row in the experiment that was tested. The GEAR file for the simulation then had only 4 "sensors" as the DUT, whereas the experiment would have 12 "sensors" as the DUT. This did not effect the results as only 1 of the DUT "sensors" is reconstructed at a time. Strip sensors have elongated readout units and are intended to be used in pairs, oriented at a stereo angle to each other in order to calculate the second co-ordinate of the space point. Since only one R0 sensor was tested, no useful analysis of the reconstruction was possible in the radial direction, the reason for only analysing one row at a time. This meant that testing sharing between two adjacent rows of strips was not possible, only between the strips within one row at a time.

The first step in using the new radial EUTelescope for the reconstruction was to test whether the package had been built and installed correctly, and then to do a quick comparison of the experiment to simulation. The R0 sensor is not used in the track fitting stage of the reconstruction as the track fitting is meant to be done without the device under test. This is because we are testing whether the tracks of the particles, reconstructed using the Mimosa sensors, match with the hits on the device under test. After the track fitting step in the reconstruction, a file is created with the information of all the tracks. This file is used as input to a post-reconstruction analysis software which produces plots for the residuals, efficiencies and clustering. The residual

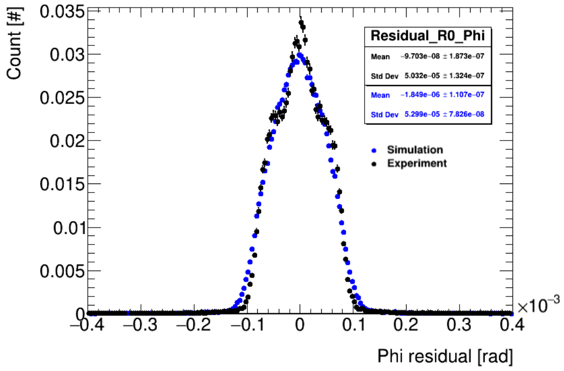

FIGURE 6.2: The residuals in phi, normalised to 1, for the R0 using the incorrect quick fix for the sharing. Residuals are calculated using track position minus hit position. The extra peak around zero is due to the clusters of size 2, which have better resolution. The black data is experiment while the blue is from simulation.

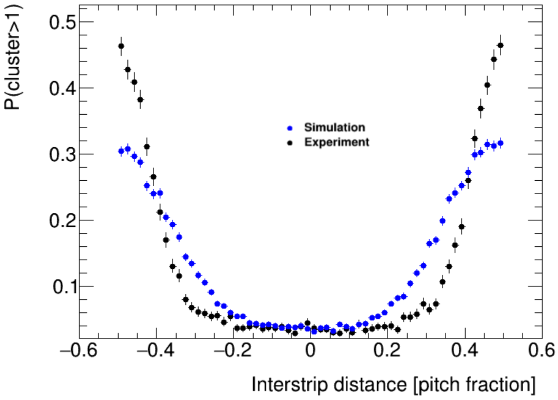

FIGURE 6.3: The interstrip clustering for the R0 after the channel numbering swap but before the correct threshold use. The black data is experiment while the blue is from simulation. Interstrip clustering is the probability of a cluster having a size greater than one as a function of the position of a track within a strip..

is the difference between the position of the hit, defined by the centre of the cluster, and the position of the reconstructed track at the sensor. Radial strips do not have a constant pitch in x, due to their fanning nature, so a resolution in the x-direction is difficult to define. Instead, since the strips have a constant angular pitch, a resolution in the phi direction would be better to use. The efficiency plots illustrate the probability of a track being reconstructed with a matching hit on the R0. The clustering plots give the probability of a cluster containing more than one strip. They are essentially a measure of the charge sharing in the sensor. The first reconstruction of the simulated data showed a discrepancy in relation to the experimental data. The simulation was over sharing and a simple fix was made to the digitiser to decrease the amount of sharing. This fix was used in the next paragraph, however, since this fix was later proven to be incorrect, it will not be discussed. The correct fix is discussed in Section 6.1.1.

The residual plot for the experiment and simulation data is shown in Fig. 6.2, with residuals of 50.32 ± 0.01 μrad and 53.00 ± 0.01 μrad respectively. The extra peak around zero is due to the clusters of size 2, due to these clusters having better resolution. The relatively large amount of clusters greater than 1 are due to the sensor operating at a low threshold in the experiment. The constant pitch in phi for the fourth row of the R0 sensor is ~ 171 μrad, giving a resolution of ~ 49 μrad. The standard deviation of the residuals for the data is reasonably close to this resolution. However, the simulation does notably worse than the experiment. The interstrip clustering shows how the probability of the cluster size being greater than 1 changes as we move from one side of a strip to the other. This is illustrated in Fig. 6.3. As can be seen, the simulation does not match well with the experimental data, despite the quick fix getting the overall sharing to match between simulation and experiment. Through discussions about this problem, it was decided to have a closer look at the digitiser.

6.1.1 Thresholds

Upon inspection of the digitiser, it was discovered that when checking if a strip was over threshold, the number of electrons in the strip was being compared to a threshold in femtocoulombs. Clearly the number of charged particles is not the same as the net charge of those particles, so this comparison was wrong. While scrutinising the digitiser, it was also noticed that the calculation of the electric field had an error. The correct calculation is given by equation 5.2, however the digitiser had a + instead of a − in the brackets. With these changes a proper comparison between the thresholds in the simulation and the testbeam thresholds was possible. The testbeam thresholds are defined in units of DAC, which is an internal unit used by the EUDAQ system. The conversion from DAC to amount of charge (in femtocoulomb) is beyond the scope of this thesis, though a conversion was done by the ITk strips testbeam group [90]. A fit was performed on those converted values relating the threshold in DACs (T_{DACs}) to a threshold in femtocoulombs (T_{fC}):

$$T_{fC} = 6.71 \times 10^{-7} T_{DACs}^3 - 1.02964 \times 10^{-4} T_{DACs}^2 + 0.0360064 94 T_{DACs} - 0.56764143. \quad (6.1)$$

As this is only an approximate fit, the physical meaning of the co-efficients are unknown. This equation was used to calculate the thresholds used in the simulations in this thesis.

An issue that arises in the experiment due to the manner in which the telescope works is that of desynchronisation. Desynchronisation occurs when the various triggers from the sensors don't match up, often due to a busy signal from the FEI4 readout. This desynchronisation prevents proper data taking and can be seen in the plots of efficiency against event number, for example Fig. 6.4(a). To remove the effects of this, those events found to have the desynchronisation are removed from the analysis. Another issue with low efficiencies is due to the disabled chips. Shown in Fig. 6.4(b) is the efficiency per channel number for a run where part of the beam was hitting the sensor where a disabled chip was reading out. The channel numbers in question are those below 512 in Fig. 6.4(b), corresponding to chip 19 in the third row of Fig. 5.4. Since the chip is disabled, no data was taken for the R0 from those strips and so the efficiency is zero. The particular run shown in Fig. 6.4(b) will be discussed later on.

6.1.2 Beam Profiles

Having a look at the profiles of the beams, there are two different profiles to look at; those of the hits and those of the tracks. In Fig. 6.5 is the comparison of the hitmap of the hits for the first Mimosa plane while Fig. 6.6 has the comparison for the reconstructed tracks hitmap at the R0 sensor. The hits on the first Mimosa were used as there is very little scattering at this point

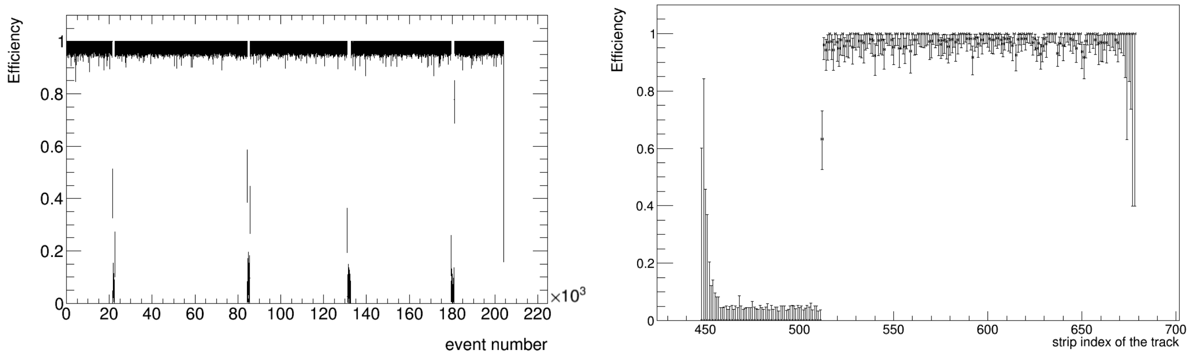

(a) (b)

FIGURE 6.4: Plots of the efficiency vs the event number (a), and the channel number (b) for two different experimental runs. The drops in efficiency in the left plot illustrate the desynchronisations that can occur during a run, while the large section of low efficiency in the right plot is due to a disabled chip on the module.

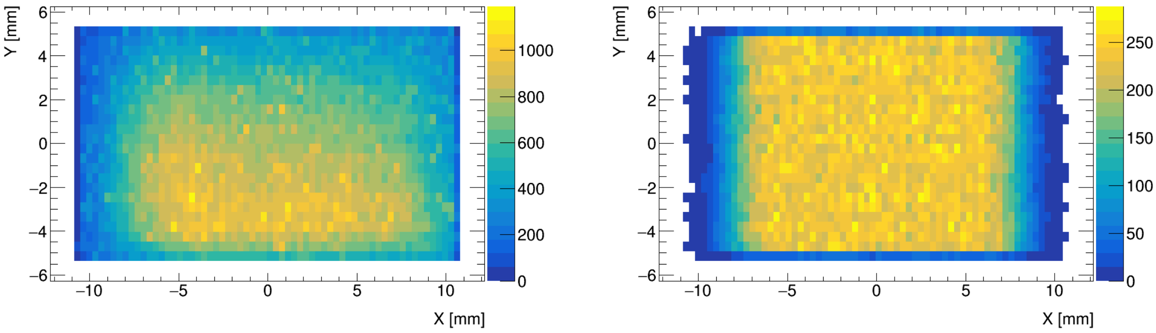

(a) (b)

FIGURE 6.5: Beam profiles using the hit map on the first Mimosa plane for the experimental (a) and simulation (b) data.

and the Mimosa has high granularity. The hitmaps of the hits and the tracks for the simulation are quite evenly spread over the beam while the experiment has some “hotspots” in the profiles, which are more pronounced in the tracks hitmap. There is also a big difference between the tracks and hits hitmap for the experiment (Figs. 6.5(a) and 6.6(a)), while the simulation is quite consistent between the two (Figs. 6.5(b) and 6.6(b)). The simulation of the telescope has some simplifications compared to the actual telescope, for example there is less material simulated in the telescope, a less complex beam profile and only one electron simulated per event. This is most likely why the track finding is more efficient in the simulation and why there is a greater difference between the hits and track hitmaps of the experiment compared to the simulation. The differences in the beam between experiment and simulation however had no effect on the results of this thesis since the beam profiles did not play a role in the tests performed.

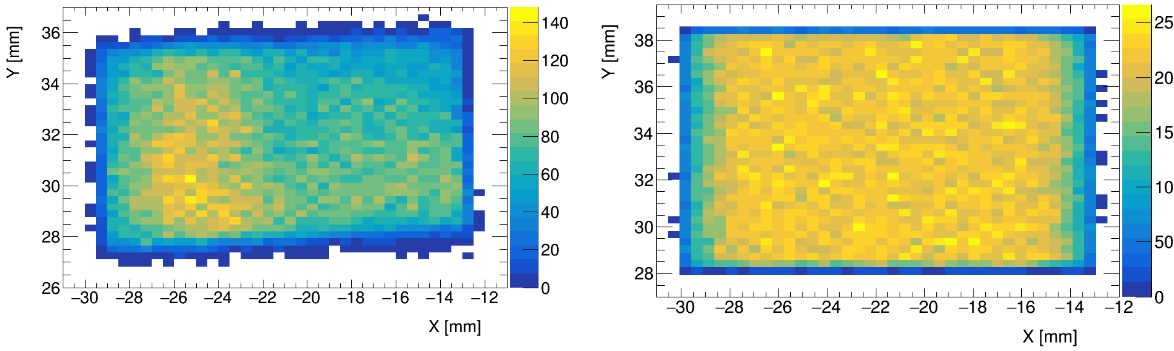

(a) (b)

FIGURE 6.6: Beam profiles using the reconstructed tracks at the position of the R0 and in the R0's local reference frame for the experimental (a) and simulation (b) data.

6.2 R0 Sensor Analysis

For the final results, 3 different run positions were chosen, corresponding to the three blue dots in Fig. 5.4. This allowed the testing of all four rows and variation in the x-direction of the sensor. Four different thresholds will also be shown for the run in the fourth row to show how the threshold affects the readouts. Also to be discussed will be a comparison of the Monte Carlo tracks to the reconstructed tracks.

6.2.1 Main Position and Threshold

The first results to be discussed will be for those of the run used for most of the reconstruction analysis and simulation testing, as the experimental run had a very good reconstruction. This pertains to the high detailed run at $(-19, 33)$ mm (the blue dot in the fourth row of Fig. 5.4), with a threshold of 0.75 fC (40 DACs). The simulation had 250000 events while the experiment had 200000. Just in terms of the alignment, Fig. 6.7(a) shows the index residual for the experiment and simulation. As can be seen, there is good alignment for both, but the slight increase at zero and decrease at plus and minus one for the simulation is due to a slightly lower sharing which will be discussed in detail later. Figure 6.7(b) shows the interstrip efficiency of both the experiment and simulation to be close to 1, which is what we expect at this threshold. The interstrip efficiency, much like the interstrip sharing, shows the probability of a hit being recorded given a track as we move from one side of a strip to the other. The cluster sizes are shown in Fig. 6.8(a). A slight drop at the cluster size of two for the simulation can be seen as the experiment has a probability of sharing equal to $12.80\% \pm 0.18\%$ while the simulation has $12.48\% \pm 0.08\%$. The effects on clusters of size greater than two were not looked at as in the simulation a sharing is only done to the nearest neighbours, sharing to the second nearest neighbour is not performed. Since experiment and simulation matched well for these large cluster sizes, it can be assumed that these clusters are primarily due to extra particles originating from the electron beam scattering. The uncertainties are purely statistical and based on Poisson statistics. The systematic uncertainties from charge propagation and the conversion of the thresholds in DAC to femtocoulomb were not taken into account. The interstrip sharing, in Fig. 6.8(b) matches well between experiment and simulation however the simulation is slightly higher near the strip edges and lower at the bends around plus minus 0.3. This is most likely due to the simulation having a “cleaner” charge sharing as no noise or random affects are added in the propagation of the charges in the simulation. The interstrip sharing also shows how the probability of sharing in the central region of the strip is constantly very low and that it increases as the incident particle gets closer to the edge. The phi residual is given in Fig. 6.9. The experiment and simulation match very well, and both have a clear secondary peak due to clusters of size greater than one. This double peak feature is due to the lower threshold of this run, and is made evident in Fig. 6.10 which shows a phi residual plot for clusters of size one (6.10(a)) and a plot for clusters of size greater than one (6.10(b)). The expected phi resolution for the strips in this row is $\sim 4.9 \times 10^{-5}$ rad. The standard deviation of both simulation and experiment are slightly lower than this since the threshold is low and sharing is relatively high. For this particular run, the simulation and experiment match very well geometrically, but the simulation has slightly less sharing. The difference in sharing could be due to the simplification used in the digitiser, for example the one dimensional electric field, no use of noise or random gaussian spreads in the threshold and only modeling the transport of electrons. The temperature and voltages may have fluctuated enough during the experiment to cause non-negligible effects that aren’t modeled in the simulation.

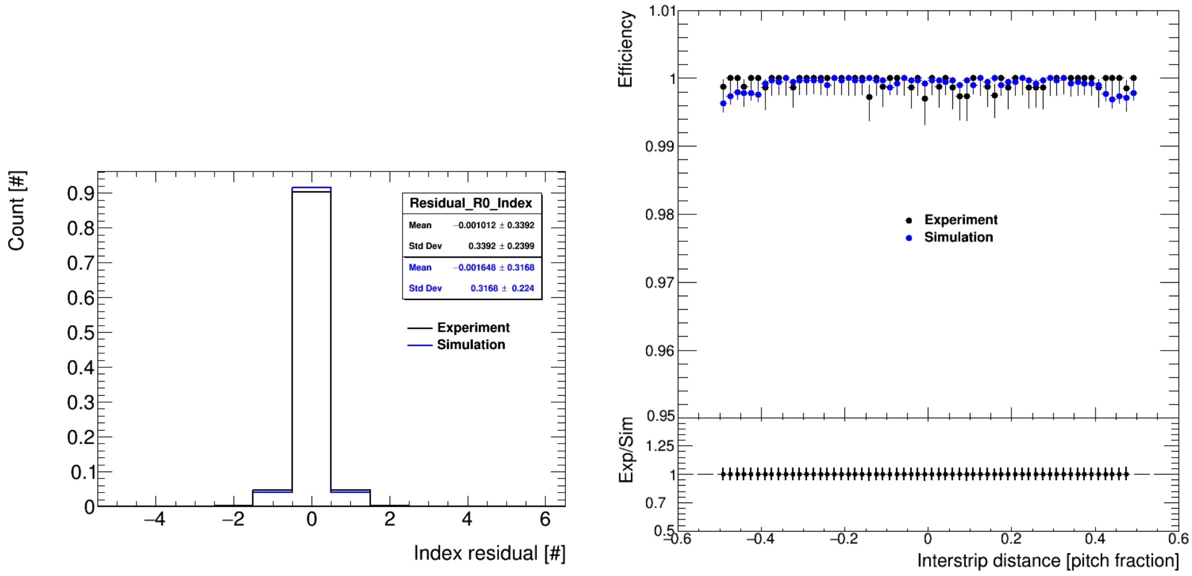

(a) (b)

FIGURE 6.7: Plots of the index residual (track_index - hit_index) using integer indeces, normalised to 1 (a), and interstrip efficiency (b), at a threshold of 0.75 fC and angular pitch of 171.8368 mrad. The efficiencies are 0.999 ± 0.003 for the simulation and 0.999 ± 0.007 for the experiment. Interstrip efficiency is the probability of a hit being recorded, given a reconstructed track, as a function of the position of a track within a strip. The bottom plot in (b) shows the ratio of experiment (Exp) to simulation (Sim).

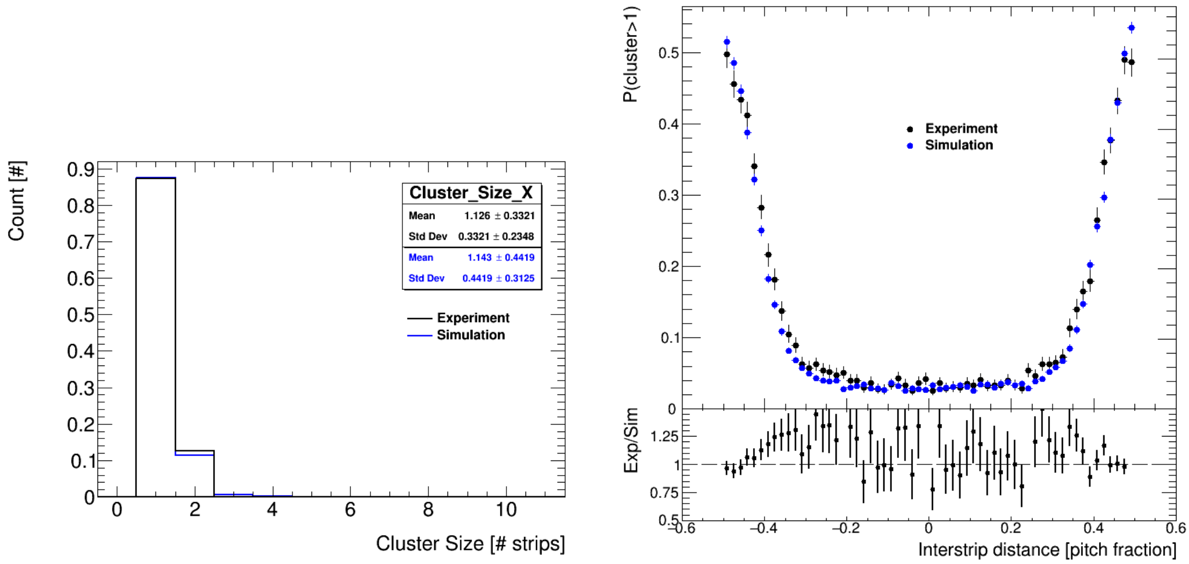

(a) (b)

FIGURE 6.8: Plots of the cluster sizes normalised to one (a) and the interstrip clustering (b), at a threshold of 0.75 fC and angular pitch of 171.8368 mrad. Interstrip clustering is the probability of a cluster having a size greater than one as a function of the position of a track within a strip. The bottom plot in (b) shows the ratio of experiment (Exp) to simulation (Sim).

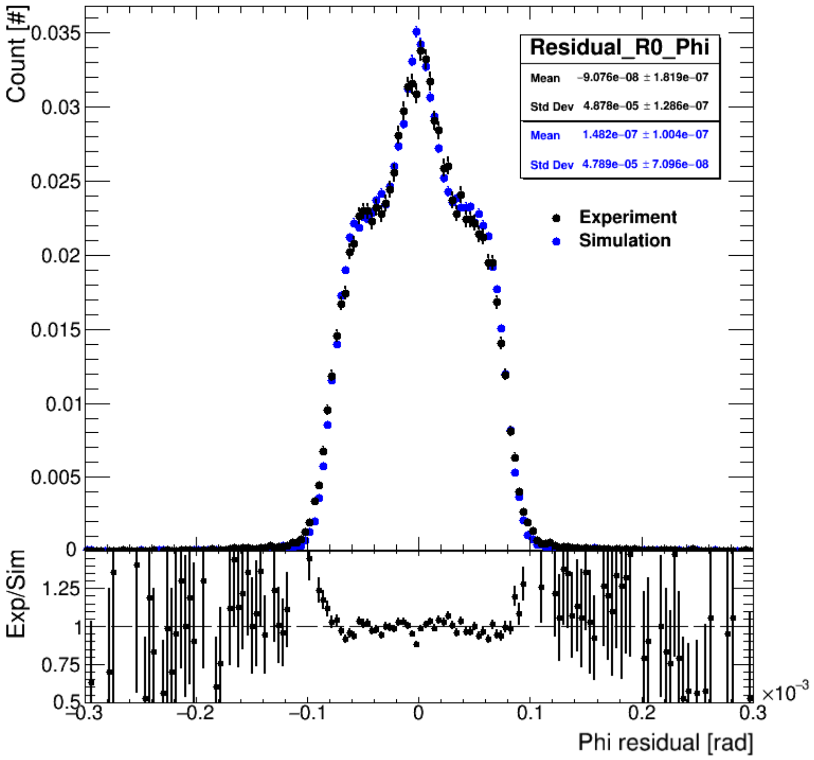

FIGURE 6.9: The phi residual (track - hit) for the R0 corresponding at 0.75 fC threshold and angular pitch of 171.8368 mrad. The secondary peak is due to clusters of size greater than one. They are both normalised to one. The bottom plot shows the ratio of experiment (Exp) to simulation (Sim).

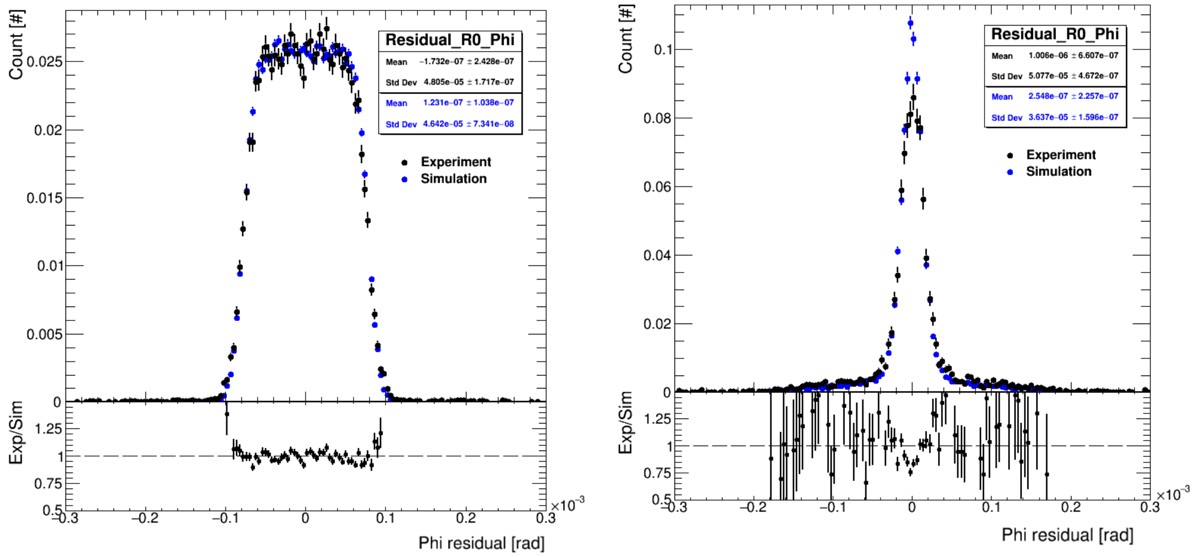

(a)

(b)

FIGURE 6.10: The phi residuals (track - hit) for the R0 corresponding to clusters of size one (a) and clusters of size two (b), at 0.75 fC threshold and angular pitch of 171.8368 mrad. They are all normalised to one. The bottom plot in both figures shows the ratio of experiment (Exp) to simulation (Sim).

6.2.2 Different Thresholds

All the following thresholds had 250000 events in the simulation and 200000 in the experiment. At the same position of the run in section 6.2.1, the threshold was increased to 1.62 fC (68 DACs). The probability for sharing for this threshold was found to be 5.66% ± 0.05% for the simulation and 4.92% ± 0.10% for the experiment. The sharing in the simulation has now gone above the experiment by more than 0.7%. The reason is not fully understood but may be due to slight inaccuracies in the conversion from DAC to fC. The interstrip sharing and efficiency are given in Figs. 6.11(a) and 6.11(b) respectively. The efficiency and sharing have started to drop off at the edges, with the experimental efficiency dropping more. The phi residual for this threshold is shown in Fig. 6.12. The secondary peak has gotten smaller and the standard deviation has increased due to the higher threshold, but the two samples still overlap quite well.
Next is the threshold of 2.33 fC (90 DACs). The probability for sharing for this threshold was found to be 2.98% ± 0.04% for the simulation and 2.78% ± 0.08% for the experiment. The difference in the probability of sharing has decreased. The interstrip sharing and efficiency are given in Figs. 6.13(a) and 6.13(b) respectively. The efficiency has dropped considerably at the edges for both samples, while the centres are still around one. The phi residual is shown in Fig. 6.14. The secondary peak has completely disappeared at this threshold.
The final threshold studied was 3.05 fC (110 DACs). The probability for sharing for this threshold was found to be 2.1%±0.03% for the simulation and 2.31%±0.10% for the experiment. The sharing in the experiment is now slightly higher than the simulation again, though statistical fluctuations are most likely starting to take effect at this threshold. The interstrip sharing and efficiency are given in Figs. 6.15(a) and 6.15(b) respectively. The efficiency has dropped even more so at the edges for both samples, however the central part of the experiment has now dropped to around 0.85. The amount of charge deposited in a strip even at the centre of a strip is now starting to be lower than the threshold for the experiment. The amount of signal charge deposited in the sensor is around 4 fC, due to the ∼25000 ionised electrons arising from the electron-hole creation of $\sim 80/\mu$m. If the sensor and the DAQ were perfect, the efficiency of the sensor would be a step function, dropping from one to zero at a threshold equal to the signal charge. However, electronic noise creates a spread in the step function, representing an s-curve [34]. This can be seen in Fig. 6.17, which shows the efficiency versus threshold (s-curve) for one of the R0 chips in the testbeam. At a threshold of around 3.05 fC, the efficiency has dropped to below 0.9. Since there is no noise in the simulation this effect will not be seen and the efficiencies are expected to have a sharper drop when the threshold is much closer to the signal charge. This is why the efficiency at a threshold of 3.05 fC is close to one in the central region of the interstrip efficiency, where the effects of the sharing are negligible. The interstrip sharing has lost the constant sharing in the central region as the edge peaks have moved more central. The phi residual is shown in Fig. 6.16. The experimental residual has started to round off at the centre, while the simulation has flat topped. This is most likely due to some of the

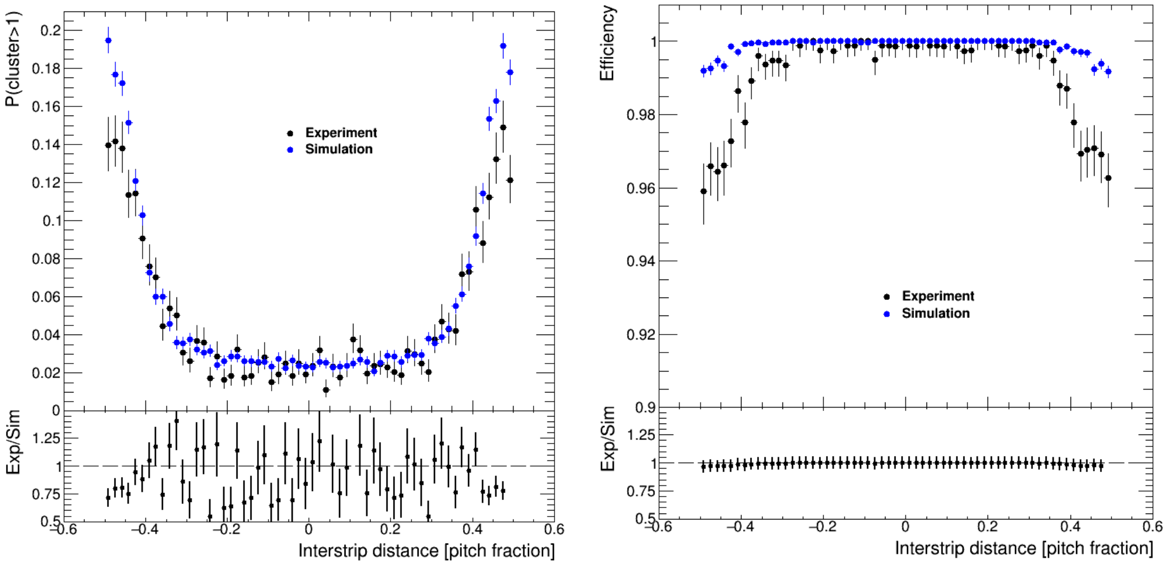

(a)

(b)

FIGURE 6.11: Plots of the interstrip cluster size (a) and the interstrip efficiency (b), at a threshold of 1.62 fC and angular pitch of 171.8368 mrad. The average efficiencies are 0.999 ± 0.003 and 0.992 ± 0.007 for the simulation and experiment respectively. Interstrip efficiency is the probability of a hit being recorded given a reconstructed track, interstrip clustering is the probability of a cluster having a size greater than one; both as a function of the position of a track within a strip. The bottom plot in both figures shows the ratio of experiment (Exp) to simulation (Sim).

electrons in the experiment depositing charge lower than the threshold which does not occur in the simulation since a mono-energetic beam is used in simulation.

In order to compare these different thresholds better, separate comparison plots of the experiment (simulation) for the residuals can be seen in Fig. 6.18(a) (6.18(b)), the interstrip clustering is in Fig. 6.19(a) (6.19(a)) and the interstrip efficiency is in Fig. 6.20(a) (6.20(a)). They illustrate quite well how an increase in the threshold effects the results, reducing the efficiency and sharing.

6.2.3 Different Positions

Changing rows, the next position is $(16, -41)$ mm (the blue dot in the first row of Fig. 5.4) at a threshold of 0.75 fC (40 DACs). The simulation had 250000 events while the experiment had 100000. The probability for sharing for this run was found to be $13.23\% \pm 0.08\%$ for the simulation and $14.13\% \pm 0.28\%$ for the experiment. The sharing is off by 0.9%, but both are higher than the previous position at the same threshold. The strips are narrower at this point (~ 0.077 mm compared to ~ 0.081 mm) and so a higher probability of sharing is expected. Since the propagation of charge is essentially independent of strip size, there will be more charge shared as the strip that had the incident particle will collect less charge when the pitch is smaller. The

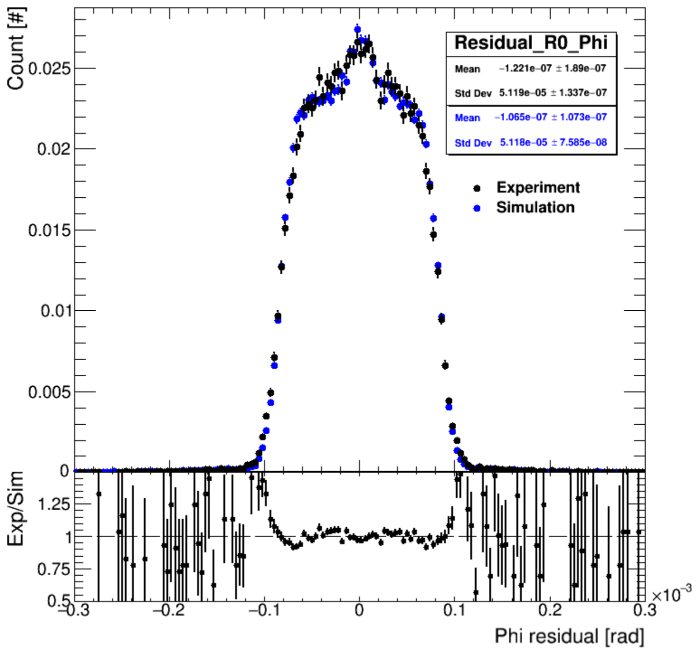

FIGURE 6.12: The phi residual (track - hit) for the R0 corresponding to 1.62 fC threshold and angular pitch of 171.8368 mrad. The secondary peak is due to clusters of size greater than one. They are both normalised to one. The bottom plot shows the ratio of experiment (Exp) to simulation (Sim).

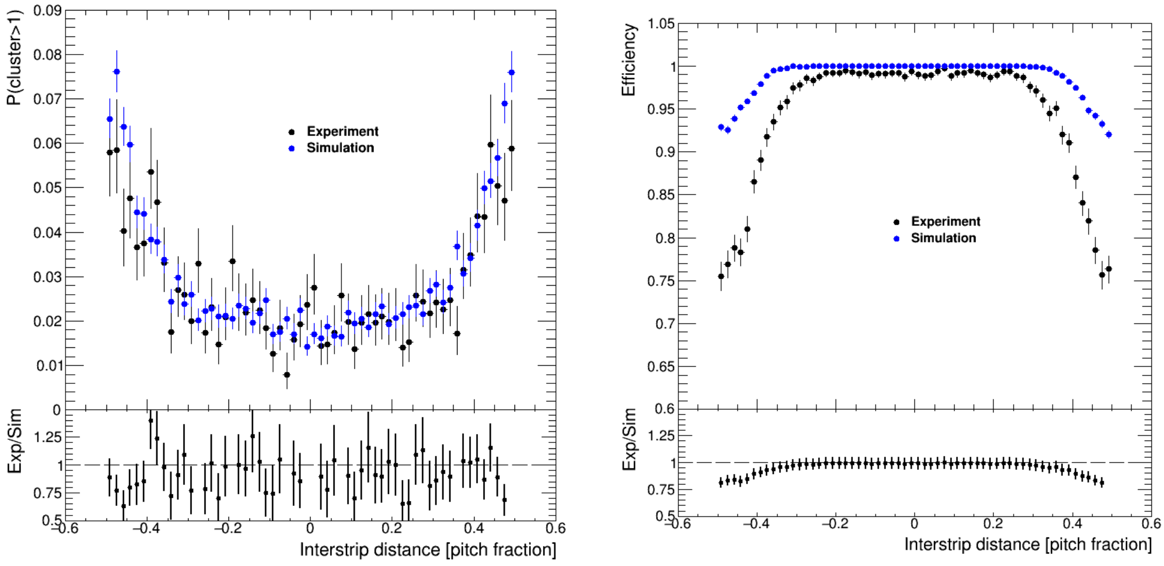

(a) (b)

FIGURE 6.13: Plots of the interstrip cluster size (a) and the interstrip efficiency (b), at a threshold of 2.33 fC and angular pitch of 171.8368 mrad. The average efficiencies are 0.988 ± 0.003 and 0.942 ± 0.006 for the simulation and experiment respectively. Interstrip efficiency is the probability of a hit being recorded given a reconstructed track, interstrip clustering is the probability of a cluster having a size greater than one; both as a function of the position of a track within a strip. The bottom plot in both figures shows the ratio of experiment (Exp) to simulation (Sim).

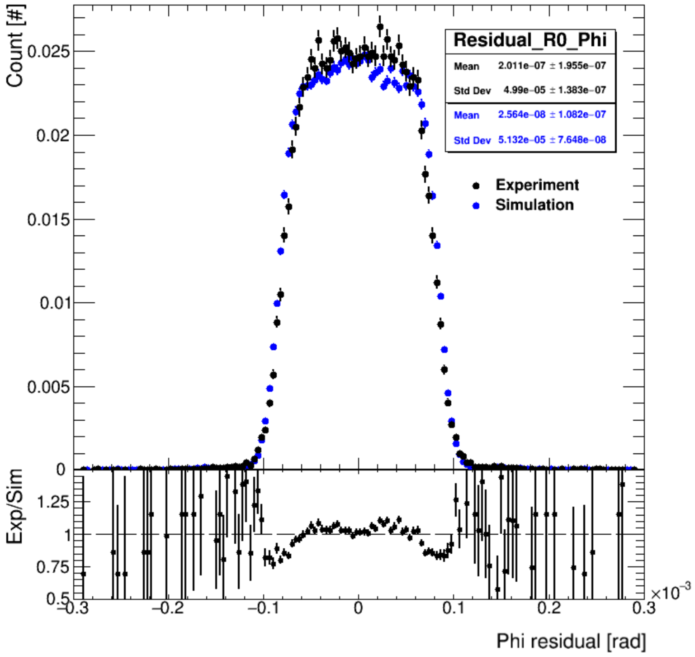

FIGURE 6.14: The phi residual (track - hit) for the R0 corresponding at 2.33 fC threshold and angular pitch of 171.8368 mrad. The secondary peak due to clusters of size greater than one is now absent. They are both normalised to one. The bottom plot shows the ratio of experiment (Exp) to simulation (Sim).

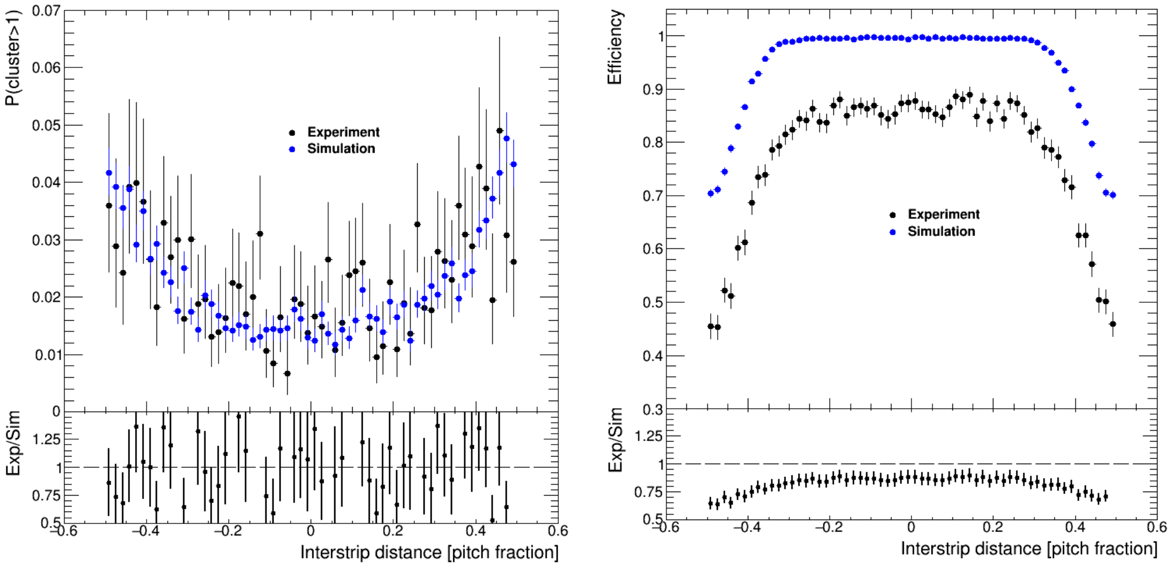

(a) (b)

FIGURE 6.15: Plots of the interstrip cluster size (a) and the interstrip efficiency (b), at a threshold of 3.05 fC and angular pitch of 171.8368 mrad. The average efficiencies are 0.943 ± 0.003 and 0.776 ± 0.007 for the simulation and experiment respectively. Interstrip efficiency is the probability of a hit being recorded given a reconstructed track, interstrip clustering is the probability of a cluster having a size greater than one; both as a function of the position of a track within a strip. The bottom plot in both figures shows the ratio of experiment (Exp) to simulation (Sim).

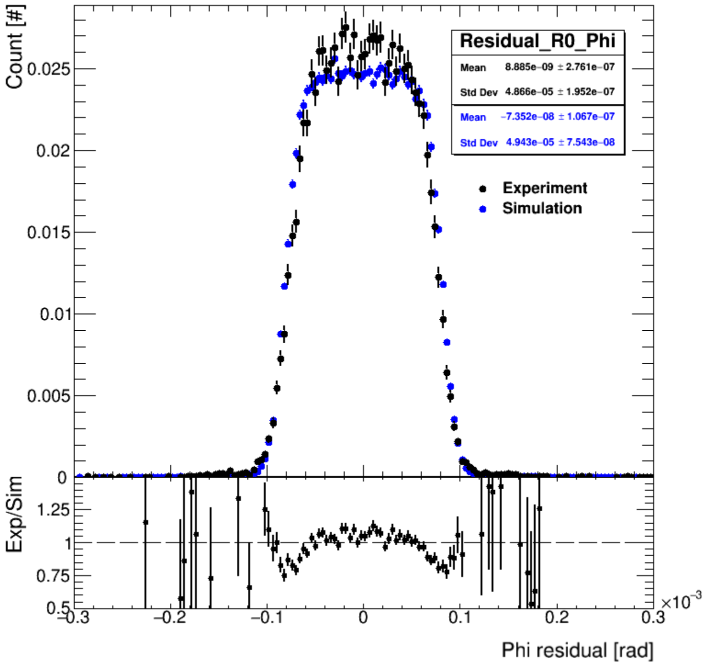

FIGURE 6.16: The phi residual (track - hit) for the R0 corresponding at 3.05 fC threshold and angular pitch of 171.8368 mrad. The secondary peak due to clusters of size greater than one is now absent. They are both normalised to one. The bottom plot shows the ratio of experiment (Exp) to simulation (Sim).

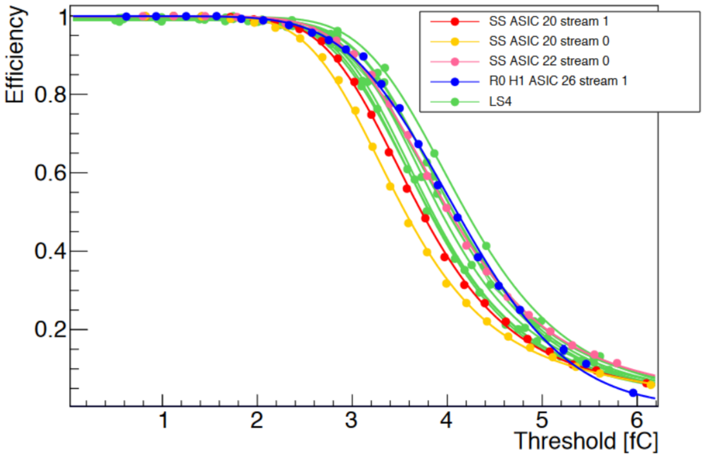

FIGURE 6.17: Plots of the efficiency versus threshold for various strips sensors [91]. The Short Strip (SS) and R0 sensors were tested at the May 2017 testbeam at DESY, while the Long Strip (LS4) sensor was tested at the testbeam prior to that. The threshold at 50% efficiency represents the charge of the signal, which for the R0 is around 4 fC.

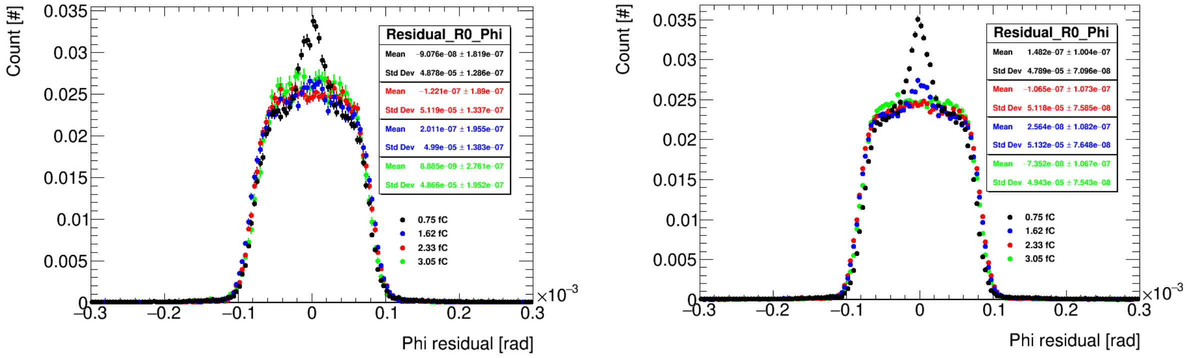

(a) (b)

FIGURE 6.18: Plots of the phi residuals (track - hit) for four different thresholds at the same position for experiment (a) and simulation (b). All have been normalised to one.

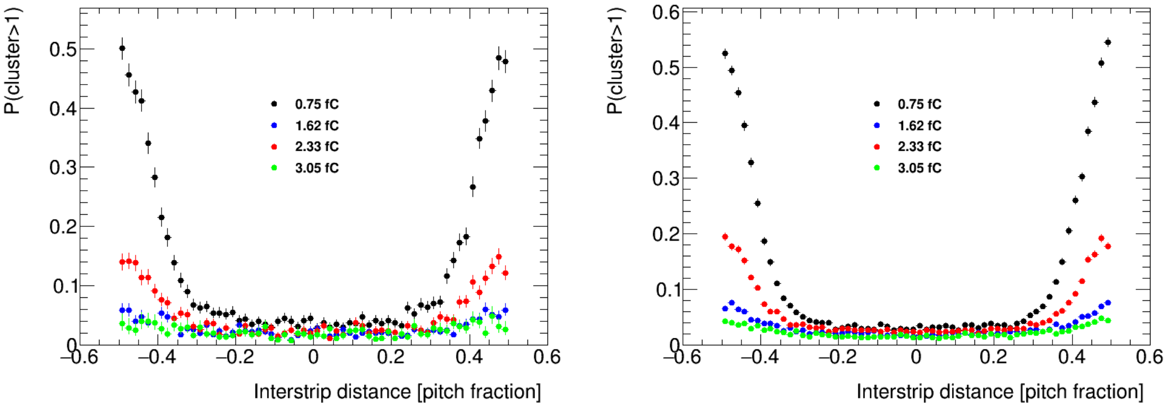

(a) (b)

FIGURE 6.19: Plots of the interstrip clustering for four different thresholds at the same position for experiment (a) and simulation (b). Interstrip clustering is the probability of a cluster having a size greater than one as a function of the position of track within a strip.

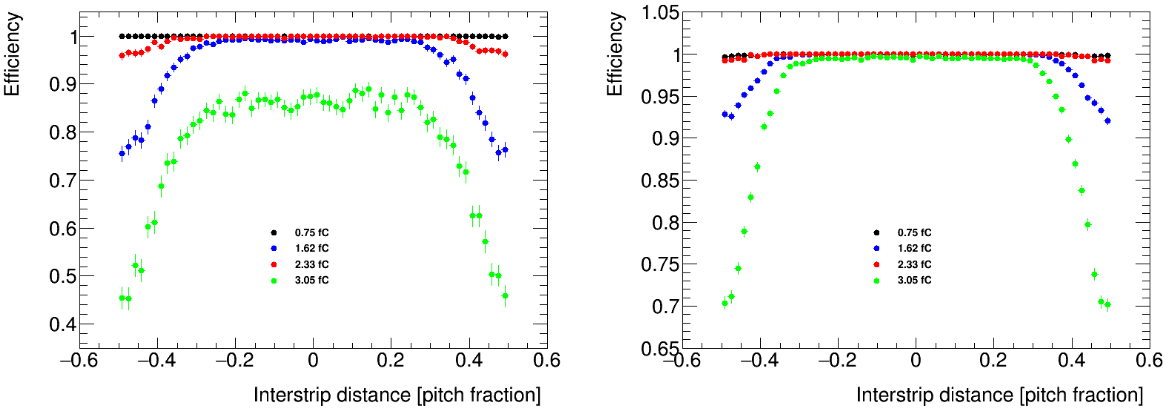

(a) (b)

FIGURE 6.20: Plots of the interstrip efficiency for four different thresholds at the same position for experiment (a) and simulation (b). Interstrip efficiency is the probability of a hit being recorded, given a reconstructed track, as a function of the position of a track within a strip.

experiment may be so far off the simulation due to the noisy chip, which could increase the signal over the threshold especially at this low threshold. The interstrip sharing and efficiency is given in Figs. 6.21(a) and 6.21(b) respectively. The efficiencies are close to one, but the experiment is lower than the same threshold at the other position. This can be explained since the beam overlapped with a noisy chip (chip 22 in 5.4). The phi residual for this run is shown in Fig. 6.22. The two samples overlap very well and both have a prominent second peak. The width of the residuals is larger than the previous position since the angular pitch of the strips in this row in larger (193.3 mrad vs 171.8 mrad).

The final position studied was at $(1, -11)$ mm (the blue dot in the centre of Fig. 5.4). Unfortunately this was the only position that tested the second and third rows, and the beam overlapped with a disabled chip in the third row and a noisy chip in the second row. The threshold for this run was 0.9 fC (45 DACs). The simulation had 500000 events while the experiment had 200000, resulting in around 250000 simulated events and 100000 experimental events per row. Looking at the results for the second row, the probability for sharing was $10.97\% \pm 0.07\%$ for the simulation and $11.16\% \pm 0.17\%$ for the experiment. The difference between the two samples is only 0.2% and why they are as low as they are is because the threshold is slightly higher than the 0.75 fC in the first hi-detailed run analysed, and the strips are slightly wider at this point (~ 0.082 mm). The interstrip sharing and efficiency is given in Figs. 6.23(a) and 6.23(b) respectively. The simulation is higher at the edges but lower at the bends for the interstrip sharing, which could possibly be due to the noisy chip in the experiment allowing sharing to occur further within the strip. For the interstrip efficiency, the experiment is far lower than expected which could possibly be due to the noisy chip in the experiment and that the beam is spread over two rows. A lot of the events in the experiment had hits from the other DUT “sensors” (out of trigger time but mostly from the third row) passing the reconstruction, which reduced the efficiency. Why they passed the reconstruction is unknown. The phi residual for this run is shown in Fig. 6.24. The experimental results have a larger residual while the simulation is quite sharp. Overall the experimental results for this run were not very good, possibly due to the noisy chip and that the beam was hitting the edge of the row of strips. This may have resulted in a reconstruction that was not as good as the other runs.

Moving to the results for the third row, probability for sharing was $12.04\% \pm 0.08\%$ for the simulation and $13.12\% \pm 0.48\%$ for the experiment. Although the strips are at their narrowest here (~ 0.074 mm), the higher threshold seems to have overall reduced the sharing from the first hi-detailed run. There is also a large difference of 1% between the sharing. The effects of the disabled chip can be seen in 6.4(b), where the strips readout by the disabled chip have zero efficiency. The interstrip sharing and efficiency is given in Figs. 6.25(a) and 6.25(b) respectively. The simulation and experiment overlap decently in the interstrip clustering and the sharing edge cuts in more since the strips are narrower here so the ratio of sharing distance to strip width is larger. For the interstrip efficiency the simulation is essentially one while the experiment is far below at about 0.75 which may possibly be due to the disabled chip and that the beam is

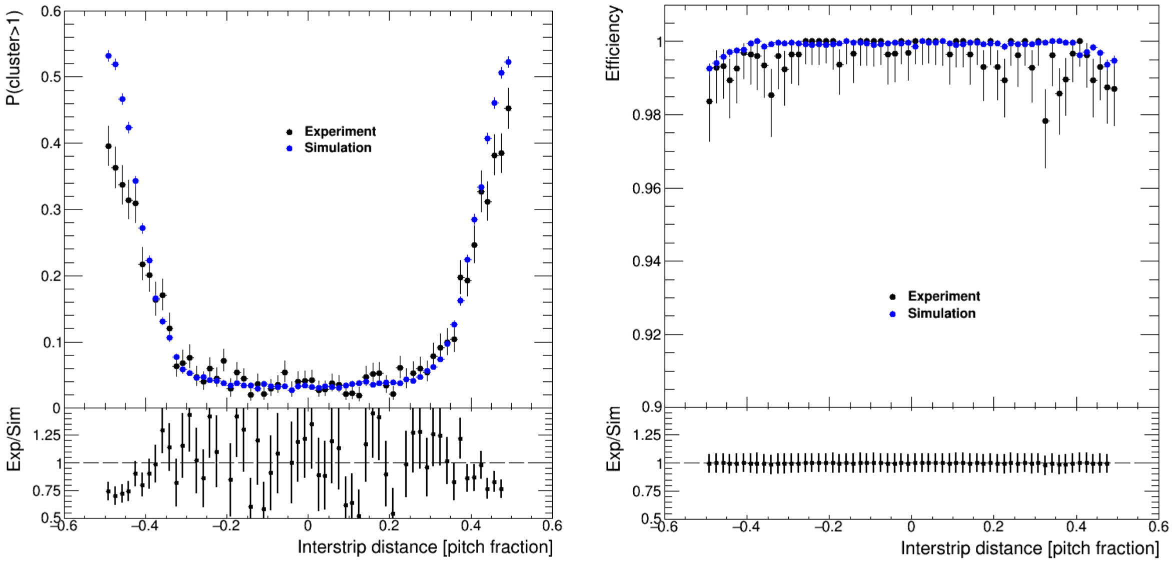

(a)

(b)

FIGURE 6.21: Plots of the interstrip cluster size (a) and the interstrip efficiency (b), at a threshold of 0.75 fC and angular pitch of 193.2745 mrad. The average efficiencies are 0.999 ± 0.003 and 0.996 ± 0.011 for the simulation and experiment respectively. Interstrip efficiency is the probability of a hit being recorded given a reconstructed track, interstrip clustering is the probability of a cluster having a size greater than one; both as a function of the position of a track within a strip. The bottom plot in both figures shows the ratio of experiment (Exp) to simulation (Sim).

spread over two rows. This row had the same problems as the previous row where alot of other DUT “sensors” passed the reconstruction. The phi residual for this run is shown in Fig. 6.26. Despite the effects of the disabled chip and low statistics, the two samples overlap fairly well and both have a double peak. The two different positions from row 4 and row 1 have their own angular pitches. To illustrate the difference in the pitches, comparisons of the residuals for these positions are shown in Figs. 6.27(a) and 6.27(b) for the experiment and simulation respectively. As can be seen, the residuals for row 1 (a pitch of 0.193 mrad) are wider than those for row 4 (a pitch of 0.171 mrad). A summary of the above results, showing the residuals, sharing and efficiency for the seven different comparisons is given in Table 6.1.

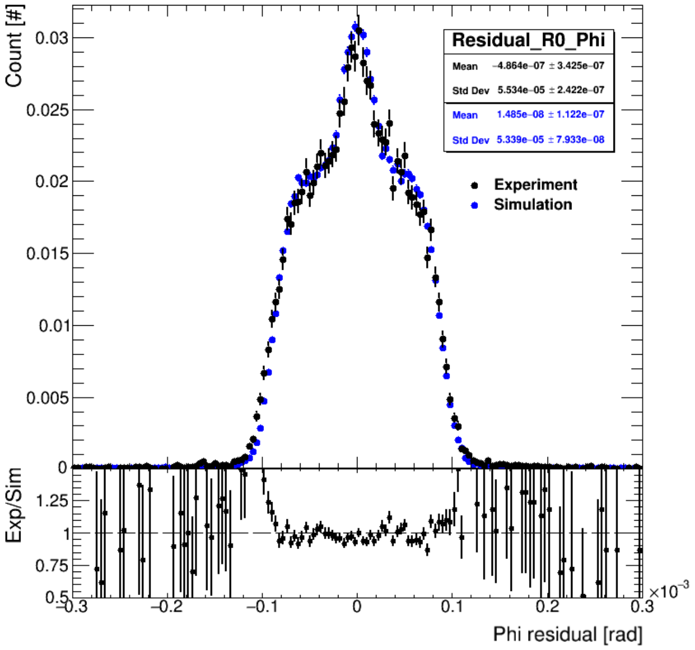

FIGURE 6.22: The phi residual (track - hit) for the R0 corresponding at 0.75 fC threshold and angular pitch of 193.2745 mrad. The secondary peak is due to clusters of size greater than one. They are both normalised to one. The bottom plot shows the ratio of experiment (Exp) to simulation (Sim).

TABLE 6.1: Summary of the experimental (Exp) and simulation (Sim) results for the different positions and thresholds. Shown is the resolution from the residuals, the probability of sharing, and the efficiency. All uncertainties are statistical.

Position (x,y) [mm]	**Threshold [fC]**	**Residual Exp(Sim) [μrad]**	**Sharing Exp(Sim) [%]**	**Efficiency Exp(Sim)**
(-19,33) row 4	0.75	48.78±0.13 (47.89±0.07)	12.80±0.18 (12.48±0.08)	0.999±0.007 (0.999±0.003)
	1.62	51.19±0.13 (51.18±0.08)	4.92±0.1 (5.66±0.05)	0.992±0.007 (0.999±0.003)
	2.33	49.90±0.14 (51.3±0.08)	2.78±0.08 (2.98±0.04)	0.942±0.006 (0.988±0.003)
	3.05	48.66±0.20 (49.43±0.08)	2.31±0.1 (2.10±0.03)	0.776±0.007 (0.943±0.003)
(16,-41) row 1	0.75	55.34±0.24 (53.39±0.08)	14.13±0.28 (13.23±0.08)	0.996±0.011 (0.999±0.003)
(1,-11) row 2	0.9	56.06±0.20 (51.85±0.08)	11.16±0.17 (10.97±0.07)	0.661±0.005 (0.998±0.003)
(1,-11) row 3	0.9	50.26±0.30 (48.63±0.08)	13.12±0.48 (12.04±0.08)	0.749±0.012 (0.999±0.003)

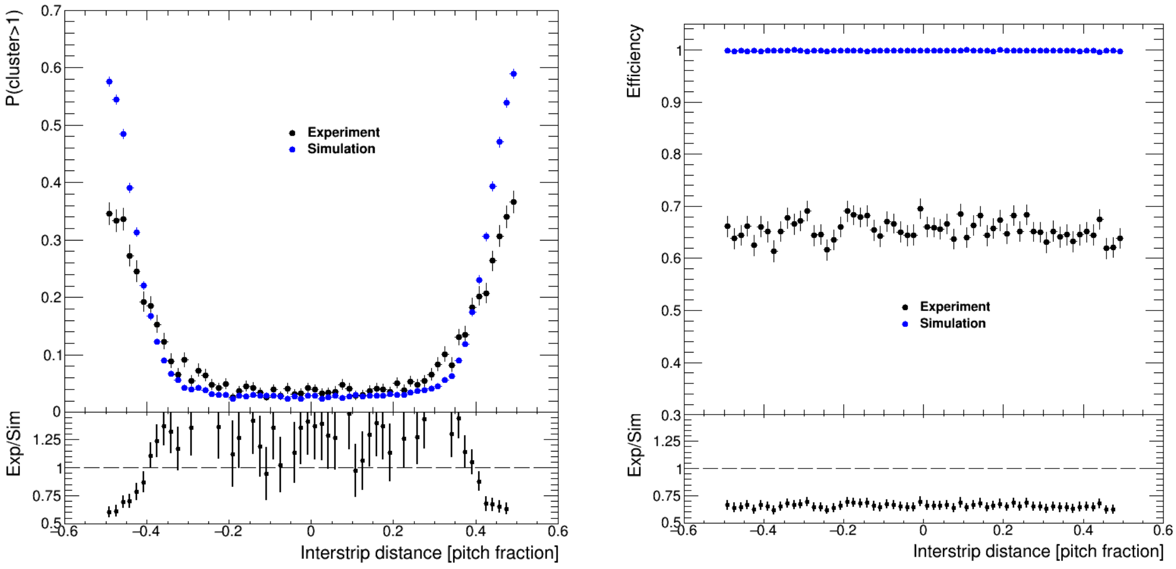

(a) (b)

Figure 6.23: Plots of the interstrip cluster size (a) and the interstrip efficiency (b), at a threshold of 0.9 fC and angular pitch of 193.2745 mrad. The average efficiencies are 0.998±0.003 and 0.661 ± 0.005 for the simulation and experiment respectively. Interstrip efficiency is the probability of a hit being recorded given a reconstructed track, interstrip clustering is the probability of a cluster having a size greater than one; both as a function of the position of a track within a strip. The bottom plot in both figures shows the ratio of experiment (Exp) to simulation (Sim).

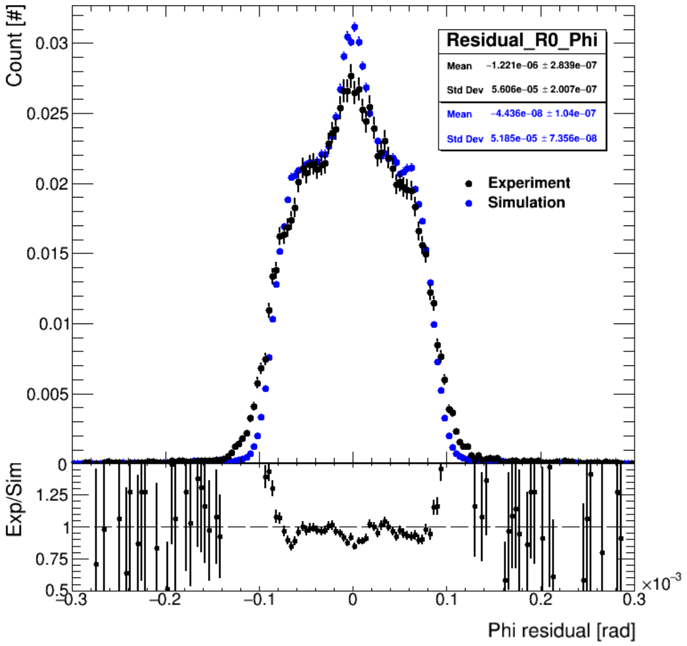

Figure 6.24: The phi residual (track - hit) for the R0 corresponding at 0.9 fC threshold and angular pitch of 193.2745 mrad. The secondary peak is due to clusters of size greater than one. They are both normalised to one. The bottom plot shows the ratio of experiment (Exp) to simulation (Sim).

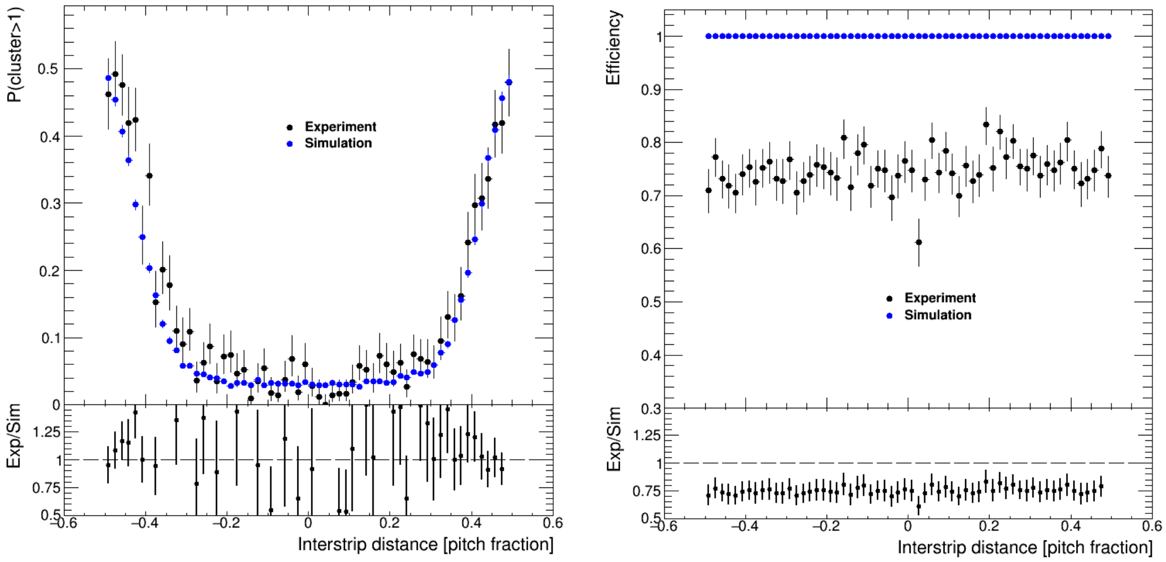

(a) (b)

FIGURE 6.25: Plots of the interstrip cluster size (a) and the interstrip efficiency (b), at a threshold of 0.9 fC and angular pitch of 171.8368 mrad. The average efficiencies are 0.999±0.003 and 0.749 ± 0.012 for the simulation and experiment respectively. Interstrip efficiency is the probability of a hit being recorded given a reconstructed track, interstrip clustering is the probability of a cluster having a size greater than one; both as a function of the position of a track within a strip. The bottom plot in both figures shows the ratio of experiment (Exp) to simulation (Sim).

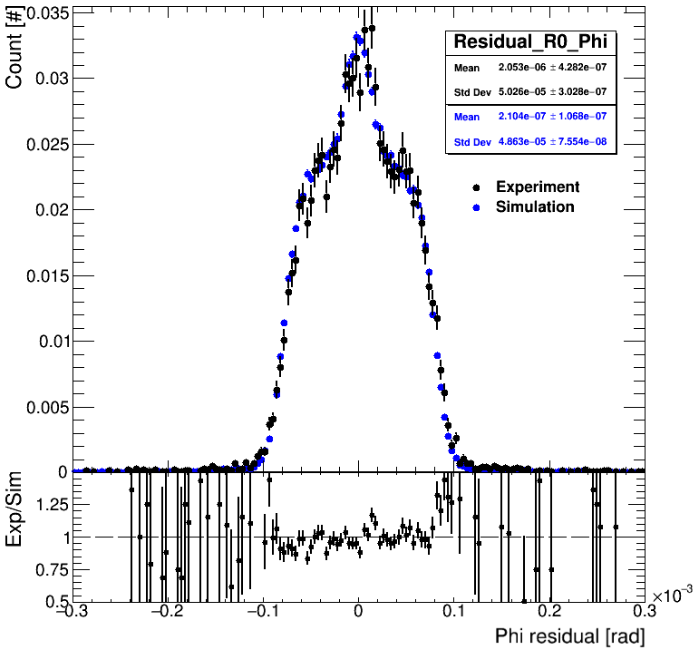

FIGURE 6.26: The phi residual (track - hit) for the R0 corresponding at 0.9 fC threshold and angular pitch of 171.8368 mrad. The secondary peak is due to clusters of size greater than one. They are both normalised to one. The bottom plot shows the ratio of experiment (Exp) to simulation (Sim).

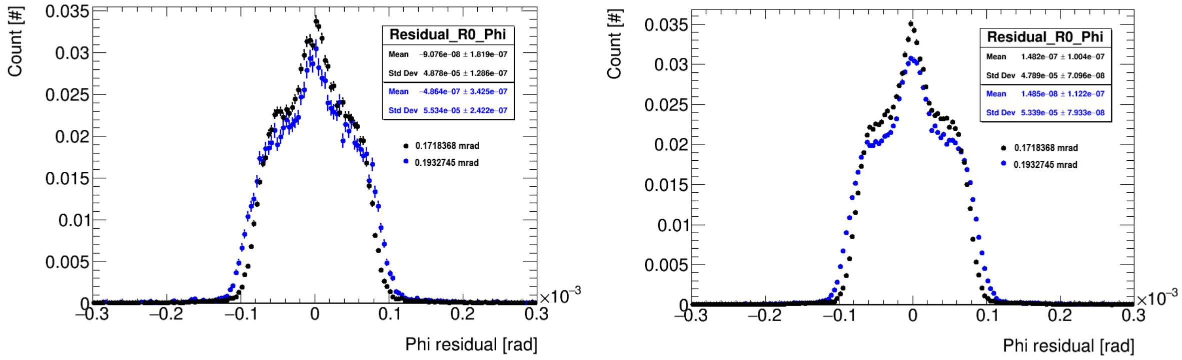

(a) (b)

FIGURE 6.27: Plots of the phi residuals (track - hit) for two different positions, namely in row 4 and row 1, for experiment (a) and simulation (b). Row 1 has a pitch of 193.3 μrad while row 4 has a pitch of 171.8 μrad. All have been normalised to one and all are at 0.75 fC.

6.2.4 True and Reconstructed Monte Carlo

Only one position and threshold will be used for the comparison of the Monte Carlo (MC) information and the reconstruction of that simulation, namely the high detailed run position and threshold corresponding to the simulation in Figs. 6.7 - 6.10. The first comparison, shown in Fig. 6.28(a), is the phi residual of the MC truth track and the position of the strip that that track passed through. The MC truth track is the actual path of the particle through the telescope in the simulation. The residual peak has sharp edges with no residuals outside this peak as well as a uniform top, proving that the tracks are spread out evenly within the strips. The edges correspond to an angle of ~ 0.000086 rad, which is half the angular pitch (0.0001718368 rad) in this row of strips, as expected. For clusters of size 1, the position will be the same as the position of the strip the track passed through. However, for clusters of size greater than one, the position of the cluster will be the mean centre of the positions of the strips in that cluster. The residuals for clusters of size 2 are smaller as sharing only occurs in a small area near the border of a strip, so the track is closer to the centre of the cluster in this case. This is illustrated in Fig. 6.28(b), which shows the residuals for the truth tracks and the reconstructed tracks against the cluster positions. The width of the truth track residual is thinner compared to Fig. 6.28(a) as the residuals of the tracks at the edge of the strip are now in the secondary peak for the clusters of size 2. The residuals outside this main peak are due to badly reconstructed tracks. Comparing the reconstructed track residual to the truth track residual, it can be seen that the reconstruction smears out the actual position of the tracks. This is better illustrated in the residual plot of the truth tracks against the reconstructed tracks in Fig. 6.29(a). The final comparison is that of the interstrip clustering for the for truth tracks vs the reconstructed tracks in Fig. 6.29(b). The MC clustering has very sharp peaks at the edges, which is expected as sharing is only done when the track is within a certain distance of the edge of the strip and mono-energetic beams were used. The peak starts at a pitch fraction

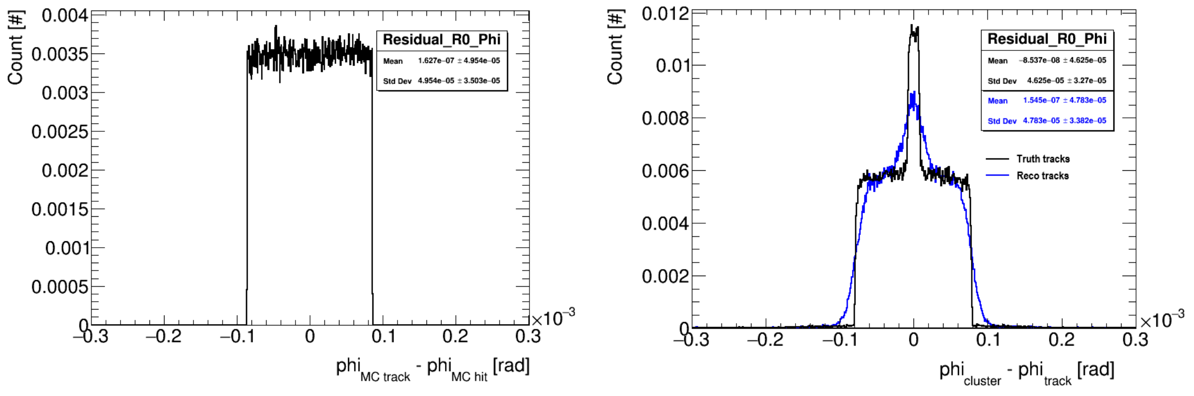

(a) (b)

FIGURE 6.28: The phi residuals of the Monte Carlo truth tracks against the position of the strip those tracks passed through (a) and the phi residuals for the truth and reconstructed tracks against the cluster positions (b). The secondary peaks in (b) are due to clusters of size 2. All are normalised to one and correspond to the high-detailed run in row 4 at a threshold of 0.75 fC.

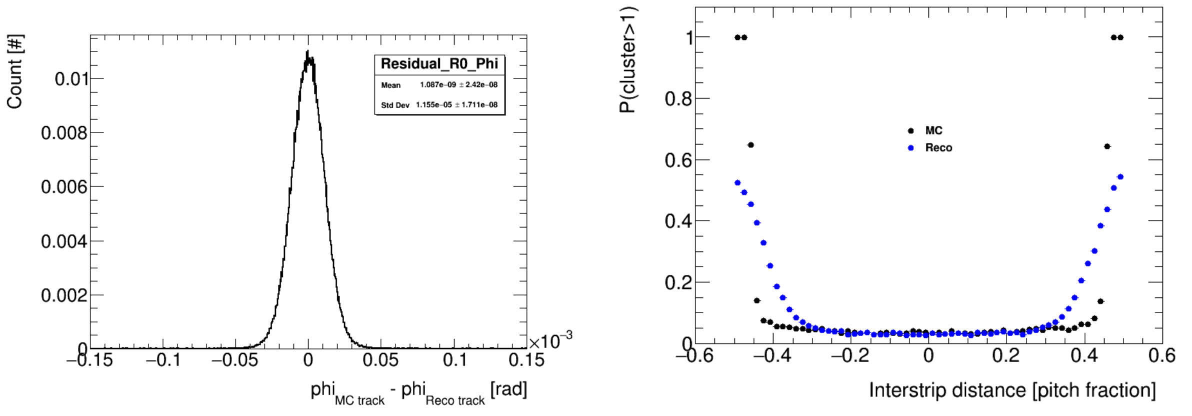

(a) (b)

FIGURE 6.29: The phi residual of the Monte Carlo truth tracks against the reconstructed tracks, normalised to 1 (a) and the interstrip clustering of the truth tracks and the reconstructed tracks (b). They correspond to the position in row 4 at a threshold of 0.75 fC. Interstrip clustering shows the probability of a cluster having a size greater than one as a function of the position of a track within a strip.

of around ±0.45, which corresponds to an angular distance from the edge of around 8.6 μrad. This distance also happens to be half the width of the secondary peak of the truth track residual in Fig. 6.28(b), as expected. The reconstructed clustering has lower, smeared out peaks which are most likely due to the smearing out of the position of the tracks.

Chapter 7

Conclusion

CERN is planning to upgrade the LHC to the High Luminosity LHC by the year 2026. In preparation for this, the ATLAS detector will also require upgrades in order to cope with the higher pileup and radiation environment. One of the main upgrades will be the complete overhaul of the current Inner Detector with the all new silicon Inner Tracker during the ATLAS Phase-II upgrades scheduled for 2024 to 2026. An important part of the upgrade is the Research and Development (R&D) phase for the new sensors. This thesis focussed on the R&D of one of the modules in the forward region of the ITk's strip detector, the R0 module. The R0 module required a full radial description in the simulation framework of AllPix as well as a radial geometrical description in the reconstruction framework of EUTelescope. This was the first time a radial sensor had been used in both these testbeam software packages.

The testing of the R0 module, as well as the ITk strip barrel short strip module occurred in May 2017 at DESY, Hamburg. Testing was done on how well the sensor records a particle traversing it, how the charge is shared and how efficient the sensor is. Despite some of the chips not being powered and some having increased noise, almost all the planned points on the sensor to be tested were tested. There was time for extra measurements to be taken as well, resulting in more data than expected. Radiation length testing was also performed on both the modules to determine whether the final product had the expected radiation thickness as outlined in the technical design reports.

The description of the R0 sensor in AllPix, based in the Geant4 framework, as well as the digitiser for the R0 sensor in AllPix have been completed. Basic tests have shown that the calculation of which strip was hit is accurate and that charge is conserved when calculating the charge sharing between neighbouring strips. On the EUTelescope side, an implementation using ROOT's TGeo of the R0 sensor geometry has been completed and was used by the ITk strips testbeam group to make the necessary changes to the EUTelescope reconstruction chain. A comparison of the simulated testbeam telescope to the actual testbeam telescope was performed.

The simulated data matches well with the experimental data, which in turn performs as was expected for the R0 module based on previous tests done on other strip sensors. This indicates that the radial geometry definitions in EUTelescope provides very good reconstruction of radial data. The simulation of the R0 sensor in terms of both the geometry and the charge propagation works well, and excluding disabled and noisy chips, the simulation predicts reasonably well how the R0 module behaves in the testbeam telescope.

The phi residuals of both simulation and experiment for the different rows of strips match with expectation, giving standard deviations very close to the resolutions of $\sim 4.9 \times 10^{-5}$ rad in the outer rows and $\sim 5.5 \times 10^{-5}$ rad in the inner rows, based on that resolution $\sim$ pitch/$\sqrt{12}$. The residuals also show the double peak structure from clusters composed of two strips at lower thresholds, and that this peak reduces as the threshold is increased. The interstrip clustering for both simulation and experiment have constant sharing in the central region of the strips and peaks at the edges for the lower thresholds as expected. The peaks reduce as the threshold is increased and the overall shape starts to flatten. The interstrip efficiencies for low thresholds are roughly constant around 1, matching with previous sensor tests. The efficiencies start to drop at the edges as the threshold increases due to the reduction in sharing. Unfortunately the total amount of sharing in the simulation doesn't match perfectly with the experiment. This may be due to the simplifications used in the digitiser, in particular the one dimensional electric field, no modeling of electronic noise or random gaussian spreads in the threshold and beam energy. The temperature and voltages may have fluctuated enough during the experiment to cause non-negligible effects that aren't modeled in the simulation as well. The conversion from the threshold used in the experiment, which is in units of DACs, to the threshold used in the simulation, in units of femtocoulomb, will have introduced uncertainties that weren't taken into account in this study.

Work that can be done in future to improve these results will be to improve the digitiser by adding statistical fluctuations to the threshold and due to electronic noise, using more accurate electric field definitions from TCAD models of the sensor and modeling both electron and hole transport. More accurate threshold conversions would also reduce the uncertainties in the actual threshold used.

Appendix A

Simulation and Reconstruction Code

A.1 AllPix Macro File

This is the macro file used in AllPix where the user defines the positions and orientations of the detectors, as well as the particles used. It is the interface between the user and the AllPix software.

```
# Test sensors
/control/alias appPosZ -4.750
/control/alias enhanceZ 5.0

# DUT and timing detector
/allpix/det/setId        410
/allpix/det/setPosition  -21.5 -33.3 384.0 mm
/allpix/det/setRotation  0.0 180.0 0.0 deg
/allpix/det/setLowTHL 13. keV
/allpix/det/setId        200
/allpix/det/setPosition  0.0 0.0 744.0 mm
/allpix/det/setRotation  0.0 180.0 90.0 deg
/allpix/det/setLowTHL 13. keV
# EUDET Planes (Mimosa26)
/allpix/det/setId        300
/allpix/det/setPosition  0.0 0.0 0.0 mm
/allpix/det/setRotation  0.0 180.0 180.0 deg
/allpix/det/setLowTHL    13. keV
/allpix/det/setId        301
/allpix/det/setPosition  0.0 0.0 149.0 mm
/allpix/det/setRotation  0.0 180.0 180.0 deg
/allpix/det/setLowTHL    13. keV
```

```
/allpix/det/setId        302
/allpix/det/setPosition  0.0 0.0 299.0 mm
/allpix/det/setRotation  0.0 180.0 180.0 deg
/allpix/det/setLowTHL    13. keV
/allpix/det/setId        303
/allpix/det/setPosition  0.0 0.0 484.0 mm
/allpix/det/setRotation  0.0 180.0 180.0 deg
/allpix/det/setLowTHL    13. keV
/allpix/det/setId        304
/allpix/det/setPosition  0.0 0.0 635.0 mm
/allpix/det/setRotation  0.0 180.0 180.0 deg
/allpix/det/setLowTHL    13. keV
/allpix/det/setId        305
/allpix/det/setPosition  0.0 0.0 787.0 mm
/allpix/det/setRotation  0.0 180.0 180.0 deg
/allpix/det/setLowTHL    13. keV

# Build detectors
/allpix/phys/Physics emstandard_opt0
/run/initialize
/allpix/det/update
# Write Telescope files
/allpix/timepixtelescope/setFolderPath ./EUTelescopeFiles/Run_900011
/allpix/timepixtelescope/setEventIDcolumn 0
/allpix/timepixtelescope/setSumTOT 1
/allpix/timepixtelescope/write 1

# Source GPS
/gps/particle e-
/gps/pos/type Plane
/gps/pos/shape Rectangle
/gps/pos/centre 0.0 0.0 -1000.0 mm
/gps/pos/halfy 5. mm
/gps/pos/halfx 8. mm
/gps/direction 0 0 1
/gps/energy 4.4 GeV
# Shoot
/allpix/beam/frames 250000
/allpix/beam/type const 1
/allpix/beam/on
```

A.2 AllPix Construction File

This is the AllpixDetectorConstruction.cc file in which the detectors are set up. Only the sections relevant to the R0 sensor are shown.

```
//create the four different strip lengths
G4Tubs* Row1Strip= new G4Tubs(SliceName.first, r0, r1, geoMap[*detItr]->GetHalfSensorZ
    (), -geoMap[*detItr]->GetPixelPhi()/2, geoMap[*detItr]->GetPixelPhi());
G4Tubs* Row2Strip= new G4Tubs(SliceName.first, r1, r2, geoMap[*detItr]->GetHalfSensorZ
    (), -geoMap[*detItr]->GetPixelPhi()/2, geoMap[*detItr]->GetPixelPhi());
G4Tubs* Row3Strip= new G4Tubs(SliceName.first, r2, r3, geoMap[*detItr]->GetHalfSensorZ
    (), -geoMap[*detItr]->GetPixelPhi2()/2, geoMap[*detItr]->GetPixelPhi2());
G4Tubs* Row4Strip= new G4Tubs(SliceName.first, r3, r4, geoMap[*detItr]->GetHalfSensorZ
    (), -geoMap[*detItr]->GetPixelPhi2()/2, geoMap[*detItr]->GetPixelPhi2());

//Create the sensor geometry through the intersection of two solids
G4RotationMatrix*  Rotate = new G4RotationMatrix;
G4ThreeVector Trans(FocusX, FocusY, 0.0);
G4Tubs* circle= new G4Tubs("circle", r0, r4, geoMap[*detItr]->GetHalfSensorZ(),0,pi);
G4Tubs* slice = new G4Tubs("slice", 0, r4*1.1, geoMap[*detItr]->GetHalfSensorZ(),
    geoMap[*detItr]->GetSensorSPhi(), geoMap[*detItr]->GetSensorDPhi());
G4VSolid* Sensor_box = new G4IntersectionSolid(BoxName.second, circle, slice, Rotate,
    Trans);

//create guard ring through intersection
G4double moveR = geoMap[*detItr]->GetSensorExcessHRight()/sin(geoMap[*detItr]->
    GetSensorDPhi()/2);
G4Tubs* circle2 = new G4Tubs("circle2", r0-geoMap[*detItr]->GetSensorExcessHBottom(),
    r4+geoMap[*detItr]->GetSensorExcessHTop(), geoMap[*detItr]->GetHalfSensorZ(), 0,
    pi);
G4Tubs* slice2 = new G4Tubs("slice2", 0, (r4+moveR)*1.1, geoMap[*detItr]->
    GetHalfSensorZ(),geoMap[*detItr]->GetSensorSPhi(),geoMap[*detItr]->GetSensorDPhi()
    );
//move the slice so that there will be excess on the straight sides
G4double moveX = moveR*cos(midPhi);
G4double moveY = moveR*sin(midPhi);
G4ThreeVector Trans2(Trans.x()-moveX,Trans.y()-moveY,0);

G4VSolid* Solid_GuardRings_Ext = new G4IntersectionSolid(BoxName.second, circle2,
    slice2, Rotate, Trans2);
G4VSolid * Solid_GuardRings =  new G4SubtractionSolid(GuardRingsName.second,
    Solid_GuardRings_Ext, Sensor_box);
```

```
G4double sensorOffsetX = geoMap[*detItr]->GetSensorXOffset();
G4double sensorOffsetY = geoMap[*detItr]->GetSensorYOffset()-geoMap[*detItr]->
    GetSensorR();

m_Sensor_log[(*detItr)] = new G4LogicalVolume(Sensor_box, Silicon, BoxName.second+"
    _log");

posSensor.setX(sensorOffsetX); posSensor.setY(sensorOffsetY);
posSensor.setZ(posDevice.z());

m_Sensor_phys[(*detItr)] = new G4PVPlacement(0, posSensor, m_Sensor_log[(*detItr)],
    BoxName.second+"_phys", m_wrapper_log[(*detItr)], // mother log
false, (*detItr), // copy number
true); // check overlap

//CREATION OF THE STRIPS
m_Row1Strip_log[(*detItr)]= new G4LogicalVolume(Row1Strip, Silicon, PixelName.second);
m_Row2Strip_log[(*detItr)]= new G4LogicalVolume(Row2Strip, Silicon, PixelName.second);
m_Row3Strip_log[(*detItr)]= new G4LogicalVolume(Row3Strip, Silicon, PixelName.second);
m_Row4Strip_log[(*detItr)]= new G4LogicalVolume(Row4Strip, Silicon, PixelName.second);

G4AssemblyVolume* assemblyDetector1 = new G4AssemblyVolume();
G4AssemblyVolume* assemblyDetector2 = new G4AssemblyVolume();
G4RotationMatrix Rot;
G4ThreeVector Pos, Tm;
G4Transform3D transform;

Pos.setX(-r0);
transform = G4Transform3D(Rot,Pos);
assemblyDetector1->AddPlacedVolume( m_Row1Strip_log[(*detItr)], transform );
assemblyDetector1->AddPlacedVolume( m_Row2Strip_log[(*detItr)], transform );
Pos.setX(-r2);
transform = G4Transform3D(Rot,Pos);
assemblyDetector2->AddPlacedVolume( m_Row3Strip_log[(*detItr)], transform );
assemblyDetector2->AddPlacedVolume( m_Row4Strip_log[(*detItr)], transform );

//get angle of the last strip for the first two rows
theta=pi/2+geoMap[*detItr]->GetStereoAngle()+(geoMap[*detItr]->GetNPixelsPhi()/2-0.5)*
    geoMap[*detItr]->GetPixelPhi();

for( int i = geoMap[*detItr]->GetNPixelsPhi()-1; i >=0; i-- ){
  //get each position of the strips
  phi_i=(i-geoMap[*detItr]->GetNPixelsPhi()/2+0.5)*geoMap[*detItr]->GetPixelPhi();
```

```
  b=-2*(2*geoMap[*detItr]->GetSensorR()*sin(geoMap[*detItr]->GetStereoAngle()/2))*sin(
    geoMap[*detItr]->GetStereoAngle()/2+phi_i);
  c=pow((2*geoMap[*detItr]->GetSensorR()*sin(geoMap[*detItr]->GetStereoAngle()/2)),2)-
    pow((r0),2);
  r=0.5*(-b+sqrt(pow(b,2)-4*c));
  y=r*cos(phi_i+geoMap[*detItr]->GetStereoAngle()) - geoMap[*detItr]->GetSensorR()*cos
    (geoMap[*detItr]->GetStereoAngle());
  x=-r*sin(phi_i+geoMap[*detItr]->GetStereoAngle()) + geoMap[*detItr]->GetSensorR()*
    sin(geoMap[*detItr]->GetStereoAngle());

  Tm.setX(x);
  Tm.setY(y+geoMap[*detItr]->GetSensorR());
  G4RotationMatrix Rm; Rm.rotateZ(theta);
  transform=G4Transform3D(Rm,Tm);
  assemblyDetector1->MakeImprint(m_Sensor_log[(*detItr)],transform);
  theta-=geoMap[*detItr]->GetPixelPhi();
}

//get angle of the first strip for last two rows
theta=pi/2+geoMap[*detItr]->GetStereoAngle()+(-geoMap[*detItr]->GetNPixelsPhi2()
    /2+0.5)*geoMap[*detItr]->GetPixelPhi2();

for( int i = 0; i <geoMap[*detItr]->GetNPixelsPhi2(); i++ ){
        //get each position of the strips
    phi_i=(i-geoMap[*detItr]->GetNPixelsPhi2()/2+0.5)*geoMap[*detItr]->GetPixelPhi2();
    b=-2*(2*geoMap[*detItr]->GetSensorR()*sin(geoMap[*detItr]->GetStereoAngle()/2))*
    sin(geoMap[*detItr]->GetStereoAngle()/2+phi_i);
    c=pow((2*geoMap[*detItr]->GetSensorR()*sin(geoMap[*detItr]->GetStereoAngle()/2))
    ,2)-pow(r2,2);
    r=0.5*(-b+sqrt(pow(b,2)-4*c));
    y=r*cos(phi_i+geoMap[*detItr]->GetStereoAngle()) - geoMap[*detItr]->GetSensorR()*
    cos(geoMap[*detItr]->GetStereoAngle());
    x=-r*sin(phi_i+geoMap[*detItr]->GetStereoAngle()) + geoMap[*detItr]->GetSensorR()*
    sin(geoMap[*detItr]->GetStereoAngle());

    Tm.setX(x);
    Tm.setY(y+geoMap[*detItr]->GetSensorR());
        G4RotationMatrix Rm; Rm.rotateZ(theta);
    transform=G4Transform3D(Rm,Tm);
    assemblyDetector2->MakeImprint(m_Sensor_log[(*detItr)],transform);
    theta+=geoMap[*detItr]->GetPixelPhi2();
}
```

A.3 AllPix Digitiser

Sharing would be tested for the strips above, next to and below the registered strip, however only sharing to the strips above (across the boundary between rows 2 and 3) have been shown. This is just to illustrate how sharing is calculated across the complex boundary where the strip angular pitch and number of strips changes, in this case row 2 sharing into row 3.

```
double SensorMidR=m_gD->GetSensorRmin()+m_gD->GetStripLength1()+m_gD->GetStripLength2
    ();
//Radial distance of hit from origin of sensor was at (0,R)
//Pos.x() and Pos.y() are the particle's positions in the local reference frame
G4double radi=sqrt(pow(Pos.x(),2)+pow(Pos.y()+m_SensorR,2));
//Angle and radial distance of hit w.r.t focus point if sensor was at (0,R)
double PhiHit=atan2(PosY+m_SensorR-m_FocusY, PosX-m_FocusX);
double RHit=sqrt(pow(PosX-m_FocusX,2)+pow(PosY+m_SensorR-m_FocusY,2));
if (radi>=m_gD->GetSensorRmin() and radi<SensorMidR-m_gD->GetStripLength2()){
  RowIndex=0;
  StripRcentre=m_gD->GetSensorRmin()+m_gD->GetStripLength1()/2;
  thetaStart=Pitch*(NStrips/2)+m_gD->GetStereoAngle()+PI/2;
}
else if (radi>=m_gD->GetSensorRmin()+m_gD->GetStripLength1() and radi<SensorMidR){
  RowIndex=1;
  StripRcentre=SensorMidR-m_gD->GetStripLength2()/2;
  thetaStart=Pitch*(NStrips/2)+m_gD->GetStereoAngle()+PI/2;
}
else if (radi>=SensorMidR and radi<SensorMidR+m_gD->GetStripLength3()){
  RowIndex=2;
  StripRcentre=SensorMidR+m_gD->GetStripLength3()/2;
  thetaStart=Pitch*(-NStrips/2)+m_gD->GetStereoAngle()+PI/2;
}
else if (radi>=SensorMidR+m_gD->GetStripLength3() and radi<m_gD->GetSensorRmax()){
  RowIndex=3;
  StripRcentre=m_gD->GetSensorRmax()-m_gD->GetStripLength4()/2;
  thetaStart=Pitch*(-NStrips/2)+m_gD->GetStereoAngle()+PI/2;
}
StripIndex=Floor(abs(thetaStart-PhiHit)/Pitch);

//Assign the indices to the strip that the particle passed through
currentStrip.first = StripIndex;
currentStrip.second = RowIndex;
//difference in R of hit and radial centre of strip
DHitR=radi-StripRcentre;
```

```
//angle distance between particle and centre of strip
double dPhi=(NStrip/2-currentStrip.first-0.5)*StripPitch+m_stereo+PI/2-PhiHit;

double diffusionWidth = sqrt(2.*m_diffusion[Electron]*tDrift);
//test for charge sharing
if ( StripL/2-abs(DHitR) < 3*diffusionWidth || RHit*(StripPitch/2-abs(dPhi)) < 3*
    diffusionWidth ) {
  // Main strip
  double stripEnergy = IntegrateGaussian(RHit*dPhi/um, DHitR/um, diffusionWidth/um,(-
    RHit*StripPitch/2)/um, (RHit*StripPitch/2)/um, (-StripL/2)/um, (StripL/2)/um, eHit
    );
  //prevent the outside field shaping strips from acting as readout channels
  if(currentStrip.first==0 || currentStrip.first==NStrip-1){stripEnergy=0.0;}
  stripContent[currentStrip] += stripEnergy;

  //get angle of current strips left side
  phia=m_thetaStart1-StripPitch*(currentStrip.first);
  //find index of strip above and to the left
  Nx=floor(abs(m_thetaStart2-phia)/m_pitchPhi2);
  // get indeces of neighbouring strips to this strip
  Nx_1=Nx+1; Nx1=Nx-1; Nx2=Nx-2;
  //find the angle of the left side of these strips
  phi=m_thetaStart2+m_pitchPhi2*(Nx+1);
  phi1=m_thetaStart2+m_pitchPhi2*(Nx1+1);
  phi2=m_thetaStart2+m_pitchPhi2*(Nx2+1);

  //determine which strips will get a charge share
  extraStrip.second = currentStrip.second + 1;
  extraStrip.first =Nx_1;
  if(extraStrip.first >= 1 && extraStrip.second>=0 && extraStrip.first < m_nStrips2-1
    && extraStrip.second < m_nRows){
    double sharedEnergy = IntegrateGaussian(RHit*dPhi/um, DHitR/um, diffusionWidth/um,
     (-HitR*(StripPitch/2+phi+m_pitchPhi2-phia))/um, (-HitR*(StripPitch/2+phi-phia))/
    um, (StripL/2)/um, (StripL/2+m_geometry->GetStripLength3())/um, eHit);
        stripContent[extraStrip] += sharedEnergy;
  }

  extraStrip.second = currentStrip.second + 1;
  extraStrip.first =Nx;
  if(extraStrip.first >= 1 && extraStrip.second>=0 && extraStrip.first < m_nStrips2-1
    && extraStrip.second < m_nRows){
    double sharedEnergy = IntegrateGaussian(RHit*dPhi/um, DHitR/um, diffusionWidth/um,
     (-HitR*(StripPitch/2+phi-phia))/um, (-HitR*(StripPitch/2+phi1-phia))/um, (StripL
    /2)/um, (StripL/2+m_geometry->GetStripLength3())/um, eHit);
```

```
    stripContent[extraStrip] += sharedEnergy;
  }

  extraStrip.second = currentStrip.second + 1;
  extraStrip.first =Nx1;
  if(extraStrip.first >= 1 && extraStrip.second>=0 && extraStrip.first < m_nStrips2-1
    && extraStrip.second < m_nRows){
    double sharedEnergy = IntegrateGaussian(RHit*dPhi/um, DHitR/um, diffusionWidth/um,
     (-HitR*(StripPitch/2+phi1-phia))/um, (-HitR*(StripPitch/2+phi2-phia))/um, (StripL
    /2)/um, (StripL/2+m_geometry->GetStripLength3())/um, eHit);
    stripContent[extraStrip] += sharedEnergy;
  }

  extraStrip.second = currentStrip.second + 1;
  extraStrip.first =Nx2;
  if(extraStrip.first >= 1 && extraStrip.second>=0 && extraStrip.first < m_nStrips2-1
    && extraStrip.second < m_nRows){
    double sharedEnergy = IntegrateGaussian(RHit*dPhi/um, DHitR/um, diffusionWidth/um,
     (-HitR*(StripPitch/2+phi2-phia))/um, (-HitR*(StripPitch/2+phi2-phia-m_pitchPhi2))
    /um, (StripL/2)/um, (StripL/2+m_geometry->GetStripLength3())/um, eHit);
    stripContent[extraStrip] += sharedEnergy;
  }
}
//Check to see if over threshold
map<pair<G4int, G4int>, G4double >::iterator iCount = stripContent.begin();
for( ; iCount != stripContent.end() ; iCount++){
  double stripEnergy = (*iCount).second;
  double depositedCharge = stripEnergy/kPairEnergy/fC;
  bool crossed = false;
  for (int timeSlice=m_minTime; timeSlice<m_maxTime; timeSlice++) {
    double Y = 0;
    double t = timeSlice/(7.0*ns);
    if(t>0){Y = depositedCharge / 27.0 * exp(3-t) * t*t*t;}
    if(crossed == false and Y >= getThresholdCharge() and timeSlice < 25){crossed =
    true;}
  }
}
```

Appendix B

EUTelescope Code

B.1 EUTelescope TGeo File

This is the TGeo definition for the R0 sensor used in the radial version of EUTelescope.

```
AnnulusStripGeoDescr::AnnulusStripGeoDescr( int xPixel, int yPixel, double xSize,
    double ySize, double zSize, double pitchPhi, double stereoAngle, double rmin,
    double rmax, double rCentre, double radLength): EUTelGenericPixGeoDescr( xSize,
    ySize, zSize, 0, xPixel-1, 0, yPixel-1, radLength) {
  Double_t PI=3.14159265358979,deg=180/PI;
  Double_t phi_i,b,r,c,x,y,gradient,theta;
  matSi = new TGeoMaterial( "Si", 28.0855 , 14.0, 2.33, -_radLength, 45.753206 );
  Si = new TGeoMedium("MimosaSilicon",1, matSi);

  plane = _tGeoManager->MakeBox("sensarea_box",Si,150,500,1);
  rowstrip = _tGeoManager->MakeTubs( "sensarea_strip" , Si, rmin, rmax, zSize/2, 90+(-
    pitchPhi/2)*deg,90+(pitchPhi/2)*deg);
  theta=pitchPhi*((xPixel-1)/2.0)+stereoAngle+PI/2;
  if(xPixel>1090){//placement of outer two rows
    for( int i = xPixel-1; i >=0; i-- ){
      TGeoCombiTrans* trans=new TGeoCombiTrans(0,0,0,new TGeoRotation("rot",0,0,0));
      //get position
      phi_i=(i -(xPixel-1)/2.0)*pitchPhi;
      b=-2*(2*rCentre*sin(stereoAngle/2))*sin(stereoAngle/2+phi_i);
      c=pow((2*rCentre*sin(stereoAngle/2)),2)-pow(rmin,2);
      r=0.5*(-b+sqrt(pow(b,2)-4*c));
      y=r*cos(phi_i+stereoAngle) - rCentre*cos(stereoAngle);
      x=-r*sin(phi_i+stereoAngle) + rCentre*sin(stereoAngle);
      //rotate to get correct angle of strip
```

```
      trans->RotateZ(theta*deg-90);
      trans->SetTranslation(x-rmin*cos(theta),y-rmin*sin(theta),0);
      //add the nodes
      plane->AddNode(rowstrip,i+1,trans);
      //get angle of next strip
      theta-=pitchPhi;
    }
  }
  else{//placement of inner two rows
    for( int i = 0; i <=xPixel-1; i++ ){
      TGeoCombiTrans* trans=new TGeoCombiTrans(0,0,0,new TGeoRotation("rot",0,0,0));
      //get position
      phi_i=((xPixel -1 - i) - (xPixel-1)/2.0)*pitchPhi;
      b=-2*(2*rCentre*sin(stereoAngle/2))*sin(stereoAngle/2+phi_i);
      c=pow((2*rCentre*sin(stereoAngle/2)),2)-pow(rmin,2);
      r=0.5*(-b+sqrt(pow(b,2)-4*c));
      y=r*cos(phi_i+stereoAngle) - rCentre*cos(stereoAngle);
      x=-r*sin(phi_i+stereoAngle) + rCentre*sin(stereoAngle);
      //rotate to get correct angle of strip
      trans->RotateZ(theta*deg-90);
      trans->SetTranslation(x-rmin*cos(theta),y-rmin*sin(theta),0);
      //add the nodes
      plane->AddNode(rowstrip,i+1,trans);
      //get angle of next strip
      theta-=pitchPhi;
    }
  }
}
void  AnnulusStripGeoDescr::createRootDescr(char const * planeVolume){
  //Get the plane as provided by the EUTelGeometryTelescopeGeoDescription
  TGeoVolume* topplane =_tGeoManager->GetVolume(planeVolume);
  //Add the sensitive area to the plane
  topplane->AddNode(plane, 1,new TGeoTranslation(0,0,0) );
}
std::string AnnulusStripGeoDescr::getPixName(int x , int y){
  char buffer [100];
  if(x<512){snprintf( buffer, 100, "/sensarea_box_1/sensarea_strip_%d", x+1);}
  else if(x>=512 && x<=_maxIndexX+256){//256 is for the offset testbeam channels
    snprintf( buffer, 100, "/sensarea_box_1/sensarea_strip_%d", x+1-256);}
  else{snprintf( buffer, 100, "invalid index");}
  return std::string( buffer );//return path to the strip
}
```

B.2 GEAR File

This is the GEAR file used in the EUTelescope software wherein the detectors used .

```
<gear>
  <global detectorName="EUTelescope" />
  <BField type="ConstantBField" x="0.0" y="0.0" z="0.0" />
  <detectors>
    <detector name="SiPlanes" geartype="SiPlanesParameters">
      <siplanesID ID="0" />
      <siplanesType type="TelescopeWithDUT" />
      <siplanesNumber number="8" />
      <layers>
        <layer>
          <ladder ID="0"
           positionX="0.0" positionY="0.0" positionZ="0.0"
           rotationXY="180" rotationZX="180" rotationZY="0.0"
           sizeX="21.1968" sizeY="10.5984" thickness="0.05"
           radLength="93.66073400" />
          <sensitive ID="0"
           positionX="0.0" positionY="0.0" positionZ="0.0"
           sizeX="21.1968" sizeY="10.5984" thickness="0.05"
           npixelX="1152" npixelY="576" pitchX="0.0184" pitchY="0.0184"
           resolution="0.0045" radLength="93.66073400"
           rotation1="1.0" rotation2="0.0" rotation3="0.0" rotation4="1.0"/>
        </layer>
        <layer>
          <ladder ID="1"
           positionX="0.0" positionY="0.0" positionZ="149"
           rotationXY="180" rotationZX="180" rotationZY="0.0"
           sizeX="21.1968" sizeY="10.5984" thickness="0.05"
           radLength="93.66073400" />
          <sensitive ID="1"
           positionX="0.0" positionY="0.0" positionZ="149"
           sizeX="21.1968" sizeY="10.5984" thickness="0.05"
           npixelX="1152" npixelY="576" pitchX="0.0184" pitchY="0.0184"
           resolution="0.0045" radLength="93.66073400"
           rotation1="1.0" rotation2="0.0" rotation3="0.0" rotation4="1.0"/>
        </layer>
        <layer>
          <ladder ID="2"
           positionX="0.0" positionY="0.0" positionZ="299"
           rotationXY="180" rotationZX="180" rotationZY="0.0"
```

```
   sizeX="21.1968" sizeY="10.5984" thickness="0.05"
   radLength="93.66073400" />
  <sensitive ID="2"
   positionX="0.0" positionY="0.0" positionZ="299"
   sizeX="21.1968" sizeY="10.5984" thickness="0.05"
   npixelX="1152" npixelY="576" pitchX="0.0184" pitchY="0.0184"
   resolution="0.0045" radLength="93.66073400"
   rotation1="1.0" rotation2="0.0" rotation3="0.0" rotation4="1.0"/>
</layer>
<layer>
  <ladder ID="17"
   positionX="0.0" positionY="0.0" positionZ="384"
   rotationXY="0.0" rotationZX="180" rotationZY="0.0"
   sizeX="100" sizeY="120" thickness="0.3"
   radLength="93.66073400" />
  <sensitive ID="17"
   positionX="0.0" positionY="0.0" positionZ="384"
   sizeX="100" sizeY="120" thickness="0.3"
   npixelX="1154" npixelY="2" pitchX="0.0745" pitchY="50"
   resolution="0.0045" radLength="93.66073400"
   resolutionX="4.96050113683419472e-05" resolutionY="10000000"
   rotation1="1.0" rotation2="0.0" rotation3="0.0" rotation4="1.0"/>
</layer>
<layer>
  <ladder ID="3"
   positionX="0.0" positionY="0.0" positionZ="484"
   rotationXY="180" rotationZX="180" rotationZY="0.0"
   sizeX="21.1968" sizeY="10.5984" thickness="0.05"
   radLength="93.66073400" />
  <sensitive ID="3"
   positionX="0.0" positionY="0.0" positionZ="484"
   sizeX="21.1968" sizeY="10.5984" thickness="0.05"
   npixelX="1152" npixelY="576" pitchX="0.0184" pitchY="0.0184"
   resolution="0.0045" radLength="93.66073400"
   rotation1="1.0" rotation2="0.0" rotation3="0.0" rotation4="1.0"/>
</layer>
<layer>
  <ladder ID="4"
   positionX="0.0" positionY="0.0" positionZ="635"
   rotationXY="180" rotationZX="180" rotationZY="0.0"
   sizeX="21.1968" sizeY="10.5984" thickness="0.05"
   radLength="93.66073400" />
  <sensitive ID="4"
   positionX="0.0" positionY="0.0" positionZ="635"
```

```
           sizeX="21.1968" sizeY="10.5984" thickness="0.05"
           npixelX="1152" npixelY="576" pitchX="0.0184" pitchY="0.0184"
           resolution="0.0045" radLength="93.66073400"
           rotation1="1.0" rotation2="0.0" rotation3="0.0" rotation4="1.0"/>
        </layer>
        <layer>
          <ladder ID="7"
           positionX="0.0" positionY="0.0" positionZ="744"
           rotationXY="270" rotationZX="180" rotationZY="0.0"
           sizeX="20" sizeY="16.8" thickness="0.3"
           radLength="93.66073400" />
          <sensitive ID="7"
           positionX="0.0" positionY="0.0" positionZ="744"
           sizeX="20" sizeY="16.8" thickness="0.3"
           npixelX="80" npixelY="336" pitchX="0.25" pitchY="0.05"
           resolution="0.1" radLength="93.66073400"
           resolutionX="0.072" resolutionY="0.0144"
           rotation1="1.0" rotation2="0.0" rotation3="0.0" rotation4="1.0"/>
        </layer>
        <layer>
          <ladder ID="5"
           positionX="0.0" positionY="0.0" positionZ="787"
           rotationXY="180" rotationZX="180" rotationZY="0.0"
           sizeX="21.1968" sizeY="10.5984" thickness="0.05"
           radLength="93.66073400" />
          <sensitive ID="5"
           positionX="0.0" positionY="0.0" positionZ="787"
           sizeX="21.1968" sizeY="10.5984" thickness="0.05"
           npixelX="1152" npixelY="576" pitchX="0.0184" pitchY="0.0184"
           resolution="0.0045" radLength="93.66073400"
           rotation1="1.0" rotation2="0.0" rotation3="0.0" rotation4="1.0"/>
        </layer>
      </layers>
    </detector>
  </detectors>
</gear>
```

Bibliography

[1] Stephen T. Thornton and Andrew Rex. *Modern Physics for Scientists and Engineers.* Brooks/Cole, Boston, Massachusetts, USA, 4 edition, 2013. ISBN 978-1-133-10372-1.

[2] J. J. Thomson. Cathode Rays. *Philosophical Magazine*, **44**:293, 1897.

[3] E. Rutherford. The Scattering of α and β Particles by Matter and the Structure of the Atom. *Philosophical Magazine*, **21**:669–688, 1911.

[4] J. Chadwick. The Existence of a Neutron. *Proceedings of the Royal Society of London Series A*, 136:692–708, June 1932. doi: 10.1098/rspa.1932.0112.

[5] Carl D. Anderson. The Positive Electron. *Phys. Rev.*, **43**:491, 1933. URL `doi:10.1103/PhysRev.43.491`.

[6] S.H. Neddermeyer and C.D. Anderson. Note on the Nature of Cosmic-Ray Particles. *Phys. Rev.*, 51:884886, 1937. doi: 10.1103/PhysRev.51.884.

[7] Cowan, C.L. and Reines, F. and Harrison, F.B. and Kruse, H.W. and McGuire, A.D. Detection of the Free Neutrino: A Confirmation. *Science*, 124:103–104, 1956. doi: 10.1126/science.124.3212.103.

[8] E. D. Bloom *et. al.* High-Energy Inelastic $e-p$ Scattering at 6° and 10°. *Phys. Rev. Lett.*, **23**:930–934, 1969. URL `doi:10.1103/PhysRevLett.23.930`.

[9] M. Breidenbach *et. al.* Observed Behaviour of Highly Inelastic Electron-Proton Scattering. *Phys. Rev. Lett.*, **23**:935–939, 1969. URL `doi:10.1103/PhysRevLett.23.935`.

[10] Augustin, J.E. et al. Discovery of a Narrow Resonance in e^+e^- Annihilation. *Physical Review Letters*, 33:1406–1408, 1974. doi: 10.1103/PhysRevLett.33.1406.

[11] Aubert, J.J. et al. Experimental Observation of a Heavy Particle J. *Physical Review Letters*, 33:1404–1406, 1974. doi: 10.1103/PhysRevLett.33.1404.

[12] Perl, M.L. et al. Evidence for anomalous lepton production in e^+e^- annihilation. *Physical Review Letters*, 35:1489–1492, 1975. doi: 10.1103/PhysRevLett.35.1489.

[13] Herb, S.W. et al. Observation of a Dimuon Resonance at 9.5 GeV in 400-GeV Proton-Nucleus Collisions. *Physical Review Letters*, 39:252–255, 1977. doi: 10.1103/PhysRevLett.39.252.

[14] TASSO collaboration. Evidence for Planar Events in e^+e^- Annihilation at High Energies. *Phys. Lett. B*, **86**:243–249, 1979. URL `doi:10.1016/0370-2693(79)90830-X`.

[15] UA1 Collaboration. Experimental Observation of Isolated Large Transverse Energy Electrons with Associated Missing Energy at $\sqrt{s}$ = 540 GeV. *Phys. Lett. B*, **122**:103–116, 1983.

[16] UA1 Collaboration. Experimental Observation of Lepton Pairs of Invariant Mass Around 95 GeV/c^2 at the CERN SPS Collider. *Phys. Lett. B*, **126**:398–410, 1983.

[17] UA2 Collaboration. Observation of Single Isolated Electrons of High Transverse Momentum in Events with Missing Transverse Energy at the CERN $p\bar{p}$ Collider. *Phys. Lett. B*, **122**:476–485, 1983.

[18] UA2 Collaboration. Evidence for $Z^0 \to e^+e^-$ at the CERN $p\bar{p}$ Collider. *Phys. Lett. B*, **129**:130–140, 1983.

[19] Abe, F. et al. Observation of Top Quark Production in $p\bar{p}$ Collisions with the Collider Detector at Fermilab. *Physical Review Letters*, 74:2626–2631, 1995. doi: 10.1103/PhysRevLett.74.2626. URL `arXiv:hep-ex/9503002`.

[20] Abachi, S. et al. Search for High Mass Top Quark Production in $p\bar{p}$ Collisions at s = 1.8 TeV. *Physical Review Letters*, 74:2422–2426, 1995. doi: 10.1103/PhysRevLett.74.2422. URL `arXiv:hep-ex/9411001`.

[21] ATLAS Collaboration. Observation of a New Particle in the Search for the Standard Model Higgs Boson with the ATLAS Detector at the LHC. *Phys. Lett. B*, **716**:1–29, 2012. URL `[arXiv:1207.7214[hep-ex]]`.

[22] CMS Collaboration. Observation of a New Boson at a Mass of 125 GeV with the CMS Experiment at the LHC. *Phys. Lett. B*, **716**:30–61, 2012. URL `[arXiv:1207.7235[hep-ex]]`.

[23] Glashow, S.L. Partial-symmetries of weak interactions. *Nucl. Phys.*, 22:579–588, 1961. doi: 10.1016/0029-5582(61)90469-2.

[24] Weinberg, S. A Model of Leptons. *Physical Review Letters*, 19:1264–1266, 1967. doi: 10.1103/PhysRevLett.19.1264.

[25] Higgs, P.W. Broken Symmetries and the Masses of Gauge Bosons. *Physical Review Letters*, 13:508–509, 1964. doi: 10.1103/PhysRevLett.13.508.

[26] T. D. Lee. A theory of spontaneous t violation. *Phys. Rev. D*, 8:1226–1239, Aug 1973. doi: 10.1103/PhysRevD.8.1226. URL https://link.aps.org/doi/10.1103/PhysRevD.8.1226.

[27] G. Veneziano. Construction of a crossing-simmetric, regge-behaved amplitude for linearly rising trajectories. *Il Nuovo Cimento A (1965-1970)*, 57(1):190–197, Sep 1968. ISSN 1826-9869. doi: 10.1007/BF02824451. URL https://doi.org/10.1007/BF02824451.

[28] J. Scherk and J. H. Schwarz. Dual models for non-hadrons. *Nuclear Physics B*, 81:118–144, October 1974. doi: 10.1016/0550-3213(74)90010-8.

[29] Sidney Coleman and Jeffrey Mandula. All possible symmetries of the s matrix. *Phys. Rev.*, 159:1251–1256, Jul 1967. doi: 10.1103/PhysRev.159.1251. URL https://link.aps.org/doi/10.1103/PhysRev.159.1251.

[30] Rudolf Haag, Jan T. Lopuszanski, and Martin Sohnius. All Possible Generators of Supersymmetries of the s Matrix. *Nucl. Phys.*, B88:257, 1975. doi: 10.1016/0550-3213(75)90279-5. [,257(1974)].

[31] Howard E. Haber. Introductory low-energy supersymmetry. In *Proceedings, Theoretical Advanced Study Institute (TASI 92): From Black Holes and Strings to Particles: Boulder, USA, June 1-26, 1992*, pages 589–686, 1993.

[32] A. et al. Antognini. Proton Structure from the Measurement of 2S-2P Transition Frequencies of Muonic Hydrogen. *Science*, 339:417–420, 2013. doi: 10.1126/science.1230016. URL http://science.sciencemag.org/content/339/6118/417.

[33] W. Crookes. Certain Properties of the Emanations of Radium. *Chemical News*, 87:241, 1903.

[34] H. Spieler. *Semiconductor Detector Systems*. Oxford Univ. Press, 2005. doi: 10.1093/acprof:oso/9780198527848.001.0001. URL https://cds.cern.ch/record/1010490.

[35] ATLAS Collaboration. Technical Design Report for the ATLAS Inner Tracker Strip Detector. Technical Report CERN-LHCC-2017-005. ATLAS-TDR-025, CERN, Geneva, Apr 2017. URL https://cds.cern.ch/record/2257755.

[36] About CERN. Jan 2012. URL http://cds.cern.ch/record/1997225.

[37] CERN media and press relations. Facts and Figures 2016, 2016. URL https://press.cern/facts-and-figures/facts-and-figures-2016. Accessed: 19 February 2017.

[38] ATLAS collaboration. ATLAS photos. URL http://atlasexperiment.org/photos/detector-site-surface.html. Accessed: 18 February 2017.

[39] G. et al Baur. Production of anti–hydrogen. *Phys. Lett.*, B368:251–258, 1996. doi: 10.1016/0370-2693(96)00005-6.

[40] The birth of the web. Dec 2013. URL `http://cds.cern.ch/record/1998446`.

[41] Lyndon Evans and Philip Bryant. LHC Machine. *Journal of Instrumentation*, **3**(08): S08001, 2008. URL `http://stacks.iop.org/1748-0221/3/i=08/a=S08001`.

[42] LHC Guide, Mar 2017. URL `https://cds.cern.ch/record/2255762`.

[43] Esma Mobs. The CERN accelerator complex - August 2018. Complexe des accélérateurs du CERN - Août 2018. Aug 2018. URL `https://cds.cern.ch/record/2636343`. Accessed: 9 January 2019.

[44] Ramon Cid Manzano and Xabier Cid Vidal. Taking a closer look at LHC. URL `https://www.lhc-closer.es/taking_a_closer_look_at_lhc/0.lhc_layout`. Accessed: 18 February 2017.

[45] Mark Thomson. *Modern Particle Physics*. Cambridge University Press, New York, 4 edition, 2013. ISBN 9781107034266.

[46] ALICE Collaboration. The ALICE Experiment at the CERN Large Hadron Collider. *Journal of Instrumentation*, **3**(08):S08002, 2008. URL `http://stacks.iop.org/1748-0221/3/i=08/a=S08002`.

[47] ATLAS Collaboration. The ATLAS Experiment at the CERN Large Hadron Collider. *Journal of Instrumentation*, **3**(08):S08003, 2008. URL `http://stacks.iop.org/1748-0221/3/i=08/a=S08003`.

[48] CMS Collaboration. The CMS Experiment at the CERN Large Hadron Collider. *Journal of Instrumentation*, **3**(08):S08004, 2008. URL `http://stacks.iop.org/1748-0221/3/i=08/a=S08004`.

[49] LHCb Collaboration. The LHCb Detector at the CERN Large Hadron Collider. *Journal of Instrumentation*, **3**(08):S08005, 2008. URL `http://stacks.iop.org/1748-0221/3/i=08/a=S08005`.

[50] Claus Grupen and Boris Schwartz. *Particle Detectors*. Cambridge Universty Press, New York, USA, 2 edition, 2008. ISBN 978-0-511-38866-8.

[51] M. et al. Tanabashi. Review of particle physics. *Phys. Rev. D*, 98:030001, Aug 2018. doi: 10.1103/PhysRevD.98.030001. URL `https://link.aps.org/doi/10.1103/PhysRevD.98.030001`.

[52] M *et. al.* Capeans. ATLAS Insertable B-Layer Technical Design Report. Technical Report CERN-LHCC-2010-013. ATLAS-TDR-19, Sep 2010. URL `https://cds.cern.ch/record/1291633`.

[53] Atlas Collaboration. Improved luminosity determination in pp collisions at $\sqrt{s} = 7$ TeV using the ATLAS detector at the LHC. *Eur. Phys J.*, C73(8):2518, 2013. URL `arXiv:1302.4393v2[hep-ex]`.

[54] S van der Meer. Calibration of the Effective Beam Height in the ISR. Technical Report CERN-ISR-PO-68-31. ISR-PO-68-31, CERN, Geneva, 1968. URL `https://cds.cern.ch/record/296752`.

[55] ATLAS collaboration. LuminosityPublicResultsRun2, 2018. URL `https://twiki.cern.ch/twiki/bin/view/AtlasPublic/LuminosityPublicResultsRun2`. Accessed: 16 August 2018.

[56] L. Arnauden et al. Linac4 Technical Design Report. Technical Report CERN-AB-2006-084. CARE-Note-2006-022-HIPPI, CERN, Geneva, Dec 2006. URL `http://cds.cern.ch/record/1004186`. revised version submitted on 2006-12-14 09:00:40.

[57] Hi-Lumi Group. The HL-LHC project, 2018. URL `http://hilumilhc.web.cern.ch/about/hl-lhc-project`. Accessed: 16 August 2018.

[58] Letter of Intent for the Phase-I Upgrade of the ATLAS Experiment. Technical Report CERN-LHCC-2011-012. LHCC-I-020, CERN, Geneva, Nov 2011. URL `https://cds.cern.ch/record/1402470`.

[59] H. W. Kraner. Radiation Damage in Semi-conductor Detectors. *IEEE Transactions on Nuclear Science*, NS-29, No. 3, June 1982. URL `https://ieeexplore.ieee.org/stamp/stamp.jsp?arnumber=4336328`.

[60] ATLAS Collaboration. Letter of Intent for the Phase-II Upgrade of the ATLAS Experiment. Technical Report CERN-LHCC-2012-022. LHCC-I-023, CERN, Geneva, Dec 2012. URL `https://cds.cern.ch/record/1502664`.

[61] ATLAS Collaboration. Technical Design Report for the ATLAS Inner Tracker Pixel Detector. Technical Report CERN-LHCC-2017-021. ATLAS-TDR-030, CERN, Geneva, Sep 2017. URL `http://cds.cern.ch/record/2285585`.

[62] ATLAS Phase-II Upgrade Scoping Document. Technical Report CERN-LHCC-2015-020. LHCC-G-166, CERN, Geneva, Sep 2015. URL `https://cds.cern.ch/record/2055248`.

[63] ATLAS Upgrade Strip Sensor Collaboration. Supply of Silicon Microstrip Sensors of ATLAS12EC specifications. Technical report, 2016. URL `https://edms.cern.ch/document/1547701/2.2`.

[64] ATLAS Collaboration. ABC130 ASIC Specification. Technical Report v4.3, Feb 2013. URL `https://indico.cern.ch/event/227566/attachments/374699/521269/ABC130_DRAFT_Specification04_3.pdf`.

[65] M. Benoit and J. Idarraga. The AllPix Simulation Framework, 2014. URL `https://twiki.cern.ch/twiki/bin/view/Main/AllPix`.

[66] Geant4 Collaboration. GEANT4: A Simulation toolkit. *Nucl. Instrum. Meth.*, A506: 250–303, 2003. doi: 10.1016/S0168-9002(03)01368-8.

[67] Frank Gaede, Ties Behnke, Norman Graf, and Tony Johnson. LCIO: A Persistency framework for linear collider simulation studies. *eConf*, C0303241:TUKT001, 2003. URL `arXiv:physics/0306114[physics.data-an]`.

[68] A. Bulgheroni, T. Klimkovich, P. Roloff, and A.F. Zarnecki. EUTelescope: tracking software. Technical Report EUDET Memo-2007-20, 2007. URL `https://www.eudet.org/e26/e28/e182/e425/eudet-memo-2007-20.pdf`.

[69] Dreyling. Welcome to EUDET-type beam telescopes, 2015. URL `https://telescopes.desy.de/Main_Page`.

[70] DESY ILCSOFT group. GEAR Homepage. URL `http://ilcsoft.desy.de/gear`.

[71] R. Brun and F. Rademakers. ROOT - An Object Oriented Data Analysis Framework. *Nucl. Instrum. Meth.*, A389:81–86, 1997. doi: 10.1016/S0168-9002(03)01368-8. URL `http://www.sciencedirect.com/science/article/pii/S016890029700048X`.

[72] Rodriguez, Daniel and Rossi, Edoardo. EUTelescope Guide for ATLAS ITk Strip: Reconstruction and Analysis. 2017. URL `[arXiv:1707.04535[physics.ins-det]]`.

[73] Claus Kleinwort. General Broken Lines as advanced track fitting method. *Nucl. Instrum. Meth.*, A673:107–110, 2012. doi: 10.1016/j.nima.2012.01.024. URL `[arXiv:1201.4320[physics.ins-det]]`.

[74] V Blobel. A new fast track-fit algorithm based on broken lines. *Nucl. Instrum. Meth.*, A566:14–17, 2006. doi: 10.1016/j.nima.2006.05.156.

[75] Hendrik Jansen et al. Performance of the EUDET-type beam telescopes. *EPJ Tech. Instrum.*, 3(1):7, 2016. doi: 10.1140/epjti/s40485-016-0033-2.

[76] V. Blobel. Software alignment for tracking detectors. *Nucl. Instrum. Meth.*, A566:5–13, 2006. doi: 10.1016/j.nima.2006.05.157.

[77] Hendrik et al. Jansen. Performance of the eudet-type beam telescopes. *EPJ Techniques and Instrumentation*, 3(1):7, 2016. ISSN 2195-7045. doi: 10.1140/epjti/s40485-016-0033-2. URL `https://doi.org/10.1140/epjti/s40485-016-0033-2`.

[78] M. Winter. Development of Swift, High Resolution, Pixel Sensor Systems for a High Precision Vertex Detector suited to the ILC Running Conditions. Technical Report DESY PRC R&D Nr 01/04, 2009. URL http://www.iphc.cnrs.fr/IMG/desy_mimosa_report_prc09.pdf.

[79] M. Garcia-Sciveres et al. The FE-I4 pixel readout integrated circuit. *Nucl. Instrum. Meth.*, A636:S155–S159, 2011. doi: 10.1016/j.nima.2010.04.101.

[80] EUDAQ Software Developers. EUDAQ Website. URL https://github.com/eudaq/eudaq.

[81] F. Guescini. DESY 2017 Testbeam [Presented at the June ATLAS ITk week at CERN, Geneva], 2017. URL https://indico.cern.ch/event/609081/.

[82] Physikalisches Institut Albert-Ludwigs-Universität Freiburg. R0H0 ChipStencil. URL https://twiki.cern.ch/twiki/pub/Atlas/PetalTooling/R0H0_ChipStencil.pdf.

[83] Hill, E and Hessey, N. Checking the dimensions of an r0 sensor. URL https://indico.cern.ch/event/694901/. Presented at the strip sensor meeting, 24 Jan 2018.

[84] Elvedin Tahirovic. AllPixITkStripsDigitiser. URL https://github.com/dinojugosloven/allpix.

[85] X. Llopart, R. Ballabriga, M. Campbell, L. Tlustos, and W. Wong. Timepix, a 65k programmable pixel readout chip for arrival time, energy and/or photon counting measurements. *Nucl. Instrum. Meth.*, A581:485–494, 2007. doi: 10.1016/j.nima.2007.08.079,10.1016/j.nima.2007.11.003. [Erratum: Nucl. Instrum. Meth.A585,106(2008)].

[86] C. Jacoboni, C. Canali, G. Ottaviani, and A. Alberigi Quaranta. A review of some charge transport properties of silicon. *Solid-State Electronics*, 20(2):77 – 89, 1977. ISSN 0038-1101. doi: https://doi.org/10.1016/0038-1101(77)90054-5. URL http://www.sciencedirect.com/science/article/pii/0038110177900545.

[87] G. Wanner E. Harrier, S. P. Norsett. *Solving Ordinary Differential Equations I.* Springer-Verlag, Berlin, 2 edition, 1993. doi: 10.1007/978-3-540-78862-1.

[88] M. Nakhostin. *Signal Processing for Radiation Detectors.* Wiley, 2017. doi: 10.1002/9781119410225.

[89] Xiaocong Ai. EUTelescope. URL https://github.com/XiaocongAi/eutelescope.

[90] ATLAS ITk strips testbeam group. Runlist for DESY 2017 testbeam. URL https://docs.google.com/spreadsheets/d/1FfUMhIEV5yZ3U8LMBFlyAQtBCjpBzp8-u0fY25Gs_2w/edit#gid=546434083.

[91] Francesco Guescini on behalf of the ITk strip testbeam group. Desy 2017 testbeam. ATLAS ITk week, June 2017. URL `https://indico.cern.ch/event/609081/contributions/2630469/attachments/1482957/2300956/20170626.pdf`.